Modeling Fluid Flow in Natural Systems: Model Validation and Demonstration

Fuel Cycle Research & Development

Prepared for
U.S. Department of Energy
Used Fuel Disposition Campaign
S.L. Painter, C.W. Gable,
N. Makedonska, J. Hyman,
S. Karra, S. Chu
Los Alamos National Laboratory
H.H. Liu, J. Birkholzer
Lawrence Berkeley National Laboratory
Y. Wang, W.P. Gardner
Sandia National Laboratories
G.-Y. Kim
Korean Atomic Energy Research Inst.

January 2014
FCRD-UFD-2014-000059
LANL Report LA-UR-14-20574

FCT Quality Assurance Program Document

Appendix E
FCT Document Cover Sheet

Name/Title of Deliverable/Milestone	Modeling Fluid Flow in Natural Systems, Model Validation and Demonstration
Work Package Title and Number	FT-14LA080702 Crystalline Disposal R&D – LANL (Rev 1)
Work Package WBS Number	**1.02.08.07**
Responsible Work Package Manager	Scott L. Painter (Name/Signature)
Date Submitted	January 2014

Quality Rigor Level for Deliverable/Milestone	☐ QRL-3	☐ QRL-2	☐ QRL-1 ☐ Nuclear Data	☒ N/A*

This deliverable was prepared in accordance with Los Alamos National Laboratory
(Participant/National Laboratory Name)

QA program which meets the requirements of
☒ DOE Order 414.1 ☐ NQA-1-2000

This Deliverable was subjected to:

☒ Technical Review

Technical Review (TR)

Review Documentation Provided

☐ Signed TR Report or,
☐ Signed TR Concurrence Sheet or,
☒ Signature of TR Reviewer(s) below

Name and Signature of Reviewers

HARI VISWANATHAN

☐ Peer Review

Peer Review (PR)

Review Documentation Provided

☐ Signed PR Report or,
☐ Signed PR Concurrence Sheet or,
☐ Signature of PR Reviewer(s) below

*Note: In some cases there may be a milestone where an item is being fabricated, maintenance is being performed on a facility, or a document is being issued through a formal document control process where it specifically calls out a formal review of the document. In these cases, documentation (e.g., inspection report, maintenance request, work planning package documentation or the documented review of the issued document through the document control process) of the completion of the activity along with the Document Cover Sheet is sufficient to demonstrate achieving the milestone. QRL for such milestones may be also be marked N/A in the work package provided the work package clearly specifies the requirement to use the Document Cover Sheet and provide supporting documentation.

This page left blank intentionally.

SUMMARY

Clay and granitic media are potential host media for future repositories for used nuclear fuel. This report addresses the representation and characterization of flow in these two media within numerical process models.

In low permeability crystalline rock, flow is primarily in relatively sparse networks of fractures. Discrete fracture network (DFNs) models are an approach to representing flow in fractured rock that explicitly represents the geometry and flow properties of individual fractures. The DFN approach captures important flow phenomena that are difficult to represent in conventional equivalent continuum approaches. However, the DFN approach is computationally demanding and requires care in constructing computational meshes. New DFN generation and computational grid generation methods were described in a previous report. The new approach places constraints on the generation of the DFN. These constraints make it possible to create high-quality computational meshes that enable accurate flow and transport solutions on the generated DFNs. Chapter 2 of the current report describes work to extend, verify, and trial the new capability. The DFN capability was extended to make it possible to use highly parallel software to solve for groundwater flow on the unstructured DFN meshes and to combine DFN meshes with traditional volume meshes representing backfilled tunnels or boreholes. A new approach to the next step in the DFN-based computational workflow, the tracking of particles representing radionuclide mass through the DFN, is also described. The particle tracking capability involves reconstruction of flow on fully unstructured control volume meshes. Control volumes that contain segments of fracture intersections are split into four control volumes, one for each side of the intersection on each fracture plane. The workflow is verified using a simple four-fracture configuration for which the flow and transport behavior can be deduced. Application of the coupled DFN flow and transport capability at the field scale is also demonstrated using DFN parameters similar to the Forsmark Sweden site.

Water flow in clay media is another important process. Experimental results indicate that the traditional form of Darcy's law is not adequate for describing water flow processes in clay media because the observed relationship between water flux and hydraulic gradient can be highly non-linear. To capture this non-Darcian flow behavior, a new relationship between water flux and hydraulic gradient was summarized in a previous report. That new relationship was shown to be consistent with experimental observations for both saturated and unsaturated conditions. Chapter 3 of the current report extends the model to consider temperature effects and anisotropic formations. In addition, flow in the excavation damage zone of a generic repository is shown, as the result of non-Darcy flow, to be extremely small such that solute transport is diffusion dominated rather than advection dominated. It is also shown that measurements of relative permeability in unsaturated conditions may be significantly in error unless the non-Darcian flow behavior is taken into account.

The use of environmental tracers to characterize the transport characteristics of fractured rock on the spatial scales relevant for a repository geosphere is discussed in Chapter 4. Lumped parameter models of stable isotope, tritium and CFC-12 transport are compared to data from the Bedrichov Tunnel Experiment in the Czech Republic. The tracer data suggest rapid transport at the site and little matrix diffusion.

Available data from the KURT generic underground research laboratory in Korea are summarized in Chapter 5. The KURT site characterization data will be valuable for testing strategies for using characterization data to constrain models of fractured crystalline rock sites.

Chapter 7 provides a literature survey on upscaling permeability and equilibrium distribution coefficients to the spatial scales relevant for performance assessment modeling.

CONTENTS

SUMMARY v

ACRONYMS xii

1 INTRODUCTION 1-1

2 REFINEMENT AND DEMONSTRATION OF DISCRETE FRACTURE NETWORK MODELS FOR FLOW AND TRANSPORT IN FRACTURED CRYSTALLINE ROCK 2-1
2.1 Background 2-1
2.2 Technical Methodology 2-2
2.2.1 Meshing Considerations 2-2
2.2.2 Solving for the Groundwater Velocity Field 2-4
2.2.3 Particle Tracking 2-5
2.3 Verification Tests 2-7
2.4 Application to the Forsmark Site 2-8
2.5 Hybrid DFN/Volume Meshes 2-9
2.6 Summary and Status of the Work 2-10
2.7 References 2-25

3 HYDROLOGIC FLOW IN LOW-PERMEABILITY MEDIA 3-1
3.1 Introduction 3-1
3.2 A Review of Relationships between Water Flux and Hydraulic Gradient 3-2
3.3 A Demonstration of Impact of Non-Darcian Flow on Performance of a Clay Repository 3-6
3.4 Influence of Non-Darcian Flow on Observed Relative Permeability 3-9
3.5 A Hypothesis Regarding the Temperature Dependence of the Threshold Hydraulic Gradient 3-11
3.6 An Approximate Formulation of Water Flux in Anisotropic Media 3-12
3.7 Concluding Remarks 3-13
3.8 References 3-14

4 Using Environmental Tracers to Estimate Fracture Network Properties: Bedrichov Tunnel, Czech Republic 4-1
4.1 Introduction 4-1
4.2 Lumped Parameter Models 4-2
4.3 Results 4-3
4.4 Conclusions 4-8
4.5 References 4-8

5 KURT Site Characterization Data - Fracture and Hydrologic Data from Deep Boreholes in KURT Site 5-9
5.1 Introduction 5-9
5.2 KURT (KAERI Underground Research Tunnel) 5-9

5.3 Geology of the KURT Site 5-13
5.4 Deep Boreholes in the KURT Site 5-15
5.5 Concluding Remarks 5-16
5.6 References 5-17

6 Upscaling of Hydrologic and Geochemical Parameters: Literature Review 6-19
6.1 Introduction 6-19
6.2 Upscaling Permeability/Hydraulic Conductivity 6-19
6.2.1 Spatial Averaging 6-19
6.2.2 Renormalization 6-20
6.2.3 Perturbation Theory 6-20
6.2.4 Numerical Inverse 6-21
6.2.5 Power-Law Averaging 6-21
6.2.6 Evaluation 6-22
6.3 Upscaling of Sorption/Distribution Coefficients (K_d) 6-23
6.4 Scale Dependence of the Effective Matrix Diffusion Coefficient 6-25
6.5 Site Characterization to Performance Assessment Upscaling 6-27
6.6 References 6-27

FIGURES

Figure 2-1. Example of stochastically generated discrete fracture network with 100 individual fractures in a domain of size 8 × 8 × 8 m. Each fracture in the network is shown by different color. 2-12

Figure 2-2. Same as Figure 2-1 but with the computational grid visible. Note that the mesh resolution is fine near intersections and coarse away from fracture intersections. 2-12

Figure 2-3. Two intersecting fractures showing conforming Delaunay triangulations (a) and Voronoi control volumes (b). The Delaunay triangulation conforms to the fractures' intersection without distorting the fracture lines intersections. Four types of nodes are distinguished on computational grid (a). Along the line of intersection control volume cells are common to both fractures (b). 2-13

Figure 2-4. Example of steady state pressure solution on a 100-fracture DFN. The boundary conditions are applied to the *x* faces of 3D domain. 2-14

Figure 2-5. Illustration of the different representations of control volumes and velocities on fracture interfaces. The interior interface node shown in a) is on the intersection of two fractures, fracture 1 and fracture 2, and belongs to both fractures. Each single 3-D control volume cell (b) is used for the purposes of obtaining the flow solution. The control volume cell on the intersection is split into two 2D polygons (c), one for each of the intersecting fracture. Those polygons are further divided at the intersection line; in (d) the blue and purple polygons belong to fracture 1, and the yellow and green polygons belong to fracture 2. The flow velocities are reconstructed on each of the split polygons, with the result (e) being that four velocities are associated with each interior node. 2-15

Figure 2-6. a) The flow field of individual fracture extracted from a DFN of 10^3 fractures is shown in *xy* plane. The nodes are colored by their corresponding pressure value: low pressure is indicated by dark blue colors, high pressure is shown by light red colors. The black arrows represent reconstructed flow field velocities. b) Detail showing a fracture intersection with flow incoming from the intersecting fracture and moving in both directions on the represented fracture. c) Detail showing another fracture intersection. At this intersection flow flow is toward the intersection and into the intersecting fractures. Note that two velocities are shown for each interior interface node. There are two corresponding velocities on the intersecting fracture (not shown). 2-16

Figure 2-7. Discrete fracture network of 4 fractures used for a verification test of the new particle-tracking capability. Boundary conditions are applied to *x* faces of the domain; flow goes from the left to right side of the DFN. The domain size is 1.8 × 1.0 × 0.65 m, and each fracture thickness is 0.01 m. The insert shows an electrical circuit that is an analog to the DFN for purposes of calculating the verification target values of flow and travel time. 2-17

Figure 2-8. The steady state flow pressure solutions obtained for the 4 fractures DFN used in the two verification tests. Light red colors correspond to high pressure. a) Pressure solution obtained for DFN where all fractures are designated equal permeability value, $k_1=k_2=k_3=k_4=2.5\cdot10^{-13}$ m^2. b) Pressure solution obtained for the same DFN, where fracture *3* is giving higher permeability, $k_3=2.5\cdot10^{-12}$ m^2, $k_1=k_2=k_4=2.5\cdot10^{-13}$ m^2. 2-18

Figure 2-9. Particle tracks on 3-fracture verification tests. In a) all the fractures are given the same permeability value, and approximately the same number of particles choose to travel through fracture 3 as through fracture 4. In b) fracture 3 (bottom fracture) is given higher permeability. As a result, more particles travel through bottom path of the DFN. 2-19

Figure 2-10. Steady state flow solution (left) and permeability (right) on three DFN realizations based on data from the Forsmark site. 2-20

Figure 2-11. a) 2000 particles trajectories starting from one region in the middle of the in-flow boundary side trajectories diver fast and fill up the domain. b) Particles final positions at in-flow (red) and out-flow (blue) boundaries. 2-21

Figure 2-12. Travel time distribution for 5×10^5 particles that enter the DFN from a region in the middle of in-flow boundary side. 2-22

Figure 2-13. Cumulative distribution of particle travel time: a) uniformly weighted at starting positions; b) flux-weighted at starting positions. 2-23

Figure 2-14. Example showing the creation of a hybrid tetrahedral/DFN mesh. Such hybrid meshes are needed in applications. 2-24

Figure 3-1. Definition of threshold hydraulic gradient 3-3

Figure 3-2. Correlation between permeability and threshold hydraulic gradient (Liu and Birkholzer, 2013). 3-5

Figure 3-3. Flow pattern for a two-dimensional generic clay repository; red = EDZ. (Bianchi et al., 2013). 3-6

Figure 3-4. The normalized pore velocity as a function of threshold gradient *I*. The normalized velocity refers to the ratio of the maximum pore velocity within the EDZ to that in the Darcian-flow case. 3-8

Figure 3-5. "Measured" relative permeability curves under different hydraulic gradient, as a function of the effective saturation. Note that $I = 0$ corresponds to the "true" relative permeability curve calculated with Eq. (3-10). 3-10

Figure 3-6. The temperature dependence of the relationship between threshold hydraulic gradient and permeability. 3-12

Figure 4-1. Measured and modeled stable isotope composition for the Bedrichov sample V6 using the exponential age distribution 4-4

Figure 4-2. Measured and modeled stable isotope composition for the Bedrichov sample V6 using the dispersive age distribution 4-4

Figure 4-3. Tracer plot of ^{3}H vs CFC-12 for precipitation (blue line) at Bedrichov, measured samples (green triangles) and expected concentration for the year 2012 given an exponential age distribution as a function of increasing mean age. Black circles are the expected concentration for every 5 year interval of mean age 4-5

Figure 4-4. Tracer plot of ^{3}H vs CFC-12 for precipitation (blue line) at Bedrichov, measured samples (green triangles) and expected concentration for the year 2012 given a dispersion age distribution as a function of increasing mean age. Black circles are the expected concentration for every 5 year interval of mean age 4-6

Figure 4-5. Expected age distributions for a dispersion model only and a dispersion model which includes retention time from infinite matrix diffusion for a mean advective travel time of 2 years, a matrix porosity of 1% and a fracture diameter of 0.2mm 4-7

Figure 4-6. Expected age distributions for a dispersion model only and a dispersion model which includes retention time from infinite matrix diffusion for a mean advective travel time of 100 years, a matrix porosity of 10% and a fracture diameter of 0.2mm 4-7

Figure 5-1. Current layout of the KURT 5-11

Figure 5-2. Location of in situ tests and experiments with related boreholes at KURT 5-12

Figure 5-3. An alternative layout for tunnel extension of KURT 5-13

Figure 5-4. Location and geologic map of KURT site. 5-14

Figure 5-5. Location of boreholes around KURT. 5-16

TABLES

Table 2-1. Numerical and analytical results of particle travel time in verification tests. 2-11
Table 2-2. DFN parameters used in simulations of the Forsmark site. 2-11
Table 3-1. Parameter Value for the Generic Clay Repository (Bianchi et al., 2013). 3-7
Table 5-1. Data list for the task of sharing KURT site characterization data 5-10

ACRONYMS

1D	one dimensional
2D	two dimensional
3D	three dimensional
CFCs	chlorofluorocarbon
BSC	Bechtel SAIC Co.
DB	Deep borehole
DFN	Discrete fracture network
DO	dissolved oxygen
EDZ	excavation disturbed zone
EOR	enhanced oil recovery
KAERI	Korea Atomic Energy Research Institute
KURT	KAERI Underground Research Tunnel
LANL	Los Alamos National Laboratory
LBNL	Lawrence Berkeley National Laboratory
MD	Molecular dynamics
MOST	Ministry of Science and Technology
PDFs	Probability distribution functions
PSLG	Planar straight line graph
R&D	Research and Development
SEM	Scanning electron microscope
SNL	Sandia National Laboratories
SP	Streaming potential
UFDC	Used Fuel Disposition Campaign

This page left blank intentionally.

FLUID FLOW MODEL DEVELOPMENT FOR REPRESENTATIVE GEOLOGIC MEDIA

1 INTRODUCTION

The U.S. Department of Energy Office of Nuclear Energy, Office of Fuel Cycle Technology has established the Used Fuel Disposition Campaign (UFDC) to conduct research and development (R&D) activities related to storage, transportation and disposal of used nuclear fuel and high-level nuclear waste.

The UFDC is currently evaluating generic research issues affecting the viability of repositories in three geologic media (salt, clay, and crystalline rock). Consistent with the well-accepted multiple barrier concept for waste repository safety, repository systems include both natural and engineered barriers. From this perspective, the natural barrier needs to be evaluated and necessary research conducted to ensure adequate safety function. Consistent with the broader objectives of the UFDC, R&D is being conducted to develop (1) fundamental understanding of natural system performance in a range of environments, and (2) computational modeling capability for evaluating natural system performance.

The R&D Roadmap for UFDC Natural System Evaluation and Tool Development (Wang, 2011) identified fluid flow in fractured crystalline rock and in low-permeability clay material as priority R&D topics for the UFDC Natural System Evaluation and Tool Development work package. This report summarizes flow model development for those two representative geologic media. Chapter 2 provides a summary of UFDC work to develop advanced flow modeling approaches for fractured crystalline rock based on explicitly represented fractures (Contributors: S. Painter, C. Gable, N. Makedonska, J. Hyman, S. Karra and S. Chu from Los Alamos National Laboratory). Section 3 summarizes modeling approaches for non-Darcian flow in clays (Contributors: H.-H. Liu and J. Birkholzer from Lawrence Berkeley National Laboratory). The use of environmental tracers to characterize the transport characteristics of fractured rock on the spatial scales relevant for a repository geosphere is discussed in Chapter 4 (Payton Gardner, Sandia National Laboratory). Available data from the KURT generic underground research laboratory in Korea are summarized in Chapter 5 (Geon-Young Kim, Korean Atomic Energy Research Institute). The KURT site characterization data will be valuable for testing strategies for using characterization data to constrain models of fractured crystalline rock sites. Chapter 6 (Yifeng Wang, Sandia National Laboratory) provides a literature survey on upscaling permeability and equilibrium distribution coefficients to the spatial scales relevant for performance assessment modeling.

2 REFINEMENT AND DEMONSTRATION OF DISCRETE FRACTURE NETWORK MODELS FOR FLOW AND TRANSPORT IN FRACTURED CRYSTALLINE ROCK

2.1 Background

Relatively impermeable hard rocks such as fractured granite and fractured welded tuffs have been considered previously as potential repository host media. Fractures are ubiquitous in such media and provide the primary migration pathways for radionuclides. Experience has shown that flow and transport in fractured rock are rarely described adequately by uniform or mildy nonuniform isotropic continuum representations (Neuman 2005) and a range of alternatives to the classical continuum representation have been developed. These alternative approaches may be grouped into three general classes: discrete fracture network representations, complex continua representations, and hybrid representations.

Discrete fracture network (DFN) models depict the rock mass as an interconnected network of explicitly represented fractures. The approach is in the reductionist tradition, implicitly assuming that detailed statistical descriptions of small observable features will, once combined in numerical simulations, lead to understanding of the system as a whole. Networks of fractures are first stochastically generated using a stochastic model derived from site data. A computational mesh is placed on each fracture plane usually ensuring that the mesh on each of a pair of intersecting fractures matches along the intersection. Groundwater flow equations are then solved using this computational mesh. The final step is then to simulate radionuclide transport using the computed flow field, usually by particle tracking. Most large-scale applications do not explicitly mesh the matrix volumes between adjacent fractures. Instead the effects of diffusion into the unrepresented matrix volume are represented (modeled) in the transport step (see e.g. Painter et al. 2008). DFN simulations were introduced first in theoretical studies; feasibility of detailed site-specific applications has also been clearly demonstrated (e.g. Cvetkovic et al. 2004, Svensk Kärnbränslehantering 2011).

Complex continua representations generalize a simple effective continuum representation to account for various flow and transport phenomena. Dual continuum models (Barenblatt et al. 1960; Warren and Root 1963) represent fractured porous rock as two overlapping and interacting continua. In its most general form (e.g. Duguid and Lee, 1977), known as the dual permeability model, flow and transport takes place in both the fracture and matrix continua while accounting for fluid and solute migration between the two continua in response to pressure and concentration differences. Commonly, flow in the matrix system is neglected relative to flow in the fracture system. In this case, the matrix acts as a non-conductive reservoir for fluid and/or solute storage and the fracture system provides the fluid migration pathways. In this variant, usually referred to as the dual porosity model, fluid and solute flux are proportional to the pressure and concentration differences between the two continua at a given location and time. The dual continuum class of models has also been generalized (Pruess and Narasimhan 1985; Zyvoloski et al. 2008) to better represent gradients internal to the matrix blocks. In this approach, multiple continua are used to represent matrix processes. Flow between spatially adjacent matrix cells may be included or not represented, depending on the variant.

Regardless of how the matrix/fracture interactions are represented, multiple continuum models originally conceptualized the fracture flow system as having a representative elementary volume (REV) that establishes a spatial scale above which the flow properties become approximately independent of scale. For natural fracture patterns, which often have a broad distribution of fracture lengths, the existence of a classical REV scale may be questionable. Neuman proposed a stochastic continuum approach that does not require an REV (Neuman 1987, 2005). In his approach, an effective permeability tensor and other required flow/transport properties are assigned to each grid block in a conventional continuum

conceptualization. However, the properties vary from grid cell to grid cell according to a stochastic model. Moreover, the stochastic model is dependent on the size of the grid block. Thus, a different stochastic model is required if the spatial discretization is changed. Parameterization of a stochastic continuum model, which generally requires inverse modeling of multiple pressure interference and solute tracer tests, has been demonstrated at the Apache Leap field site (e.g. Neuman 2005). The stochastic continuum model may be combined with any of the dual or multiple continua ideas to represent fracture/matrix interactions.

Hybrid methods adopt a reductionist view similar to DFN models but also use continuum representations for practical computational reasons (e.g. to reduce the overall size of the computational mesh). Hybrid methods fall into two subclasses: nested and upscaled. In nested models, explicit DFN models are used along transport pathways or in other regions where high spatial resolution is required and continuum representations are used in regions that are of less interest. This approach allows for a DFN representation of transport in and near expected transport pathways while still modeling a sufficiently large region to honor natural hydraulic boundary conditions. In upscaled models, explicit DFN representations are constructed and stochastically generated. However, the flow problem is not solved on the full DFN. Instead, the DFN is used to establish, grid block by grid block, equivalent permeability tensors for use in a continuum model. Jackson et al. (2000), Svensson (2001) and Botros et al. (2008) provide examples of upscaling algorithms for the permeability tensors. Experience with upscaled models for flow has generally been good, but the approach is questionable for transport. Extensions that attempt to recover the transport effects of subgrid velocity variability through stochastic simulation have emerged (Painter and Cvetkovic 2005) but have not been fully explored.

Experience suggests that it should be possible to model a sufficiently well-characterized site in a variety of ways and that combinations of methods may allow for the most efficient use of available information. Extensive studies by the Swedish Nuclear Fuel and Waste Management Company in support a safety case for a proposed spent fuel repository (Svensk Kärnbränslehantering 2011) has clearly demonstrated practical utility of hybrid approaches to flow and transport modeling. Given this experience it is likely that DFN and DFN/continuum hybrids will play an important role in future assessments of fractured hard rock sites. However, modern and non-proprietary modeling tools for supporting such assessments and for addressing key unresolved scientific issues are lacking.

This Chapter addresses Topic P1 of the R&D Plan for UFDC Natural Systems Evaluation and Tool Development – Development of Discrete Fracture Models. The longer-term objective is to develop discrete fracture network (DFN) flow and transport modeling capability, which was identified as a capability gap. The DFN software development process related to requirements definition, algorithm design and prototyping were summarized in FY2012 report. This chapter summarizes the current state of the DFN flow and transport modeling capability with a focus on new particle tracking capability, verification and application.

2.2 Technical Methodology

Three algorithmic steps related to DFN flow and transport simulations are identified: meshing, solving for the groundwater velocity field, and radionuclide transport simulation.

2.2.1 Meshing Considerations

The DFN approach represents fractures as two-dimensional finite objects in a three-dimensional domain. Each fracture is characterized by its shape, orientation, and location in three-dimensional space. In our model, fracture shapes are represented by ellipses or rectangles; the lengths of fractures follow a truncated power-low distribution. Fracture locations in the three-dimensional domain are taken to be stochastic due

to the difficulty of directly measuring location of fractures in the subsurface. Fig. 2-1 shows an example of a stochastically generated network of 100 fractures, where number of rectangular fracture shape is equal to elliptical ones. A wide variety of lengths, locations, and orientations in space coupled with the complexity of the intersections between fractures create difficulties in generating a high-quality computational mesh. The quality of mesh is often quantified by the distribution of cell aspect ratios or angles, as it is often difficult to obtain accurate numerical solutions on long thin cells.

Mesh generation for DFN flow and transport simulations involves constructing a quality mesh on each fracture surface that also meets two constraints: (1) the mesh on each fracture must conform to intersections with other fractures, and (2) the meshes for each of two intersecting fractures must coincide along the intersection. The second constraint may be relaxed if mortar methods (e.g. Ewing et al. 2000, Arbogast et al. 2000, Pichot et al. 2010) are used to solve for flow and transport. Mortar methods are not addressed here.

Regardless of whether the mesh is generated for use in a control volume or finite element calculations, the major meshing issues are associated with pathological cases that lead to small or high aspect ratio cells/elements. To overcome this meshing difficulty, Hyman et al. (2014) present a new approach to generate Delaunay triangulation on a stochastically generated DFN. Stochastic generation of the fracture network is often necessary because the locations of individual fractures in the subsurface are generally not known, but their statistical distribution can be inferred from detailed characterization studies. However, stochastic network generation usually produces pathological mesh conditions around fracture intersections unless some constraints are placed on the mesh generation. In the approach of Hyman et al. (2014) a minimal feature size that will be resolved is defined. Any stochastically generated fracture that would have created a feature of the DFN less than this length scale is rejected at the generation step. Fig. 2-2 shows the complexity of fully meshed 100-fracture network (previously shown in Fig. 2-1). The mesh is fine near fracture intersection and coarse away from facture intersections, thus minimizing mesh size in order to keep computational cost down. At the same time, the mesh cells meet quality criteria on the cell shape, thus ensuring stability and accuracy of the physics solution being computed. Additionally, the mesh generated on two intersecting fractures coincides along the intersection line.

The approach developed by Hyman et al. (2014) is unique in that it produces a high-quality conforming DFN mesh for use in control volume codes. The finite volume method is often preferred over finite-element methods for complex multiphysics applications because of the finite volume method's local mass conservation properties and the ease of dealing with phase disappearance and reappearance. The new DFN generation and meshing capability makes it possible to use existing subsurface flow and transport codes based on the finite volume method.

Fig. 2-3a shows a zoomed frame on an intersection of two fractures. For the purposes of particle tracking (addressed later) it is convenient to classify nodes of the triangulation as follows:

- Interior nodes are located inside a fracture and do not lie on a boundary or a fracture intersection.
- Exterior nodes are on the fracture boundary but do not lie on a fracture intersection.
- Interior interface nodes are located on the intersection of two fractures and are not on a boundary.
- Exterior interface nodes lie on fracture intersections and are also on a boundary of one (or both) of the intersecting fractures.

In the last two cases, interface nodes are formally considered to be common ones of both intersecting fractures and belong to both fractures simultaneously.

Since the goal of the meshing is to obtain flow solution followed by solute transport modeling, the control volume cells are derived from a Delaunay triangulation (Fig. 2-3b). Therefore, the triangulation of each fracture obeys Delaunay triangulation; a Voronoi tessellation is formed based on it. As a result, each

fracture is divided into control volume cells formed by perpendicular bisectors between adjacent nodes in an underlying triangulation of the cell centers (Fig. 2-3).

2.2.2 Solving for the Groundwater Velocity Field

Numerical methods for solving for flow within the DFN must be able to accommodate the fully unstructured grid, which is locally two-dimensional within each fracture. Three methods are identified: conventional finite elements, mixed hybrid finite elements, and control volumes.

Early 3-D DFN research codes and most existing commercial codes use the finite element method to solve for flow within the fracture network. The finite element method is able to accommodate fully unstructured grids without difficulty, but is not locally mass conserving. Lack of local mass conservation is an issue for radionuclide transport simulations because it can lead to nonphysical mass accumulation. If a particle tracking method is used for the radionuclide transport simulation, for example, lack of local mass conservation can cause particles representing packets of radionuclide mass to become stuck in the computational mesh. If enough particles become stuck, a misleading representation of geosphere performance would result. Local postprocessing of the finite-element flow solution using the approach of Cordes and Kinzelbach (1992) or similar method can improve the local mass conservation dramatically. This method is difficult to implement especially at fracture intersections.

Applied to groundwater flow, the mixed hybrid finite element method (Mose et al. 1994) approximates simultaneously the hydraulic head and groundwater velocity. The number of unknowns is doubled, but the approximation to the groundwater velocity is obtained as a continuous field, thus avoiding velocity discontinuities that plague transport calculations.

The finite element method and the mixed hybrid finite element method are convenient for saturated flow but are not ideal for unsaturated or multiphase flow. Control volume methods are traditionally used for these situations. Applied to flow, the control volume method solves conservation equations for water mass on each computational cell. Applied to radionuclide transport, the control volume method solves conservation equations for radionuclide mass on each computational cell, thus avoiding any issues with local mass conservation. The computer codes FEHM (Zyvoloski 2007) and TOUGH2 (Pruess et al. 1999) are based on the control volume method.

The control volume method is used here to obtain the groundwater flow solution. Applied to flow, the control volume method solves conservation equations for water mass on each computational cell. Applied to transport simulation, the control volume method solves mass conservation equation on each computational cell, which is a necessary requirement to avoid local mass stagnation.

Our DFN modeling capability has been adapted to work with the massively parallel PFLOTRAN computational tool (Lichtner et al. 2013). The control volume cells are used explicitly in PFLOTRAN. This link makes it possible to do large-scale flow simulations on DFN grids using high-performance computing. It also brings the complex multiphase flow and equations of state in PFLOTRAN to DFN simulations.

An example flow solution using a 100-fracture DFN (previously shown in Figs. 2-1 and 2-2) is presented in Fig. 2-4. In this example, constant-pressure boundary conditions are applied to the x-faces of the domain. Specifically, all the nodes of the DFN located on the left face of the domain are given the lowest pressure value, *1.0* MPa, while all the nodes on right face of the domain are given the highest pressure, *2.0* MPa. No-flow conditions are imposed on the remained boundary faces of the DFN. In this case the flow direction is going from the right to the left side of the domain, along the x axis. Gravity is neglected here.

The radionuclide particle simulation requires the flow velocity to be defined at all points of the simulation domain. Using the flow solutions obtained on unstructured control volume grids is not straightforward

because the control volume flow solution does not produce a continuous flow velocity field. Instead, it provides a set of scalar quantities that are approximations to the normal component of Darcy flux integrated over each edge of each control volume cell. For particle tracking the reconstruction of a continuous velocity field from the scalar quantities obtained by PFLOTRAN is required.

A new approach for particle-tracking modeling using flow solutions obtained on unstructured control volume meshes was developed by Painter et al. (2011). The method uses an unconstrained least square method on an interior cell. The constrained least square method is applied to reconstruct velocities on boundary cells for exterior nodes. The Darcy velocities so obtained on nodes then can be continuously interpolated to any point in the domain of interest. Their 2D tests correctly reproduced uniform corner-to-corner flow on fully unstructured grid. Their approach is for the first time tested here on transport simulations in DFNs.

The main difficulties in DFN transport modeling come into play on fracture intersections. The control volume cells are two-dimensional polygons with centers on interior and exterior nodes, while for interface nodes the control volume cells are three-dimensional objects. Moreover, at the fracture intersections the flow behavior is nontrivial. For example, the main flow can go through intersection and continue in the same fracture in the same direction, or change its direction and proceed in intersecting fracture. Therefore, the flow velocities associated with interface nodes must indicate flow directions not only into each intersecting fractures, but also describe flow field on every fracture portion around the intersection line.

In order to overcome this problem, a new technique, schematically presented in Fig. 2-5, was developed. First, the control volume cell on the intersection (Fig. 2-5b) is split into two 2D polygons, each of them corresponding to one of two intersecting fractures (Fig. 2-5c). Second, each obtained control volume polygon is divided again into two parts along the intersection line (Fig. 2-5d). Flow velocity vectors are then reconstructed on the split polygons using the method of Painter et al. (2011). Fig. 2-5e shows the reconstructed flow velocities on the interface nodes and interior nodes of connected triangular elements. The velocity vectors on the interface nodes have four flow directions, one for each side of each fracture. The blue and purple parts of fracture 1 show outgoing flow from the intersection, yellow and green parts of fracture 2 indicate flow into the fracture intersection.

In our approach, the DFN is three-dimensional with fractures as planar objects. During the velocity reconstruction and particle tracking simulation every single fracture is viewed as a two-dimensional polygon. Fig. 2-6a shows the flow field of an individual fracture extracted from a DFN of 1000 fractures. The nodes are colored by their respective pressure magnitude, where low pressure corresponds to dark blue colors. The black arrows represent the reconstructed flow velocities. There are 10 fracture intersection lines on this elliptical fracture. Flow comes into the fracture on some intersections and leaves on others. Intersections with outgoing and incoming flow are shown in Fig. 2-6b and Fig. 2-6c, respectively. As a result of dividing of control volume cells into two polygons along the intersection line, the interface nodes have two flow velocity vectors on each fracture, indicating flow direction on each side of the intersection.

2.2.3 Particle Tracking

Although the finite element, mixed hybrid finite element, or control volume method can be used to solve the advection dispersion equation to represent radionuclide transport, particle tracking on the computed groundwater velocity field is the more common approach to representing radionuclide transport in DFN modeling. Particle tracking does not produce numerical dispersion and can accommodate complex dispersivity tensors. In addition, computational strategies that include the effects of matrix diffusion and sorption by postprocessing the results of particle tracking simulations without matrix diffusion are among the most efficient and practical methods available for representing the transport effects of matrix diffusion.

Once the discrete representation of flow velocity field is defined and every node on the DFN computational mesh is assigned flow velocity vectors, the groundwater velocity can be determined at any point of a DFN. (Notice, the presented particle-tracking model assumes no interaction of particles with matrix domain, particles can travel only on fractures, where the flow is present.)

The standard barycentric interpolation approach is applied to define the particle velocity. In planar two dimensional space, if $\boldsymbol{r}_1$, $\boldsymbol{r}_2$, and $\boldsymbol{r}_3$ are the positions of nodes of the triangular element where the particle is located at the current computational time step and $\boldsymbol{v}_1$, $\boldsymbol{v}_2$ and $\boldsymbol{v}_3$ are the values of velocity at those nodes, then the particle's velocity $\boldsymbol{v}$ at some position $\boldsymbol{r}$ in the triangular element can be interpolated as

$$\boldsymbol{v}(\boldsymbol{r}) = \sum_{i=1,3} \lambda_i \boldsymbol{v}_i, \tag{2-1}$$

where

$$\begin{pmatrix}\lambda_1\\ \lambda_2\end{pmatrix} = \boldsymbol{T}^{-1}(\boldsymbol{r} - \boldsymbol{r}_3). \tag{2-2}$$

$\boldsymbol{T}$ is a 2×2 matrix that has $\boldsymbol{r}_1$-$\boldsymbol{r}_3$ as the first column and $\boldsymbol{r}_2$-$\boldsymbol{r}_3$ as the second column and $\lambda_3 = 1 - (\lambda_1 + \lambda_2)$.

Having the velocity, $\boldsymbol{v}$, at any point in the domain, it is quite straightforward to define the particle's new position. A first-order predictor-corrector method with adaptive time step control is applied in the current particle tracking model. Every time increment, Δt, the new particle position is defined in two steps, where first predictor step is:

$$\boldsymbol{r}_p(t + \Delta t) = \boldsymbol{r}(t) + \boldsymbol{v}\big(\boldsymbol{r}(t)\big)\Delta t. \tag{2-3}$$

Then Eq.2-1 defines the new particle's velocity $\boldsymbol{v}\left(\boldsymbol{r}_p(t + \Delta t)\right)$. The particle is moved to its new position defined by the corrector step:

$$\boldsymbol{r}(t + \Delta t) = \boldsymbol{r}(t) + \boldsymbol{v}\left(\boldsymbol{r}_p(t + \Delta t)\right)\Delta t. \tag{2-4}$$

The presented predictor-corrector technique prevents particles from reaching the edge of a fracture with no-flow boundary conditions.

The particle movement through an unstructured grid on a DFN requires determination of triangular element where particle resides at a current computational time step. This is most efficiently accomplished with an edge-crossing test. The particle's movement inside one fracture is straightforward. After defining the triangular element currently occupied by the particle, the instantaneous velocity is calculated by Eq. 2-1 followed by Eq. 2-3 and Eq. 2-4, which determines the particle's position at the end of the time step.

When the particle enters an element adjacent to fracture intersection, the distance between the current particle position and the intersection is computed. If the distance is smaller than the particle's movement during the last time step, then one predictor step (Eq. 2-3) is done and test on crossing the intersection line is performed. If true, the particle is moved to line representing the fracture intersection.

Being located on the intersection line implies that the particle is on the common edge of four triangular elements including the original one. Two of the elements belong to each of the two intersecting fractures. It is then required to decide into which element the particle will go at the next time step. The downstream element is chosen randomly with probability proportional to the outgoing flux. If there are two elements with outgoing flow, and the groundwater flux interpolated to them are $\boldsymbol{q_{e1}}$ and $\boldsymbol{q_{e2}}$, then the element 1 will be chosen if $u \le \frac{|\boldsymbol{q_{e1}}|}{|\boldsymbol{q_{e1}}|+|\boldsymbol{q_{e2}}|}$, where u is a generated random number between 0.0 and 1.0. The chosen triangular element dictates the next fracture where particle continues to travel.

2.3 Verification Tests

The 4-fracture DFN shown in Fig. 2-7 was used for verification of the flow and particle tracking capability. The travel time through this DFN can be deduced based on an equivalence to an electrical circuit, where fractures play the role of resistors. In this case particles travel time through the DFN may be determined analytically and compared to the numerical results.

Three horizontal rectangular fractures are connected through one vertical fracture (Fig. 2-7). Pressure boundary conditions are applied on $-x$ and x faces of the domain, 2 MPa and 1 MPa, respectively. Fluid flow goes from left to right side of the domain and obeys Darcy's Law:

$$Q = -\frac{kA(\Delta P)}{\mu L}, \tag{2-5}$$

where Q is a fluid discharge, k is a fracture permeability, A is a cross sectional area, ΔP is the applied pressure drop, μ is fluid viscosity, and L is a length of fluid path. Darcy's Law for fluid flow is an analogy to Ohm's Law for electrical circuit, leading to:

$$Q = -\frac{\Delta P}{R}, \quad R = \frac{\mu L}{kA} \ . \tag{2-6}$$

To calculate total flow in the DFN, the equivalent resistor network (Fig. 2-7 insert) is used. The total resistance R in the network is

$$R = R_1 + \frac{(R_{24}+R_4)\cdot(R_{24}+R_3)}{R_{24}+R_4+R_{24}+R_3} \ . \tag{2-7}$$

Once Q is computed, the Darcy flux, q, and flow velocity, $v = q/n$, where n is porosity, are calculated analytically, thus obtaining a theoretical value of particle travel time, t_{th}.

The fluid viscosity is μ=1.002[Pa · s], the cross section A is constant all over the DFN, where A=0.01[m^2]. The length, L, of R_1, R_3, and R_4 paths is 0.9 [m], the length of the R_{23} and R_{24} paths is 0.2 [m]. Two tests of the flow solution and particle tracks were performed. In the first test, the fracture permeability k is constant for every fracture in the DFN: k_1=k_2=k_3=k_4=2.5 × 10^{-13} [m^2]. In the second test fracture 3, the bottom fracture in the domain, is giving higher permeability k_3=2.5 × 10^{-12} [m^2], and k_1=k_2=k_4=2.5 × 10^{-13}[m^2].

The numerical results of steady state flow solutions are shown in Fig. 8 for both tests. In the first test (Fig. 2-8a) fluid pressure gradually decreases from left to right side of the domain, it does not show significant difference between the top and bottom fractures. In the second case (Fig. 2-8b), as a result of higher permeability on fracture 3, the pressure on it is lower than on fracture 4. Therefore, in the second test, the pressure gradient is significantly lower on the right side of the domain than in the first case.

Particle transport numerical experiments were performed for both tests. Initially, all particles are placed on the inflow boundary side, on the left edge of fracture 1 (Fig. 2-7) moving towards fracture 2. When they reach the first intersection, particles choose one of two paths to the outflow boundary: through the top (fracture 3) or bottom (fracture 4). Fig. 2-9 shows particle trajectories of 50 particles. In the first test (Fig. 2-9a) flow in the two paths are the same and particles are equally apportioned between two paths. The distribution is significantly different in the second test (Fig. 2-9b), where the bottom path has a higher flow. However, the probability of choosing the way through lower permeability fracture is nonzero, therefore we observe a few particles traveling through the top fracture of the DFN.

The measured numerically and calculated analytically values of particle travel time for both tests are giving in Table 2-1.

2.4 Application to the Forsmark Site

The Swedish Nuclear Fuel and Waste Management Company (SKB) recently submitted an application for a license to construct a final repository for spent nuclear fuel. SKB is owned by the utilities producing electricity by nuclear power in Sweden and is responsible for the handling of all spent nuclear fuel and other radioactive wastes generated as a result of nuclear power production in Sweden. If the application is approved and the repository constructed within the estimated time frame, it will be among the first, if not the very first, deep geological repository for spent nuclear fuel. The repository is to be constructed at approximately 500 m depth in crystalline bedrock according to the KBS-3 principle (Svensk Kärnbränslehantering, 2011), which implies a system of independently functioning barriers. The Forsmark area is located in northern Uppland within the municipality of Östhammar, about 120 km north of Stockholm. The Forsmark area consists of crystalline bedrock that has been affected by both ductile and brittle deformation. The ductile deformation has resulted in large-scale, ductile high-strain belts and more discrete high-strain zones. Tectonic lenses, in which the bedrock is less affected by ductile deformation, are enclosed between the ductile high strain belts. The proposed repository location is in the north-westernmost part of one of these tectonic lenses. The brittle deformation has given rise to reactivation of the ductile zones in the colder, brittle regime and the formation of new brittle fracture zones of variable size.

As a demonstration test of the new DFN capability, the DFN inferred (Svensk Kärnbränslehantering, 2011) for Forsmark was simulated. The purpose of the numerical experiments is to demonstrate that the new capability can be deployed in applications. Three realizations were created using the parameters shown in Table 2-2. A three-dimensional domain of size 1000 m × 1000 m × 1000 m was used. The three sets of fractures are of circular shape and oriented according to Fisher distribution:

$$f(\theta) = \frac{\kappa \cdot sin\theta \cdot e^{\kappa \cdot cos\theta}}{e^{\kappa} - e^{-\kappa}}, \tag{2-8}$$

where θ is the deviation of the fracture pole orientation from the mean orientation and the parameter $\kappa > 0$ is the concentration parameter. The concentration parameter quantifies the degree of clustering; values approaching zero represent a uniform distribution on the sphere and large values imply small average deviations from the mean direction.

The fractures sizes at Forsmark obey a truncated power-law distribution with lower and upper cut-off radii of R_0 and R_x, respectively. The power-law distribution is sampled by first generating a random number u from a uniform distribution between *0.0* and *1.0*. The radius is then calculated as

$$R = R_0 \cdot \left[1 - u + u \cdot \left(\frac{R_0}{R_x}\right)^{\alpha}\right]^{-1/\alpha}. \tag{2-9}$$

Fracture transmissivity, σ, was estimated using a power-law relationship a correlated transmissivity model (Svensk Kärnbränslehantering, 2011)

$$\log(\sigma) = \log\left(a \cdot R^{\beta}\right), \tag{2-10}$$

with parameters a=1.6 ×10^{-9}, β=0.8. The fracture aperture, b, and fracture permeability, k, were partially correlated to fracture size and calculated using the cubic law (Adler et al. 2012)

$$\sigma = \frac{b^3}{12}, \quad k = \frac{b^2}{12}. \tag{2-11}$$

Three fracture sets are represented. The stochastic parameters for the three fracture sets are given in Table 2-2.

Pressure boundary conditions are applied to horizontal faces of the domain, assuming fluid flow from bottom to top along the z direction. The steady state pressure solutions and permeability fields are shown in Fig. 2-10 for three realizations of the network.

In the first numerical experiment on particle tracking on the DFN all particles were placed initially on a small region (20m × 20m × 20m) in the center of inflow boundary. This experiment allows us to observe how fast particle trajectories diverge from their initial common location (Fig. 2-11a) due to high topological variety of the DFN and probabilistic method used on fracture intersection. Final positions of particles are captured at the out-flow boundary and plotted in Fig. 2-11b. A wide dispersion in space is observed, but so is channeling, with higher particle density on large fractures edge. The travel time cumulative distribution of 10000 particles is shown in Fig. 2-12. It is well approximated by a power-law distribution. It should be noted that power-law distributions are fundamentally inconsistent with the advection dispersion equation.

In the second set of next numerical experiment, all particles were initially equally distributed over all fracture edges at in-flow boundary of the domain. The travel time to the out-flow boundary was measured. The complementary cumulative distribution (exceedance probability) is plotted in Fig. 2-13 for three realizations. The distributions generally follow a power-law except for the large plateau visible in each. This plateau is attributed to a small number of large fractures in the domain. While not an issue in applications, such realization-to-realization variability is not desirable for theoretical studies of transport in fracture networks. Larger domains will be necessary to ensure ergodic conditions and eliminate the large realization-to-realization variability.

2.5 Hybrid DFN/Volume Meshes

The ability to merge DFN meshes with conventional volume-filling meshes is a practical capability required for applications. These hybrid DFN/volume meshes are needed for two reasons. First, it is convenient in applications to use a detailed DFN mesh in parts of the domain but use an equivalent porous medium representation and conventional volume-filling mesh outside the main region of interest. This nested-mesh strategy allows for detailed investigations of flow and transport in the area near a potential repository while also modeling a larger region that is natural for the regional boundary conditions. Experience has shown that this nested mesh approach is more transparent and involves fewer approximations than the alternative approach that attempts to match boundary conditions from a larger domain to a smaller domain. Second, repository designs in crystalline rock typically involve tunnels, ventilation shafts, and emplacement boreholes that are filled with buffer and backfill. Such engineered features are not fractured media and require a porous medium representation and a volume-filling mesh to represent.

The DFN meshing process was extended to create hybrid DFN/volume meshes. The approach is illustrated in Fig. 2-14. In this example, the interior of a cylinder is to be meshed and merged with a DFN grid in the nearby rock volume. A DFN is first generated using the procedures described previously. The generated DFN ignores the volume to be meshed. However, before the DFN is meshed, interfaces between fractures and the cylinder to be meshed are identified. A two-dimensional mesh is then created on each fracture in a way that conforms to the fracture intersections and to the fracture-volume interfaces (Fig. 2-14a). The fracture grids are then merged. In the second step, nodes on the fractures within the volume to be meshed are removed (Fig. 2-14b). A tetrahedral mesh that conforms to the fracture intersection is then created within the cylinder. In the final step, the tetrahedral mesh and the DFN mesh are merged and duplicate nodes removed (Fig. 2-14c). The LaGriT software (Los Alamos Grid Toolbox, 2013) was used to execute the meshing calculations.

2.6 Summary and Status of the Work

Several new capabilities were summarized in this report:

1. The previously introduced DFN generation and meshing capability was matched to the highly parallel flow and transport simulator PFLOTRAN (Lichtner et al. 2013), thus allowing for flow solutions on large DFN grids.
2. Particle-tracking capability, a key component in workflows for evaluating nuclear waste repositories, was developed.
3. The DFN flow and transport capabilities were verified in two tests using a 4-fracture configuration.
4. DFN generation, parallel flow solutions, and particle tracking were demonstrated at application-relevant scales using fracture parameters from a well-characterized site.

There are two overarching motivations for this work on DFN modeling tools. First, the tools under development will be necessary should the UFDC be asked to evaluate a potential future site in fractured rock. Second, there are several unresolved generic scientific issues associated with flow and transport in fractured rock that these tools will be able to address.

The ability to produce high-quality computational DFN meshes suitable for state-of-the-art parallel subsurface flow codes is a unique capability that will allow large DFNs to be considered in applications. The ability to reliably track particles on DFN control volume grids is also a unique capability.

Of the component pieces of the work, the generation of a high-quality DFN computational mesh is largely complete for the situation where the space between fractures is not meshed. Further work is required to develop meshing capability for the spaces between fractures, which may be needed to address some of the unresolved issues associated with transport in fractured rock. In addition, testing of the DFN capability has revealed that the current computational bottleneck is in the DFN generation step. Additional optimization of the algorithm and software would be advantageous to enable larger and more detailed DFNs to be considered.

Table 2-1. Numerical and analytical results of particle travel time in verification tests.

	Travel Time Analytical [s]	Travel Time Numerical [s]	Error [%]	Mass fraction per path, Analytical	Mass fraction per path, Numerical	Error [%]
Test 1	1.802×10^3	1.801×10^3	0.047	0.5, 0.5	0.478, 0.522	
Test2, path1	1.025×10^3	1.010×10^3	0.014	0.905	0.96	
Test 2, path2	2.926×10^3	2.930×10^3	0.001	0.095	0.04	

Table 2-2. DFN parameters used in simulations of the Forsmark site.

Set	Orientation Distribution: Fisher			Size Distribution: Power Law			Fracture Density
	Mean Trend	Mean Plunge	Concentration κ	α	R_x, m	R_0, m	Number of fractures in 1 km^3
1. (NS)	90.0°	0.0°	21.7	2.5	500	15	2093
						20	1019
						25	583
2. (NE)	135.0°	0.0°	21.5	2.7	500	15	2000
						20	920
						25	503
3. (HZ)	360.0°	90.0°	8.2	2.38	500	15	2285
						20	3887
						25	7711

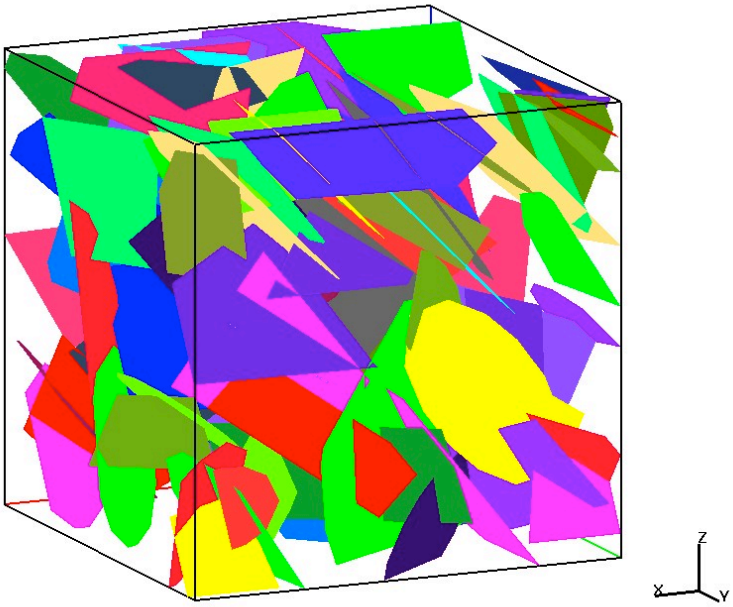

Figure 2-1. Example of stochastically generated discrete fracture network with 100 individual fract a domain of size 8 × 8 × 8 m. Each fracture in the network is shown by different color.

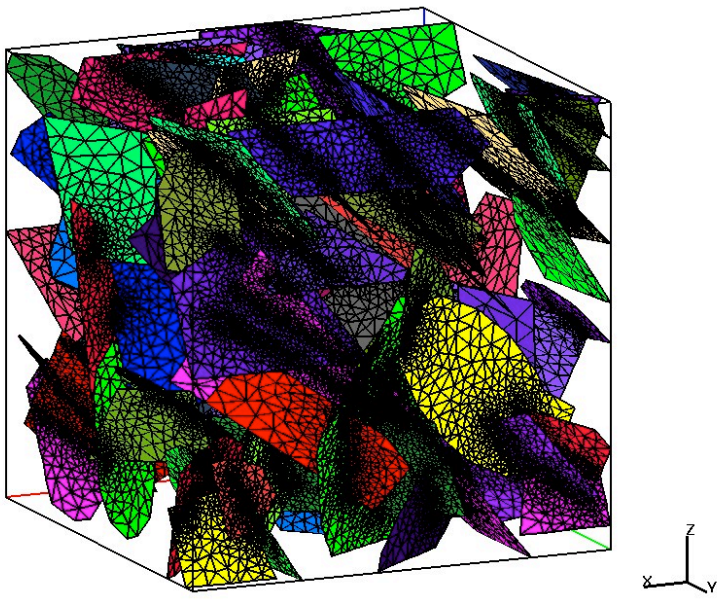

Figure 2-2. Same as Figure 2-1 but with the computational grid visible. Note that the mesh resolution is fine near intersections and coarse away from fracture intersections.

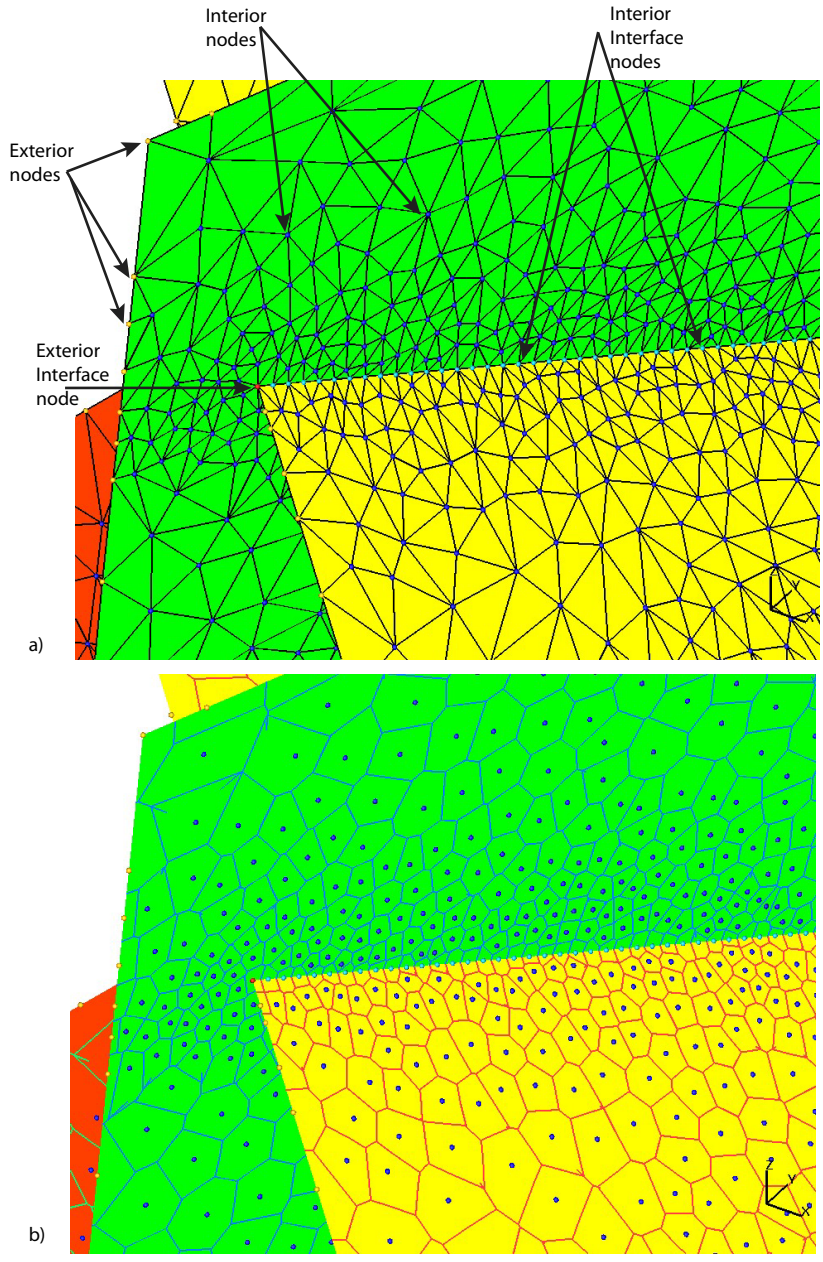

Figure 2-3. Two intersecting fractures showing conforming Delaunay triangulations (a) and Voronoi control volumes (b). The Delaunay triangulation conforms to the fractures' intersection without distorting the fracture lines intersections. Four types of nodes are distinguished on computational grid (a). Along the line of intersection control volume cells are common to both fractures (b).

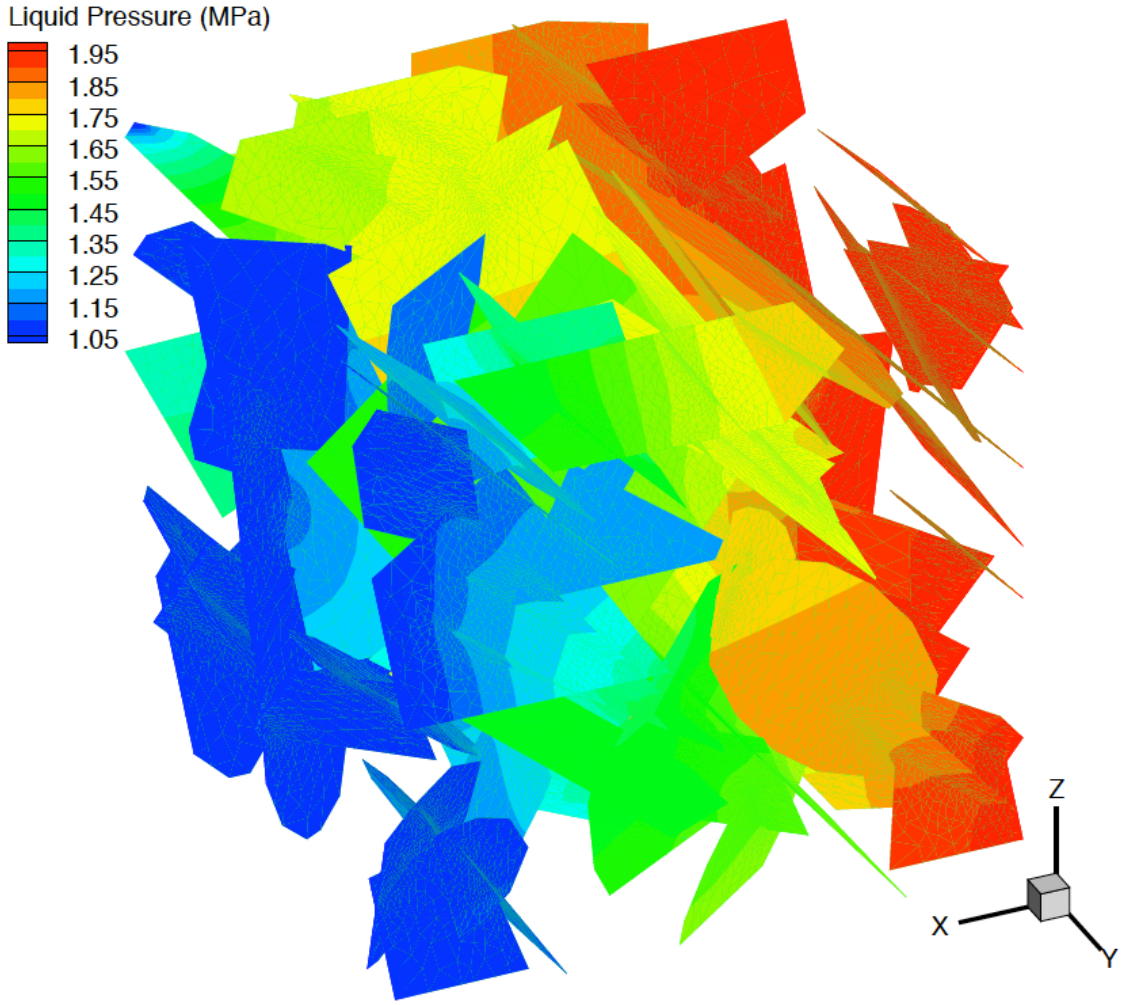

Figure 2-4. Example of steady state pressure solution on a 100-fracture DFN. The boundary conditions are applied to the *x* faces of 3D domain.

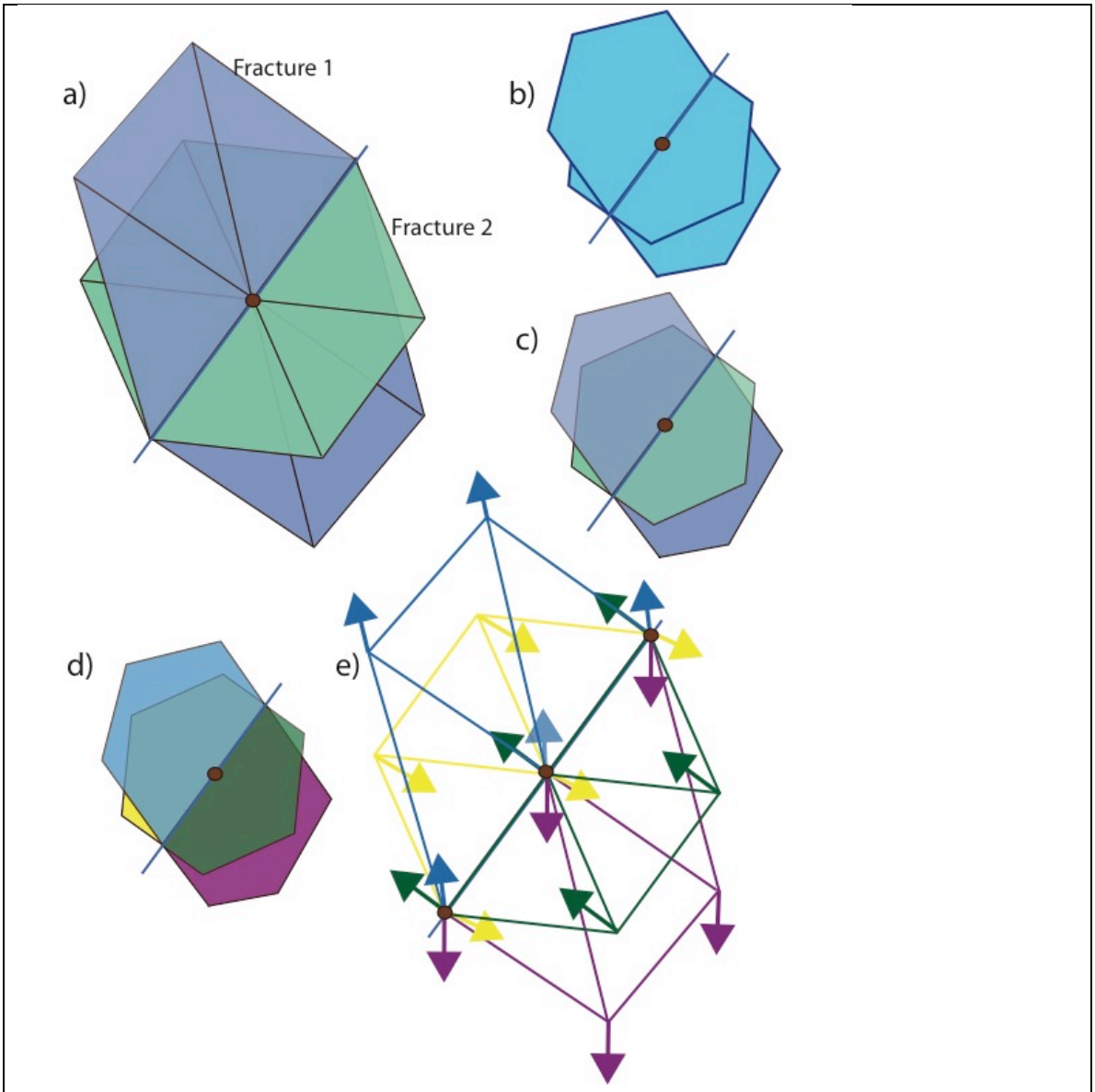

Figure 2-5. Illustration of the different representations of control volumes and velocities on fracture interfaces. The interior interface node shown in a) is on the intersection of two fractures, fracture 1 and fracture 2, and belongs to both fractures. Each single 3-D control volume cell (b) is used for the purposes of obtaining the flow solution. The control volume cell on the intersection is split into two 2D polygons (c), one for each of the intersecting fracture. Those polygons are further divided at the intersection line; in (d) the blue and purple polygons belong to fracture 1, and the yellow and green polygons belong to fracture 2. The flow velocities are reconstructed on each of the split polygons, with the result (e) being that four velocities are associated with each interior node.

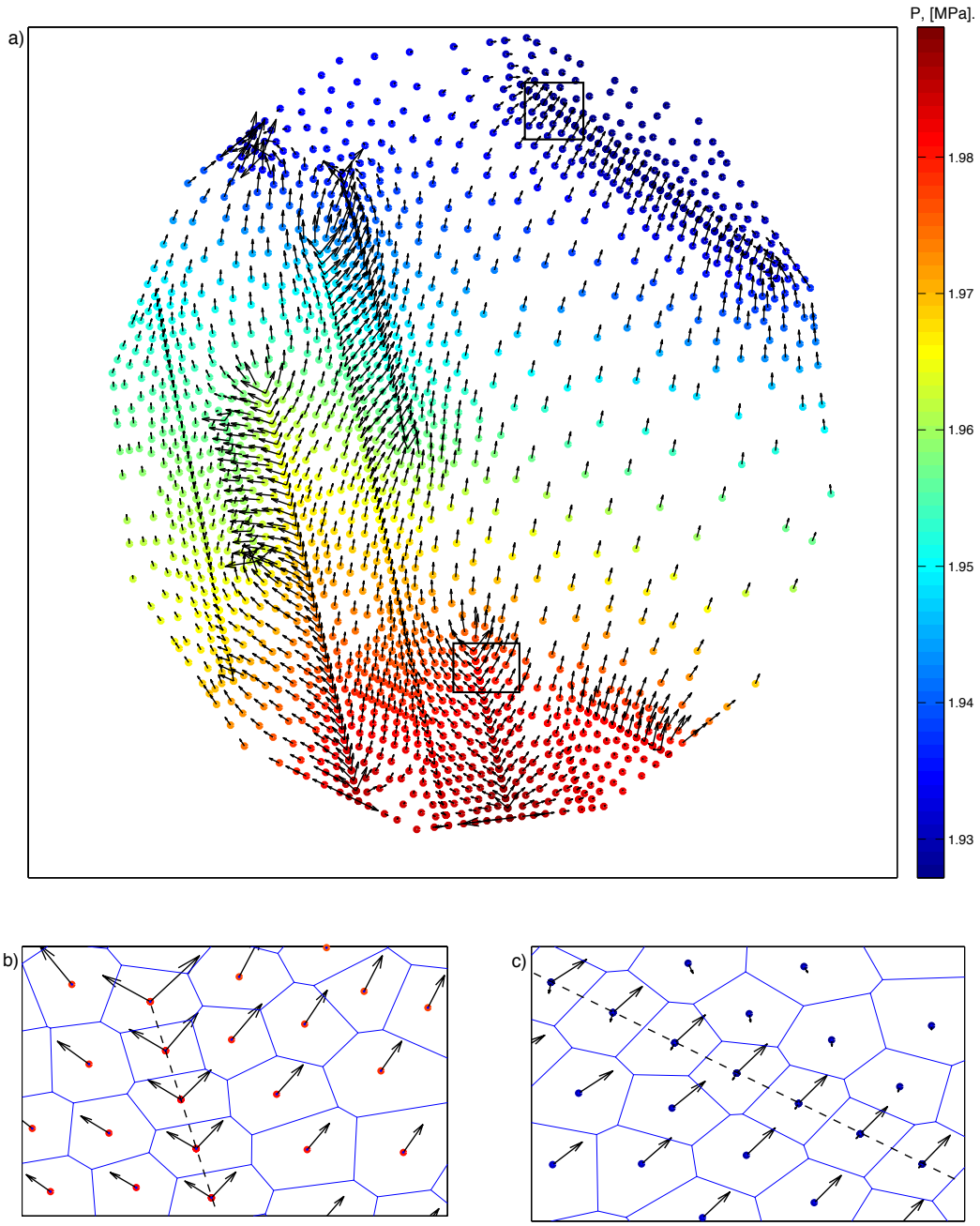

Figure 2-6. a) The flow field of individual fracture extracted from a DFN of 10^3 fractures is shown in *xy* plane. The nodes are colored by their corresponding pressure value: low pressure is indicated by dark blue colors, high pressure is shown by light red colors. The black arrows represent reconstructed flow field velocities. b) Detail showing a fracture intersection with flow incoming from the intersecting fracture and moving in both directions on the represented fracture. c) Detail showing another fracture intersection. At this intersection flow flow is toward the intersection and into the intersecting fractures. Note that two velocities are shown for each interior interface node. There are two corresponding velocities on the intersecting fracture (not shown).

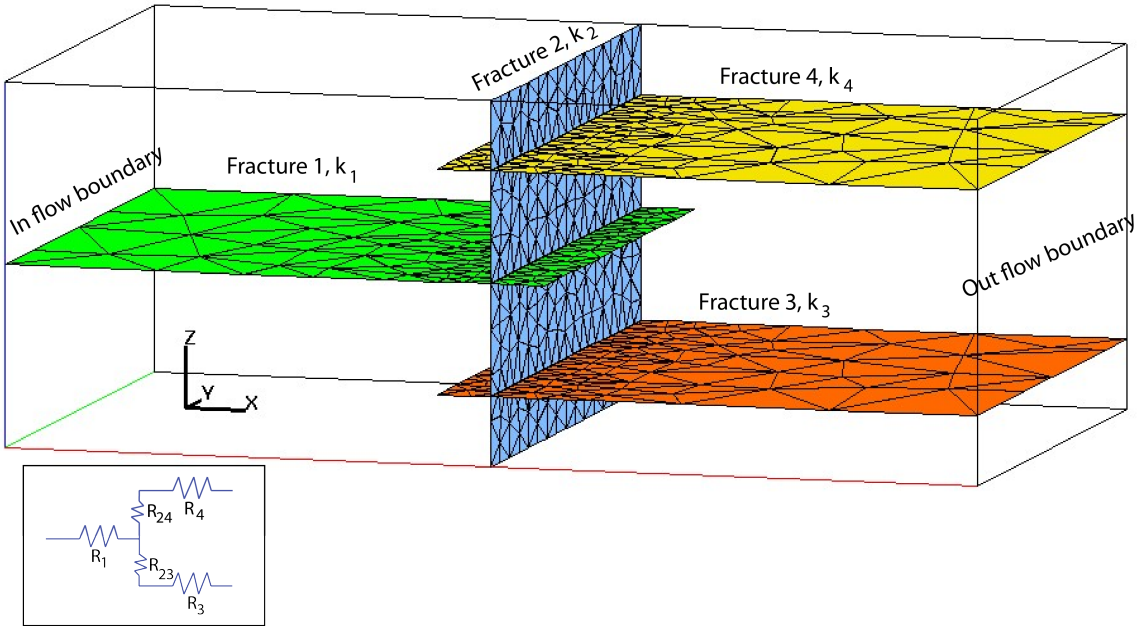

Figure 2-7. Discrete fracture network of 4 fractures used for a verification test of the new particle-tracking capability. Boundary conditions are applied to *x* faces of the domain; flow goes from the left to right side of the DFN. The domain size is 1.8 × 1.0 × 0.65 m, and each fracture thickness is 0.01 m. The insert shows an electrical circuit that is an analog to the DFN for purposes of calculating the verification target values of flow and travel time.

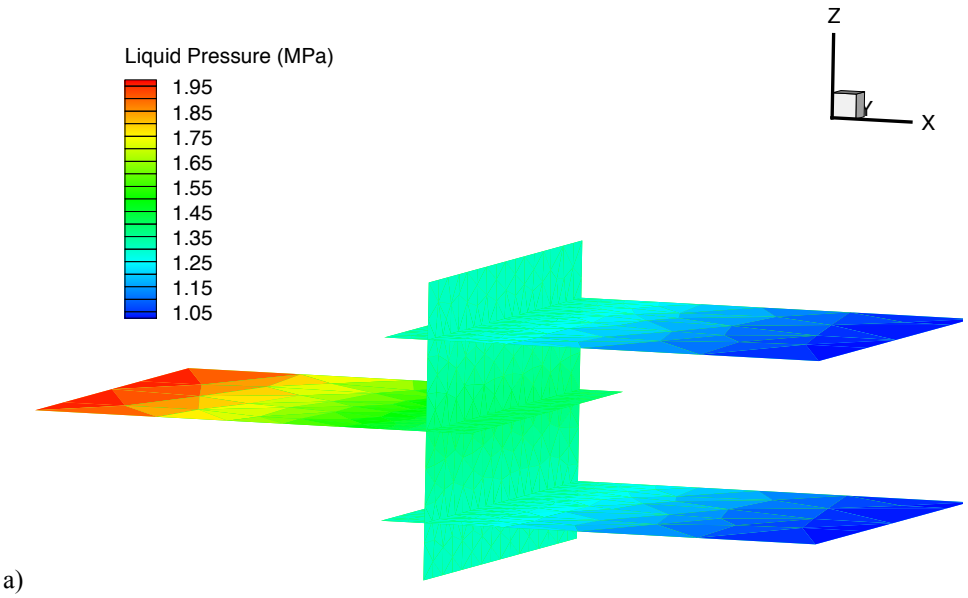

a)

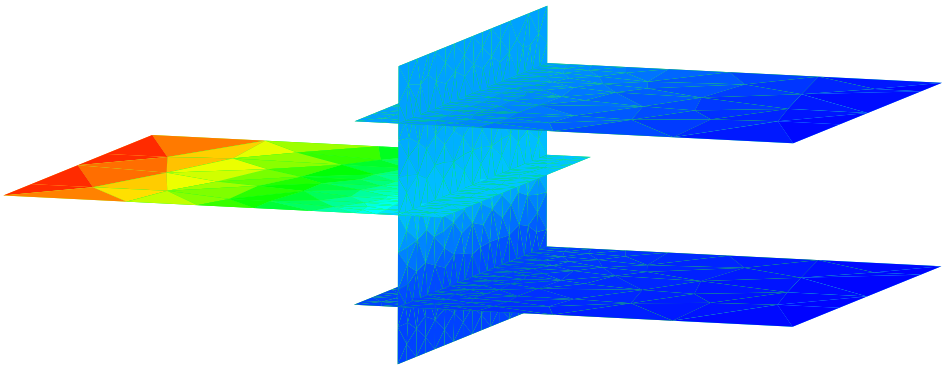

b)

Figure 2-8. The steady state flow pressure solutions obtained for the 4 fractures DFN used in the two verification tests. Light red colors correspond to high pressure. a) Pressure solution obtained for DFN where all fractures are designated equal permeability value, $k_1=k_2=k_3=k_4=2.5\cdot10^{-13}$ m^2. b) Pressure solution obtained for the same DFN, where fracture *3* is giving higher permeability, $k_3=2.5\cdot10^{-12}$ m^2, $k_1=k_2=k_4=2.5\cdot10^{-13}$ m^2.

a)

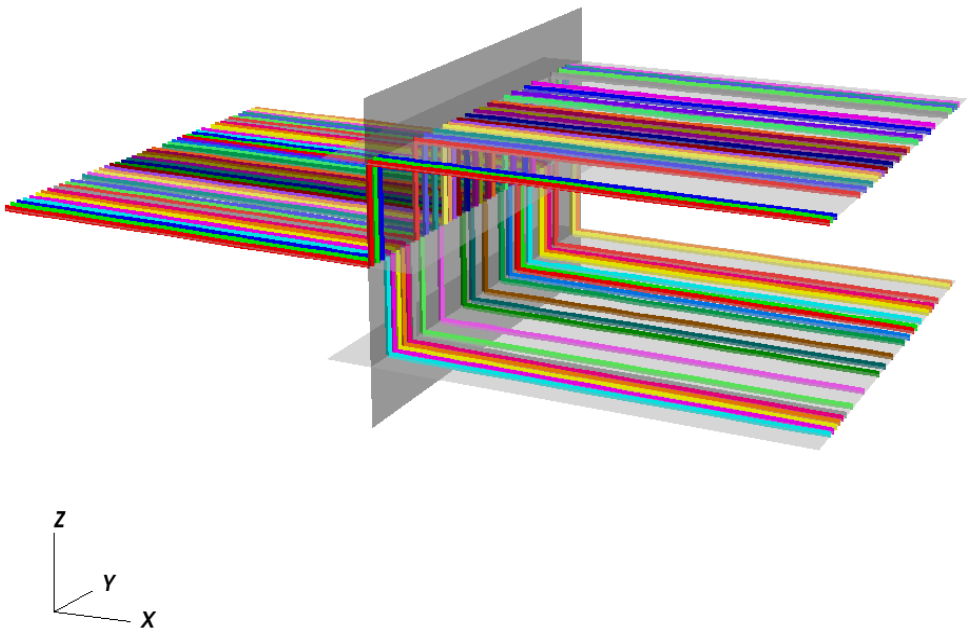

b)

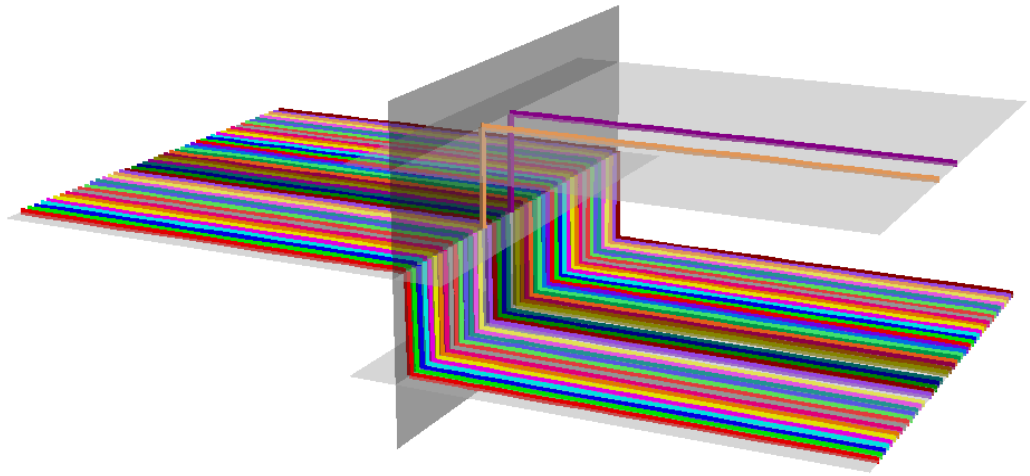

Figure 2-9. Particle tracks on 3-fracture verification tests. In a) all the fractures are given the same permeability value, and approximately the same number of particles choose to travel through fracture 3 as through fracture 4. In b) fracture 3 (bottom fracture) is given higher permeability. As a result, more particles travel through bottom path of the DFN.

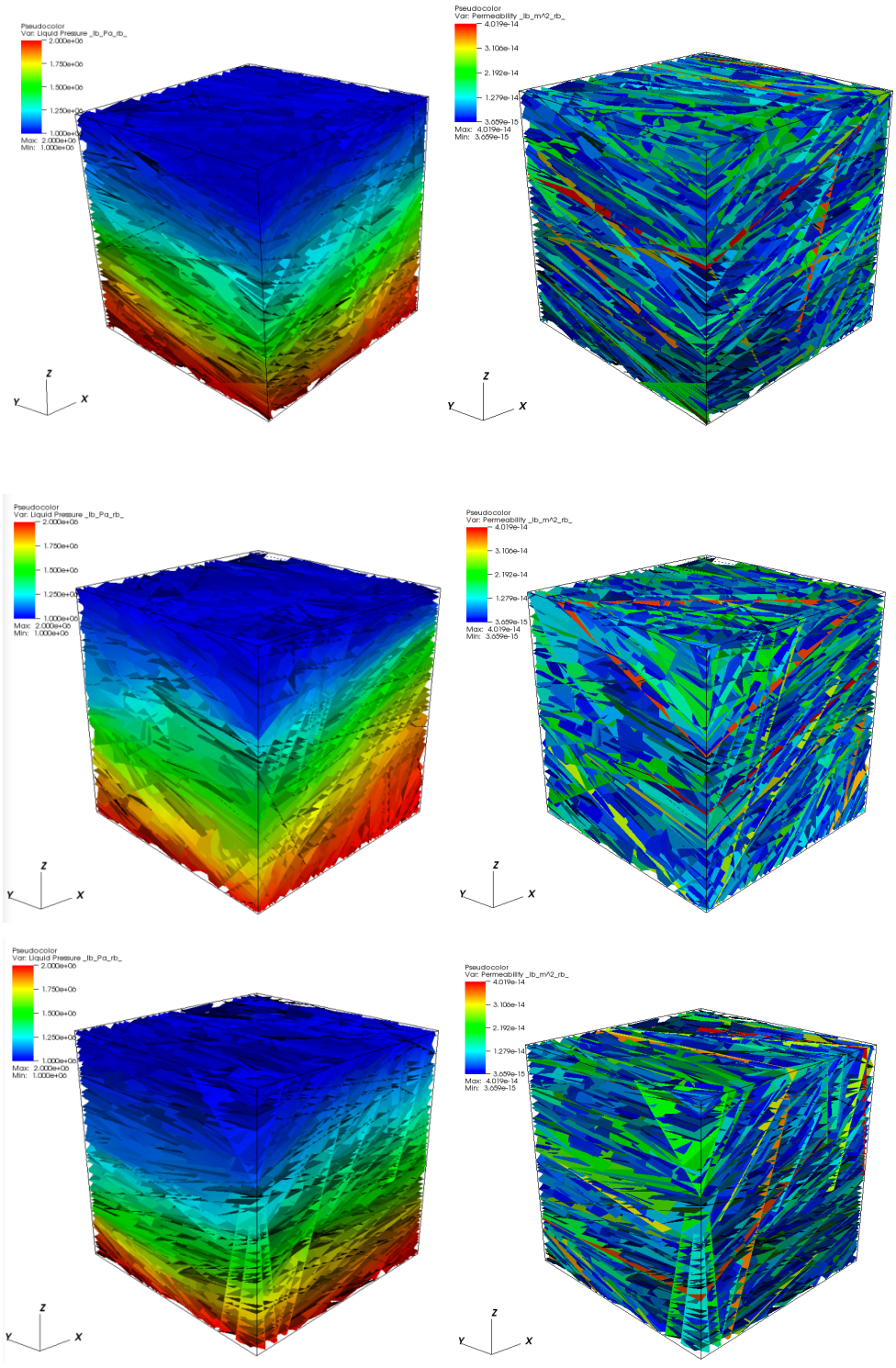

Figure 2-10. Steady state flow solution (left) and permeability (right) on three DFN realizations based on data from the Forsmark site.

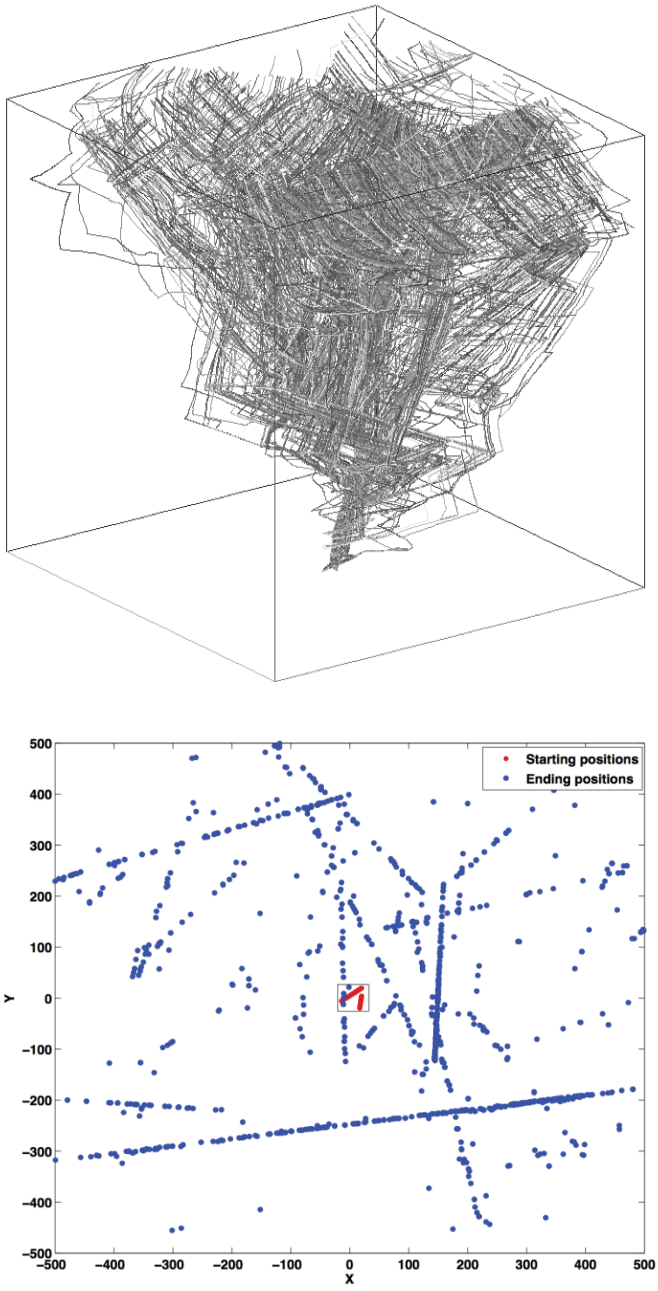

Figure 2-11. a) 2000 particles trajectories starting from one region in the middle of the in-flow boundary side trajectories diver fast and fill up the domain. b) Particles final positions at in-flow (red) and out-flow (blue) boundaries.

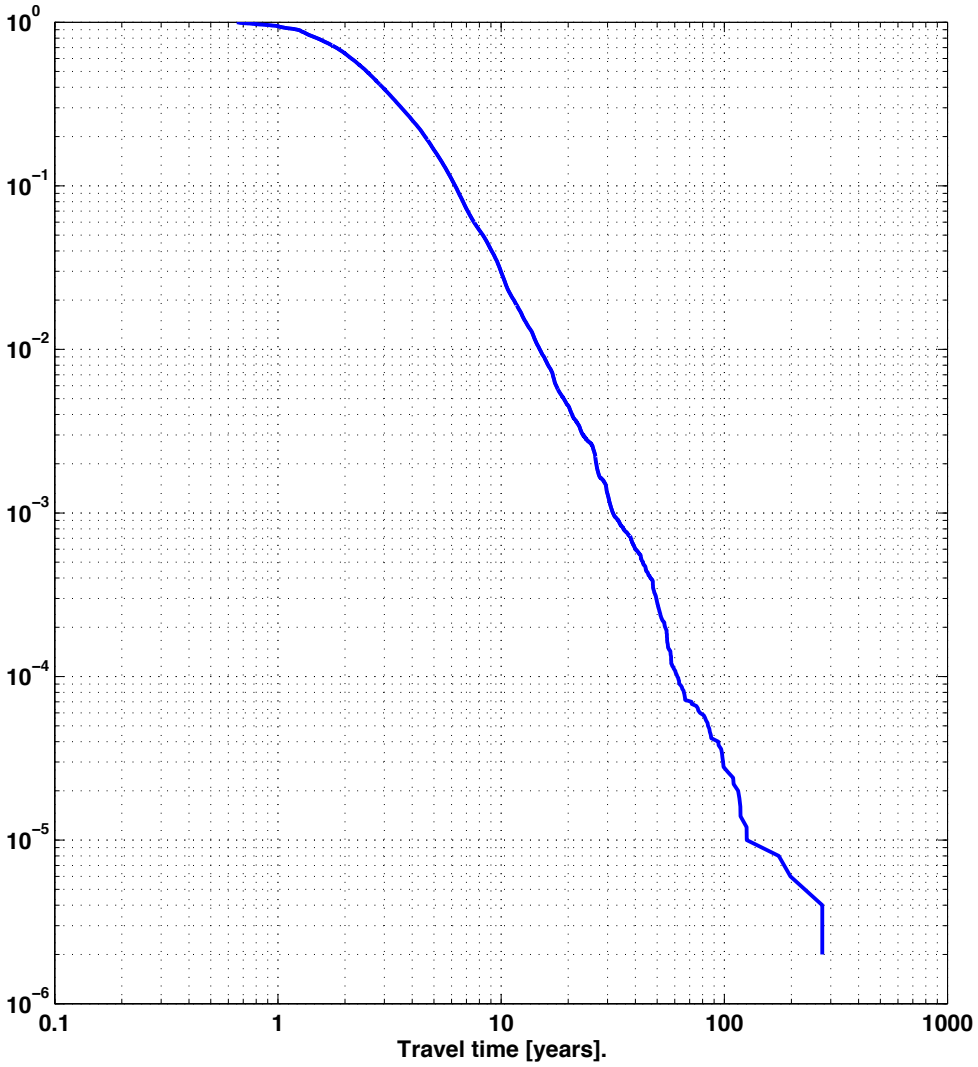

Figure 2-12. Travel time distribution for 5×10^5 particles that enter the DFN from a region in the middle of in-flow boundary side.

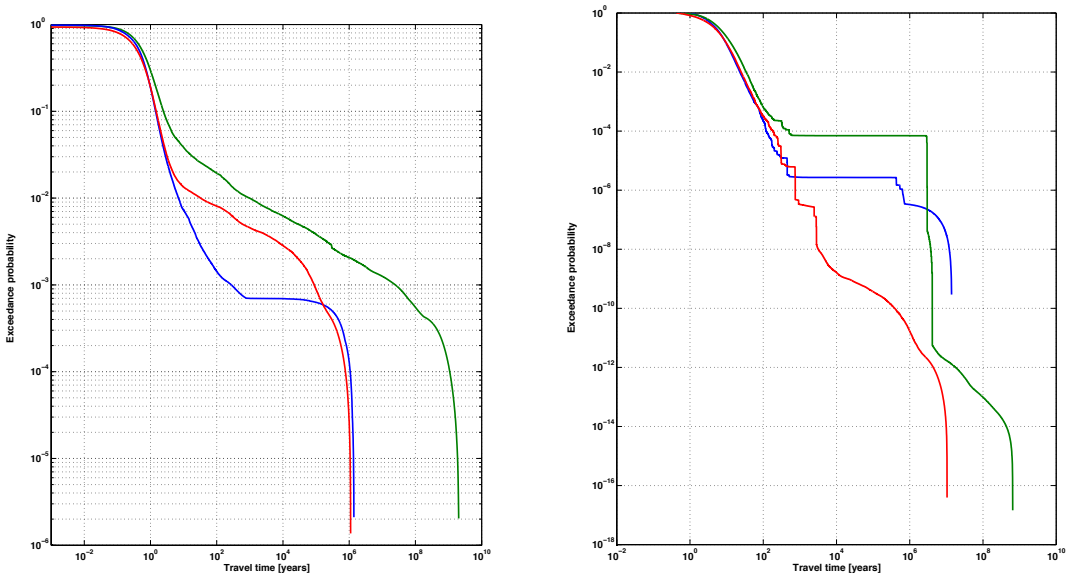

Figure 2-13. Cumulative distribution of particle travel time: a) uniformly weighted at starting positions; b) flux-weighted at starting positions.

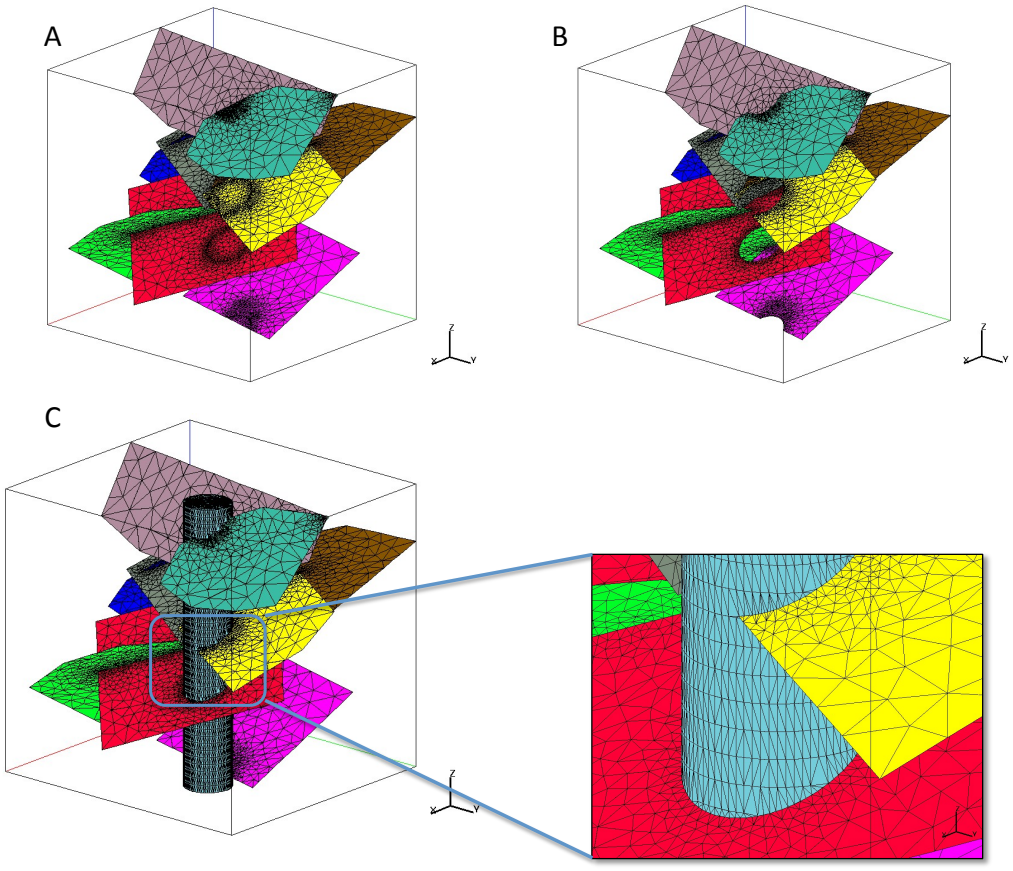

Figure 2-14. Example showing the creation of a hybrid tetrahedral/DFN mesh. Such hybrid meshes are needed in applications.

2.7 References

Adler, P.M., Thovert. J.-F., Mourzenko, V.V., Fractured Porous Media, Oxford University Press, 2012.

Arbogast T., Cowsar L. C., Wheeler M. F., Yotov I., 2000. Mixed finite element methods on non-matching multiblock grids, SIAM Journal Numerical Analysis 37(4), 1295-1315.

Barenblatt, G.I., Zheltov Y.P., Kochina I.N., 1960. Basic concepts in the theory of seepage of homogeneous liquids in fissured rocks. Journal of Applied Mathematics of Mechanics (English Translation) 24, 1286–1303.

Botros F. E., Hassan A. E., Reeves D. M., and Pohll G., 2008. On mapping fracture networks onto continuum, Water Resources Research 44, W08435, doi:10.1029/2007WR006092.

Cordes C. and Kinzelbach W., 1992. Continuous groundwater velocity field and path lines in linear, bilinear, and trilinear finite elements, Water Resources Research 28(11), 2903-2911.

Cvetkovic V., Painter S., Outters N., and Selroos J.-O., 2004. Stochastic simulation of radionuclide migration in discretely fractured rock near Aspo hard rock laboratory, Water Resources Research 40, W02404, doi:10.1029/2003WR002655.

Duguid J.O. and Lee P. C. Y., 1977. Flow in fractured porous rock, Water Resources Research 13, 558–566.

Ewing R., Lazarov R., Lin T., and Lin Y., 2000. The mortar finite volume element methods and domain decomposition. East-West Journal of Numerical Mathematics 8, 93–110.

Jackson, C., Hoch, A., Todman, S., 2000. Self-consistency of a heterogeneous continuum porous medium representation of a fractured medium, Water Resour. Res. 36 (1), 189-202.

Hyman, J.D., Gable, C.W., and Painter, S.L., 2014. Conforming Delaunay Triangulation of Stochastically Generated Three Dimensional Discrete Fracture Networks : A Feature Rejection Algorithm for Meshing Strategy (Under Review at SIAM Sci. Comp.).

Los Alamos Grid Toolbox, LaGriT, 2011. Los Alamos National Laboratory, <http://lagrit.lanl.gov>.

Lichtner, P.C., Hammond, G.E., Bisht, G.,Karra, S., Mills, R.T., and Kumar, J., 2013. PFLOTRAN User's Manual: A Massively Parallel Reactive Flow Code.

Mosé R., Siegel P., Ackerer P., and Chavent G., 1994. Application of the mixed hybrid finite element approximation in a groundwater flow model: Luxury or necessity?, Water Resources Research 30(11), 3001–3012, doi:10.1029/94WR01786.

Neuman, S. P., 1987. Stochastic continuum representation of fractured rock permeability as an alternative to the REV and discrete fracture concepts. In Farmer I.W., Daemen J. J. K., Desai C.S., Glass C.E. Neuman S. P. (eds) Rock Mechanics, Proceedings of the 28th US Symposium, Tucson, Arizona. AA Balkema, Rotterdam.

Neuman, S. P., 2005. Trends, prospects and challenges in quantifying flow and transport through fractured rocks, Hydrogeology Journal 13, 124–147.

Painter S. and Cvetkovic V., 2005. Upscaling discrete fracture network simulations: An alternative to continuum transport models, Water Resources Research 41, W02002, doi:10.1029/2004WR003682.

Painter S., Cvetkovic V., Mancillas J., and Pensado O., 2008. Time domain particle tracking methods for simulating transport with retention and first-order transformation, Water Resources Research 44, W01406, doi:10.1029/2007WR005944.

Painter S., Gable C., and Kelkar S., 2011. Pathline tracing on fully unstructured control volume grids. Computational Geosciences 16(4) 1125–1134.

Pichot G., Erhel, J., de Dreuzy, J. R., 2010. A mixed hybrid Mortar method for solving flow in discrete fracture networks. Applicable Analysis: An International Journal 89 (10), 1629–1643.

Pruess K. and Narasimhan, T.N., 1985. A practical method to modeling fluid and heat flow in fractured porous media. Society Petroleum Engineers Journal 25(1), 14–26.

Pruess K., Oldenburg C., and Moridis G., 1999. TOUGH2 Users Guide, Version 2.0, LBNL-43134, Lawrence Berkeley National Laboratory, Berkeley CA.

Svensk Kärnbränslehantering AB, 2011. Long-term safety for the final repository for spent nuclear fuel at Forsmark, SKB TR-11-01, Svensk Kärnbränslehantering AB

Svensson U., 2001. A continuum representation of fracture networks: Part I. Method and basic test cases, Journal of Hydrology 250, 170–186.

Wang, Y.F., 2011. Research and Development Plan for Natural System Evaluation and Tool Development. U.S. Department of Energy.

Warren J.E. and Root P.J., 1963. The behavior of naturally fractured reservoirs. Society of Petroleum Engineers Journal 3, 245–255.

Zyvoloski G. A., 2007. FEHM: A control volume finite element code for simulating subsurface multi-phase multi-fluid heat and mass transfer. Los Alamos Unclassified Report LA-UR-07-3359.

Zyvoloski G. A, Robinson B. A, Viswanathan H. S., 2008. Generalized dual porosity: A numerical method for representing spatially variable sub-grid scale processes, Advances in Water Resources 31 (3) 535–544, DOI: 10.1016/j.advwatres.2007.11.006

This page left blank intentionally.

3 HYDROLOGIC FLOW IN LOW-PERMEABILITY MEDIA

3.1 Introduction

Water flow in clay media is an important process for geological disposal of high-level nuclear wastes. Clay/shale formations have been considered as potential host rock for geological disposal of high-level radioactive waste because of their low permeability, low diffusion coefficient, high retention capacity for radionuclides, and ability to self-seal fractures (Tsang et al., 2012). In geologic repositories for radioactive waste disposal, compacted expansive clay soils (bentonites) are also often considered as buffer materials within an engineered barrier system, to be placed in the repository tunnels between the radioactive waste and the host rock. The bentonite is usually compacted at low water content, and then progressively wetted by water from the surrounding host formation. As a result, an unsaturated zone may develop within the near field of a clay repository while the other regions of host rock remain saturated. The unsaturated wetting process is accompanied by bentonite swelling, which ensures acceptable sealing of open spaces between waste packages and the corresponding host formation. Accurately modeling both saturated and unsaturated flow in such clay materials is critical for assessing the performance of both clay rock and buffer materials for isolating radioactive wastes at a disposal site.

Water flow in porous media is traditionally described by Darcy's law. In 1856, Henry Darcy investigated the flow of water in vertical homogeneous sand filters in connection with the fountains of the city of Dijon in France. From his experimental results, Darcy empirically discovered that water flux is directly proportional to the hydraulic gradient. However, it has been well documented that Darcy's law is not adequate for clay media, as reviewed by Liu and Birkholzer (2013). For example, Hansbo (1960; 2001) reported that water flux in low-permeability clay is proportional to a power function of the hydraulic gradient when the gradient is less than a critical value, above which the relationship between water flux and gradient becomes linear for large gradient values. He explained this behavior by positing that a certain hydraulic gradient is required to overcome the maximum binding energy of mobile pore water. From their experimental results, Miller and Low (1963) also found the existence of a hydraulic gradient below which water is essentially immobile. Most recently, Xu et al. (2007) experimentally investigated the relationship between flux of deionized water and hydraulic gradient in individual microtubes with diameters ranging from 2 to 30 μm. They demonstrated that water flow in microtubes with diameters of larger than 16 μm is consistent with Darcy's law, but not for smaller diameters. In the latter cases, the relationship between water flux and hydraulic gradient becomes non-linear.

The studies mentioned above are all for saturated flow conditions. Laboratory test results seem to show that non-Darcian flow behavior becomes even more significant under unsaturated conditions. Cui et al. (2008) reported non-Darcian behavior for a range of observed hydraulic gradients under unsaturated conditions. Liu et al. (2012) developed a constitutive model for unsaturated flow when water can be considered as a power-law (non-Newtonian) fluid; the model is consistent with the data set of Cui et al. (2008). Note that Liu et al. (2012) probably were the first to report relative-permeability formulations for power-law fluids. Power-law fluids are common in the processes of enhanced oil recovery (EOR), such as chemical flooding. Thus, the work of Liu et al. (2012) could be applicable to modeling related EOR processes as well. As an effort to develop a general framework for modeling non-Darcian flow in low-permeability media, Liu and Birkholzer (2013) reported a new relationship between water flux and hydraulic gradient for both saturated and unsaturated water flow, and also developed an empirical formulation to relate permeability to a parameter characterizing non-Darcian flow behavior.

While considerable progress has been made for investigating non-Darcian flow in clay media, several key technical issues still need further research. We devote this report to addressing the following issues related to geological disposal of high-level nuclear waste in clay/shale formations.

One of the most important technical questions for the performance of a shale/clay repository is the relative importance of advection versus diffusion in the damage zone near underground tunnels/drifts. In Section 3.3, we demonstrate that under normal conditions (under which there are no intersections between tunnels/drifts and conductive geological structures, such as faults), the water flow velocity in the damage zone, as a result of non-Darcian flow behavior, is extremely small such that solute transport is dominated by diffusion, rather than advection. This is desirable because diffusion is a much slower transport mechanism for radionuclides.

As previously indicated, unsaturated flow is an important process for a shale/clay repository. To model the unsaturated flow process, we need relative permeability as a function of water saturation. In Section 3.4, we show that unless non-Darcian flow behavior is considered, significant errors can occur in the "measured" relative-permeability values. This is generally supported by an experimental data set.

A geological repository is subject to temperature evolution in the near field as a result of heat generated by nuclear waste. Thus, incorporating the impact of temperature on non-Darcian flow behavior is needed for assessing repository performance. However, studies on the subject are very limited in the literature. As a first step to resolve this issue, we propose a hypothesis to consider the temperature impact based on limited test results from the petroleum literature (Section 3.5).

Previous studies have only considered non-Darcian flow in one-dimensional and/or isotropic media (Liu and Birkholzer, 2013). However, shale formations consist of bedding layers and are therefore generally anisotropic. To consider the bedding effects, we present an empirical relationship between water flux and hydraulic gradient for non-Darcian water flow in anisotropic cases (Section 3.6).

3.2 A Review of Relationships between Water Flux and Hydraulic Gradient

Non-Darcian flow behavior is characterized by non-linear relationships between water flux and hydraulic gradient. This section discuses several selected relationships available in the literature for completeness, while a more detailed review is given in Liu and Birkholzer (2013).

The well-known flux-gradient relationship is Darcy's law given by

$$q = Ki \tag{3-1}$$

where q (m/s) is water flux, K (m/s) is hydraulic conductivity and i (-) is hydraulic gradient. The above equation only includes magnitudes of variables for one-dimensional flow and therefore q, K, and i are all positive. A similar treatment is used, for convenience, for all the other relationships to be discussed in this section.

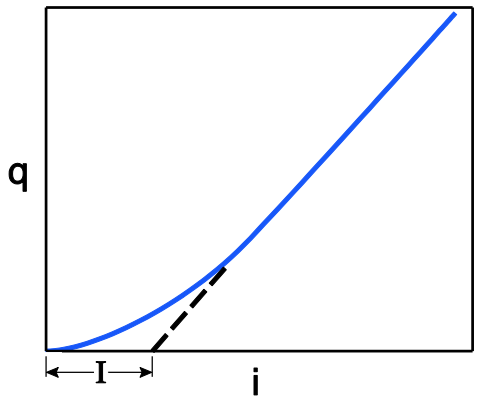

Figure 3-1. Definition of threshold hydraulic gradient

To incorporate non-Darcian flow behavior in clay soils, Swartzendruber (1961) introduced a modified Darcy's law based on a relation for *dq/di*:

$$\frac{dq}{di} = K(1 - e^{-i/I}) \tag{3-2}$$

For a large value of hydraulic gradient *i*, *dq/di* approaches a constant *K* that is hydraulic conductivity. Parameter *I* is called the threshold gradient in this study and refers to the intersection between the *i* axis and the linear part of the relationship (Figure 3-1). Integrating, and using *q*=0 at *i*=0, leads to

$$q = K[i - I(1 - e^{-i/I})] \tag{3-3}$$

Eq. (3-3) involves two parameters *K* and *I*. The equation of Swartzendruber (1961) has been evaluated with a number of data sets collected under saturated flow conditions and satisfactory agreements have been generally obtained (Swartzendruber, 1961; Blecker, 1970). However, it was found that Eq. (3-3) cannot capture the full range of non-Darcian flow behavior in clay media especially under unsaturated conditions (Liu and Birkholzer, 2013).

Another commonly used flux-gradient relationship for clay is given as (e.g., Bear, 1979):

$$q = 0 \text{ for } i \le I \tag{3-4a}$$

$$q = K(i - I) \text{ for } i \ge I \tag{3-4b}$$

Similar to Eq. (3-3), the above equation involves only two parameters (*K* and *I*) and is mathematically simpler. It is obvious, however, from data available in the literature, that Eq. (3-4) cannot adequately capture non-Darcian flow behavior (or non-linear flux-gradient relationship) at low *i* values (e.g., Swartzendruber, 1961; Blecker, 1970). Therefore, Eq. (3-4) should be applied only when *i* is large. Also note that Eq. (3-4b) is a limiting case of Eq. (3-3) for $i/I \to \infty$.

In an effort to develop a general relationship between water flux and hydraulic gradient (that covers the full range of non-Darcian flow behavior under both saturated and unsaturated conditions), Liu and Birkholzer (2013) proposed to generalize Swartzendruber's (1961) relationship using

$$\frac{dq}{di} = K(1 - e^{-\left(\frac{i}{I^*}\right)^{\alpha}}) \tag{3-5}$$

where α is a positive constant, and I^* is a parameter related to α and I. For α=1, Eq. (3-5) is reduced to Eq. (3-2). For $\alpha \to \infty$, $\frac{dq}{di} \to 0$ when $\frac{i}{I^*} < 1$, and $\frac{dq}{di} \to K$ when $\frac{i}{I^*} > 1$. In this case, Eq. (3-5) essentially represents the flux-gradient behavior given in Eq. (3-4). Thus, with one more parameter (α), Eq. (3-5) can capture a relatively large range of non-Darcian flow behavior.

Integrating Eq. (3-5) with the condition of q=0 at i=0 yields

$$q = K[i - \frac{I}{\gamma(\frac{1}{\alpha})}\gamma(\frac{1}{\alpha}, \left(\frac{i}{I^*}\right)^{\alpha})] \tag{3-6}$$

where

$$I = \frac{I^*}{\alpha}\gamma\left(\frac{1}{\alpha}\right) \tag{3-7a}$$

and γ refers to Gamma functions

$$\gamma(a,x) = \int_0^x t^{a-1}e^{-t}dt \tag{3-7b}$$

$$\gamma(a) = \int_0^\infty t^{a-1}e^{-t}dt \tag{3-7c}$$

Note that the physical meaning of parameter α is not fully understood yet; it may be associated with the pore-size distribution.

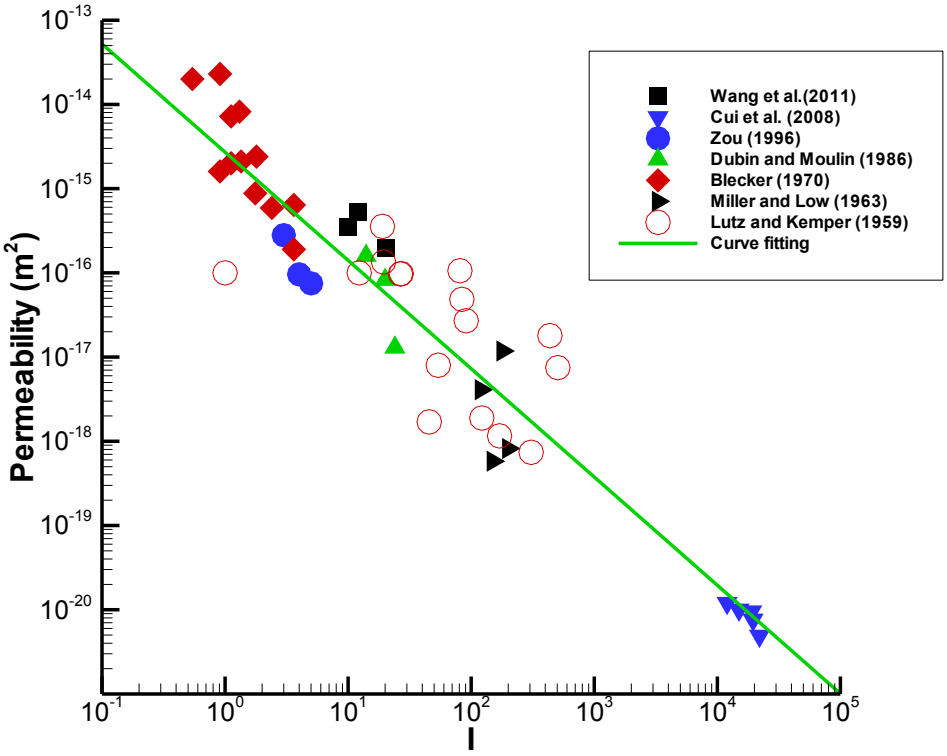

Figure 3-2. Correlation between permeability and threshold hydraulic gradient (Liu and Birkholzer, 2013).

For a clay material, the degree of solid-water interaction and non-Darcian flow behavior can be characterized by permeability (k) (or pore size) and threshold gradient (I), respectively. Thus, Liu and Birkholzer (2013), as shown in Figure 3-2, present an empirical correlation between K and I based on data sets from a number of researchers (Lutz and Kemper, 1959; Miller and Low, 1963; Blecker, 1970; Dubin and Moulin, 1986; Zou, 1996; Cui et al., 2008; Wang et al., 2011). These data sets can be reasonably fitted by a relationship between I and permeability k (m^2)

$$I = Ak^B \tag{3-8}$$

with $A = 4.0 \times 10^{-12}$ and $B = -0.78$. This finding is very encouraging considering that the data sets were collected for different kinds of clay media and low-permeability materials and by different researchers. This may imply the existence of a universal relationship between I and permeability, although some degree of fluctuation exists in Figure 3-2. Similar power-law relationships have also been reported in the literature of petroleum engineering (e.g., Zeng et al., 2010). Note that for unsaturated flow, k in Eq. (3-8) is replaced by relative permeability multiplied by permeability (Liu and Birkholzer, 2013).

3.3 A Demonstration of Impact of Non-Darcian Flow on Performance of a Clay Repository

As previously indicated, one major concern for a clay repository is that the hydromechanical perturbation caused by underground excavations during the construction stage could alter the properties of geological barriers compromising the safety performance of the repository system. The perturbation generally results in the excavation damaged zone (EDZ) around the repository tunnels and access shaft, because of a redistribution of *in situ* stresses and rearrangement of rock structures (Tsang et al., 2012). The higher concentration of macro- and microfractures in the EDZ increases the permeability by one or more orders of magnitude. Thus, the EDZ could act as a preferential flow path for advective transport. This is a very unfavorable condition because it can speed up radionuclide transport toward the biosphere. On the other hand, if water velocity in the EDZ is small, diffusion could be the dominant mechanism for radionuclide transport. In this case, the impact of the EDZ on radionuclide transport is minimal. Therefore, the relative importance of advection versus diffusion in the EDZ is a key issue for assessing the performance of a clay repository.

Recently, Bianchi et al. (2013) conducted a comprehensive modeling study on the relative importance of advection versus diffusion within the EDZ. They developed a two-dimensional model of a generic repository including a single horizontal tunnel for waste emplacement, a vertical shaft, and a vertical cross section of the host-rock formation. The longitudinal axis of the horizontal tunnel, which has a total length L equal to 600 m, is located at z = – 50 m (Figure 3-3). The length of the model domain in the x direction is 2000 m, such that boundary conditions imposed at the left and right boundaries are sufficiently distant from the tunnel and the shaft. The total thickness t_{HR} of the host rock is 100 m, while the vertical extension of the shaft (h_S) equals 50 m, from the end of the horizontal tunnel to the top boundary of the host formation. For their base case scenario, they assumed a vertical hydraulic gradient, determined by the difference in hydraulic head between the values imposed at upper and lower boundaries of the flow model, equal to 1 m/m. This value is consistent with the hydraulic conditions of the Opalinus Clay at the Mont Terri site, Switzerland (Bianchi et al., 2013). The values of the hydrogeological parameters assigned to the host rock and the repository components were also chosen to be realistic with respect to values from several sources (Table 3-1).

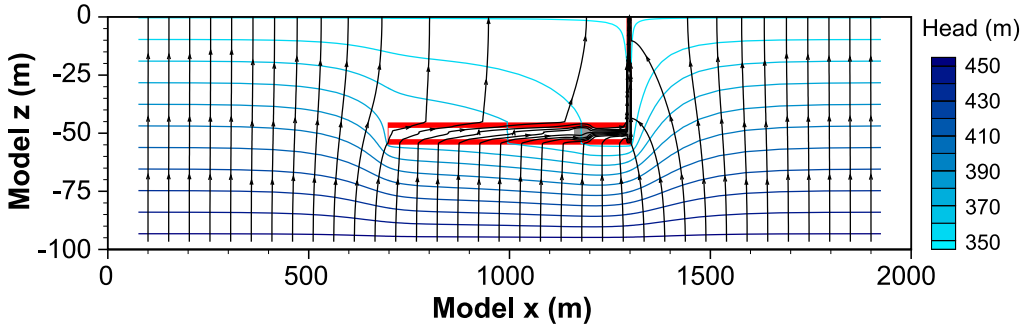

Figure 3-3. Flow pattern for a two-dimensional generic clay repository; red = EDZ. (Bianchi et al., 2013).

Table 3-1. Parameter Value for the Generic Clay Repository (Bianchi et al., 2013).

Parameter	Value
Vertical thickness of the host rock formation	100 m
Total length of the repository in the x direction	600 m
Repository tunnel diameter	4.5 m
Thickness of the EDZ in the tunnel	2.4 m
Initial hydraulic gradient in the z direction	1 m/m
Host rock permeability	5E-20 m^2
Diffusion coefficient for EDZ fractures	1.08E-9 m^2/s
Fracture porosity within the EDZ	0.01

The base-case simulation results of Bianchi et al. (2013) are demonstrated in Figure 3-3. The stream lines, shown in black, are generally vertical except within the EDZ surrounding the tunnel, and the water potential lines, shown in blue (each of which has constant water head [potential]), are generally in the horizontal direction. The simulations did not consider the non-Darcian flow behavior. Bianchi et al. (2013) found that for a given ambient hydraulic gradient, the upward water flow below the tunnel is intercepted by the high-permeability EDZ and advection indeed becomes important within the EDZ. They also found that the advection within the EDZ is limited by the amount of water flowing into it from the surrounding host rock. This is expected because when there is no water flowing into the EDZ, water velocity within the EDZ would be zero, even through the EDZ permeability is high.

In this study, we further investigated the relative importance of advection versus diffusion within the EDZ by incorporating the non-Darcian flow behavior. The model setup and parameter values in Bianchi et al. (2013) are employed herein. To simplify the analysis procedure, we assume that the EDZ permeability is infinite and the permeability of backfills in the tunnel is zero. Obviously, these assumptions generally lead to overestimation of the relative importance of advection within the EDZ. In this case, the EDZ has the same pressure head as the upper boundary in Figure 3-3, because the EDZ is in equilibrium with the upper boundary. The simulation results from Bianchi et al. (2013) indicate that under steady state conditions, the hydraulic gradient in the zone below the tunnel is very close to the uniform distribution. The same distribution is assumed here. With these assumptions and approximations, the hydraulic behavior of the EDZ can be easily determined without using numerical modeling. The hydraulic gradient below the tunnel will be twice as large as the ambient condition (or i = 2 m/m). The EDZ intercepts all the upward flow from the region below the tunnel. The water flow rate (and velocity) will be linear along the x axis with zero value at the left end and the maximum value at the right end (Figure 3-3).

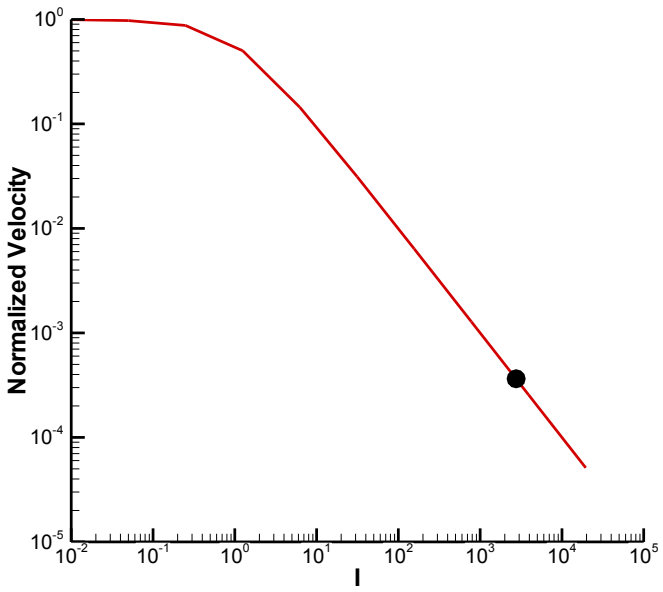

Figure 3-4. The normalized pore velocity as a function of threshold gradient *I*. The normalized velocity refers to the ratio of the maximum pore velocity within the EDZ to that in the Darcian-flow case.

The water flux into the EDZ from the lower portion of the clay formation in Figure 3-3 is estimated with Eq. (3-3) (for simplicity) and for i = 2 m/m. Based on the mass balance, the maximum (horizontal) water flow rate within the EDZ is equal to the calculated water flux, multiplied by the length of the tunnel and by the upper diameter of the EDZ. Then, the maximum pore velocity within the EDZ is determined with the flow rate, its cross-sectional area, and fracture porosity. Figure 3-4 shows the normalized pore velocity as a function of threshold gradient *I*. The normalized velocity there refers to the ratio of the maximum pore velocity within the EDZ to that for Darcian flow (2.69E-16 m/s). The filled circle in Figure 3-4 corresponds to the threshold hydraulic gradient I = 2755 m/m calculated from Eq. (3-8) using permeability k = 5E-20 m^2 (Table 3-1). Obviously, the non-Darcian flow has a significant impact on the water velocity. For the problem under consideration with I = 2755 m/m, the water velocity corresponding to non-Darcian flow is more than three orders of magnitude smaller than that for the Darcian flow (Figure 3-4).

The relative importance of the advection within EDZ can be evaluated with the Peclet number, Pe (Bianchi et al., 2013):

$$Pe = \frac{vL}{D} \tag{3-9}$$

where v (m/s) is the maximum pore velocity, L = 600 m is the length of the tunnel, and D (m^2/s) is the effective diffusion coefficient within fractures (Table 3-1). Note that with D here, unlike in porous media, we do not need to consider the tortuosity factor because transport paths in fractures are close to straight lines. In general, Pe represents the ratio of the time for diffusion (L^2/D) to the time for advection (L/v). For porous media, Pe < 1 is considered to correspond to the solute-transport regime with dominant diffusion. This criterion, however, is too strict for our study because the matrix diffusion process can significantly enhance the role of the diffusion process in fractured rock (Liu et al., 2007), but is not considered in the expression for Pe. Nevertheless, the calculated Pe values for the problem given in Figure 3-3 are 0.6 in the non-Darcian flow case and 1666.7 in the Darcian flow case. It is obvious that solute transport within the EZD, as a result of non-Darcian flow behavior, is diffusion-dominated, even though the EDZ permeability is assumed to be infinite. In other words, advection is not the dominant

transport mechanism within the EDZ because the water flow rate into the EDZ is essentially eliminated by the non-Darcian flow behavior in the shale formation. Note that our conclusion holds only under conditions without intersections between the EDZ and the conductive geological structures that connect the high-permeability formations surrounding the host rock formation.

The non-Darcian flow behavior discussed here is consistent with the often observed pressure-seal effects of shale formations. It is well known that a shale formation is capable of confining anomalous pressure over geologic time. Based on his analyses of pressure propagations, Deming (1994) concluded that the permeability needed for a geologic unit to act as a pressure seal over a time span of about one million years is in the range of 10^{-21} to 10^{-23} m^2, a range generally lower than most measurements of shale permeability. Note that the use of lower permeability values than actual ones in Deming (1994) is essentially equivalent to the consideration of non-Darcian flow behavior when the hydraulic gradient is less than the threshold gradient (Figure 3-1). The dominant mechanism for the anomalous pressure in shale formations has been an issue of debate in the literature. To the best of our knowledge, our work is the first to propose the non-Darcian flow as the dominant mechanism. The osmotic pressure within shale formations has also been proposed as a major mechanism (e.g., Tremosa et al., 2012). It may contribute to the persistence of observed overpressures, but cannot explain the frequently observed pressures that are lower than hydrostatic ones in shale formations.

3.4 Influence of Non-Darcian Flow on Observed Relative Permeability

Unsaturated properties for clay, including relative permeability k_r, are necessary inputs to modeling the unsaturated flow process. (Note that for simplicity, near-field unsaturated water flow is not considered in Section 3.3.) In general, the relative permeability can be related to water saturation by (van Genuchten, 1980):

$$k_r = S_e^{1/2}\left\{\left[1-\left(1-S_e{}^{1/m}\right)^m\right]\right\}^2 \tag{3-10a}$$

where m is a parameter related to pore size distribution and S_e is the effective saturation defined by

$$S_e = \frac{S-S_r}{1-S_r} \tag{3-10b}$$

where S and S_r are water saturation and residual saturation, respectively.

Since parameter m can be determined from the relatively easily measured water retention curve, Eq. (3-10) provides an efficient way to estimate relative permeability. The measurements of relative permeability are difficult and take a long time. However, the validity of the van Genuchten (1980) relationship, as an empirical one, is an open question for the shale rock because there are very rare studies on the comparison between the relationship and measured relative-permeability data for the rock. Thus, laboratory measurements of clay/shale relative-permeability values are needed to verify constitutive models and/or serve as inputs to modeling studies. The major purpose of this section is to demonstrate that "measured" values for relative permeability are not true medium properties, but strongly depend on test conditions, as a result of non-Darcian flow behavior. By "true" relative permeability, we mean the relative permeability associated with the linear regime for the curve in Figure 3-1.

To measure the relative permeability, the hydraulic gradient i is generally fixed, and then water flux q is measured under steady-state condition. In this case, the "measured" relative permeability k_{rM} can be calculated as

$$k_{rM} = \frac{q/i}{K} \tag{3-11}$$

For simplicity, we use Eq. (3-3) to describe the non-Darcian flow behavior. Note that under unsaturated conditions, conductivity K in Eq. (3-3) needs to be replaced by unsaturated conductivity Kk_r. In this case, Eq. (3-11) becomes

$$k_{rM} = (1 - \frac{1-e^{-\frac{i}{I_{unsat}}}}{\frac{i}{I_{unsat}}})k_r \quad (3\text{-}12)$$

Herein, we denote I and I_{unsat} as the threshold hydraulic gradient under saturated and unsaturated conditions, respectively. To calculate I_{unsat} with Eq. (3-8), the permeability (k) there needs to be replaced by unsaturated permeability kk_r (Liu and Birkholzer, 2013). As previously indicated, water flow under unsaturated conditions generally exhibits stronger non-Darcian flow behavior than that under saturated conditions, because the former corresponds to smaller sizes of pores occupied by water.

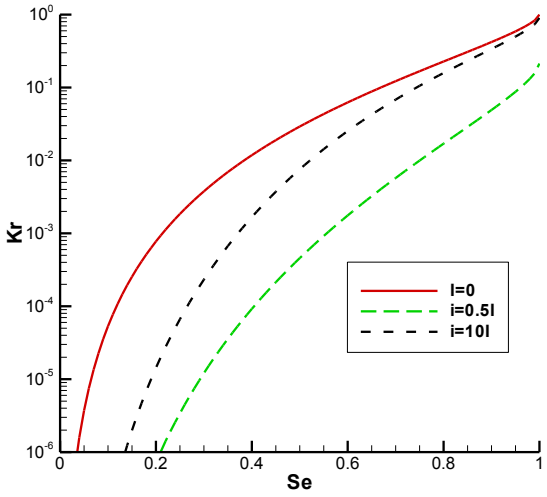

Figure 3-5. "Measured" relative permeability curves under different hydraulic gradient, as a function of the effective saturation. Note that I = 0 corresponds to the "true" relative permeability curve calculated with Eq. (3-10).

For demonstration purposes, and for the lack of alternatives, we assume that k_r in Eq. (3-12) can be represented by Eq. (3-10). When hydraulic gradient i in a test is given, k_{rM} can be calculated from Eq. (3-12) with I_{unsat} and k_r obtained from Eqs. (3-8) and (3-10), respectively. The value for m is assigned to be 0.6 (Zheng et al., 2012). Figure 3-5 shows the calculated k_{rM} curves as a function of the effective saturation. For each curve, the hydraulic gradient i is fixed. The threshold gradient I is determined from Eq. (3-8) with k = 5E-20 m^2 (Section 3.3). Note that I = 0 corresponds to the "true" relative permeability curve calculated with Eq. (3-10).

Figure 3-5 shows that a measured relative permeability, for a given saturation, is significantly smaller than the "true" value, especially for the low saturations under which non-Darcian flow behavior becomes relatively strong. The measured curve is a function of the hydraulic gradient used in the test. A larger gradient gives results closer to the "true" values, which is expected from Figure 3-1. If relatively small hydraulic gradients are used in tests, the measured relative permeability can be smaller than one under the saturated condition, because permeability k measurements are not made in the linear regime of the relationship between water flux and hydraulic gradient (Figure 3-1). The differences between "measured" curves and the "true" curve would be even more dramatic if Eq. (3-6) with α values larger than one were used for describing the non-Darcian flow behavior, because it gives much smaller values for dq/di when the hydraulic gradient is smaller than the corresponding threshold gradient (Eq. (3-5)). Nevertheless,

Figure 3-5 clearly indicates that without considering the non-Darcian flow behavior, the "measured" values for relative permeability involve large errors.

Our finding seems to be consistent with the relative permeability measurements of rock matrix from the unsaturated zone of Yucca Mountain (BSC, 2004). Those measurements, for a given saturation, are dramatically smaller than what are predicted from the van Genuchten relationship (Eq. 3-10) for samples with (absolute) permeability values below 10^{-18} m^2. The differences can be explained with the non-Darcian flow behavior in low-permeability media, as discussed above.

There are several ways to recover the "true" relative permeability curve from raw measurements by incorporating the non-Darcian flow behavior. The ideal one would be to use large enough hydraulic gradients such that throughout the tests, the relationship between water flux and the gradient is in the linear regime (Figure 3-1). However, this may not be feasible in practice because the threshold gradient can be huge for low saturations. When the relationship between permeability and the threshold gradient (e.g., Eq. (3-8)) is known with confidence, the only unknown in Eq. (3-12) is k_r for a given measurement k_{rm}. In this case, k_r can be estimated by solving Eqs. (3-8) (generalized for unsaturated conditions) and (3-12). If the required relationship between permeability and the threshold gradient is not known for a specific rock type, measurements for relative permeability with different hydraulic gradients, such as those shown in Figure 3-5, need to be made. To recover the true curve, we can simultaneously fit the measured curves using Eqs. (3-8), (3-10) and (3-12) with parameters A, B, and m being treated as fitting parameters. The advantage of this approach is that both the true relative permeability curve and the relationship between permeability and threshold gradient are simultaneously determined from measurements.

3.5 A Hypothesis Regarding the Temperature Dependence of the Threshold Hydraulic Gradient

Performance assessment of a clay repository requires consideration of the impact of temperature on non-Darcian flow behavior, because such a repository is subject to temperature evolution in the near field as a result of heat generated by nuclear waste. This section presents a hypothesis regarding the temperature dependence of the threshold hydraulic gradient.

Studies of temperature impact on non-Darcian flow behavior are rare in the literature. To the best of our knowledge, the only study related to temperature impact on non-Darcian water flow is Miller and Low (1963). They experimentally found that the critical hydraulic gradient (below which water is immobile) decreases with increasing temperature. They argued that this is because increased temperature may weaken the bounding between water molecules and the clay surface. Recently, Zeng et al. (2010) also reported an experimental investigation into temperature impact on oil flow processes in initially water-saturated low-permeability sandstone samples. They performed tests at two temperatures (70°C and 90°C) and found that observed threshold pressure gradient, in terms of oil mobility (or the ratio of permeability to temperature-dependent oil viscosity), does not depend on temperature. This is a potentially important result. Unfortunately, there are no data from a large range of temperatures to further verify their finding. However, their results are consistent with the argument of Miller and Low (1963) in that the weakened liquid-solid interaction should correspond to a low effective viscosity. Thus, as a first step, we hypothesize that the finding of Zeng et al. (2010) can be applied to water flow in clay materials.

Based on our hypothesis, Eq. (3-8) becomes

$$I = Ak^B \left(\frac{\mu_{ref}}{\mu}\right)^B \tag{3-13}$$

with $A = 4.0 \times 10^{-12}$ and $B = -0.78$. In the above equation, μ and μ_{ref} are water viscosities, respectively, at the current temperature and the reference temperature at which the data used to develop Eq. (3-8) were collected. Here the reference temperature is given as 25°C.

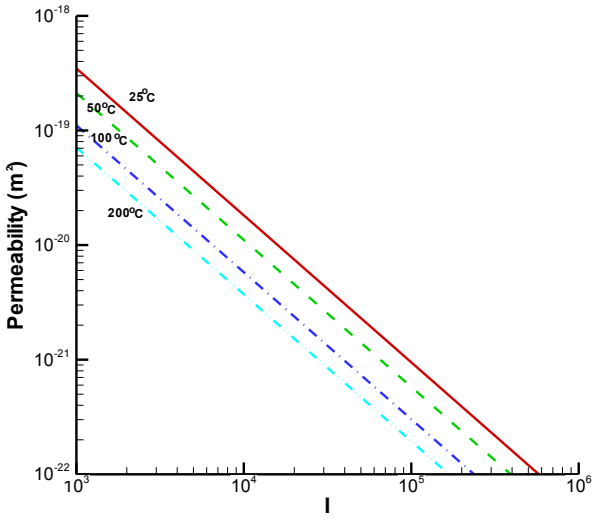

Figure 3-6. The temperature dependence of the relationship between threshold hydraulic gradient and permeability.

Figure 3-6 shows the results calculated from Eq. (3-13) for several temperatures from 25°C to 200°C that cover the temperature range of interest to performance assessment of a clay repository. (The line for 25°C is identical to that in Figure 3-2.) Viscosity values for different temperatures are taken from Weast et al. (1989) and Kestin et al. (1978). The threshold hydraulic gradient decreases with temperature, but the change is less than one order of magnitude for a given permeability (Figure 3-6). Eq. (3-13) allows for incorporating the temperature impact in modeling non-Darcian flow in clay or shale rocks, but it should be used with caution, especially when modeling results are sensitive to the temperature impact. More studies, both theoretical and experimental, are needed to develop more rigorous approaches for dealing with this temperature dependence.

3.6 An Approximate Formulation of Water Flux in Anisotropic Media

In many studies, including modeling of flow and transport in a clay repository, we need to investigate multidimensional water-flow processes. However, most previous studies on the non-Darcian flow are for one-dimensional cases. Recently, Liu and Birkholzer (2013) extended Eq. (3-6) to three-dimensional, homogeneous and isotropic clay media:

$$\boldsymbol{q} = -K[i - \frac{I}{\gamma(\frac{1}{\alpha})}\gamma(\frac{1}{\alpha}, \left(\frac{i}{I*}\right)^{\alpha})]\boldsymbol{n}_i \tag{3-14}$$

where $\boldsymbol{q}$ (m/s) and $\boldsymbol{n}_i$ (-) are water flux vector and unit vector for hydraulic gradient, respectively. The relationship between I and I^* is given by Eq. (3-7a). When the threshold gradient I approaches zero, Eq. (3-14) is reduced to the commonly used form of Darcy's law. It should be emphasized that Eq. (3-14) is

an empirical relationship developed from one dimensional test results. It is logical to directly extend Eq. (3-6) to Eq. (3-14) for homogeneous and isotropic cases because both equations are consistent with the one-dimensional-test condition that flux and negative hydraulic gradient are along the same direction.

Shale formations are generally anisotropic, as a result of bedding structure. To model water flow in these formations, we need a formulation for water flux in anisotropic media. However, because of the non-linear feature of the non-Darcian flow, it is not a trivial task to theoretically relate the flux-gradient relationship between different dimensions and/or between isotropic and anisotropic media. Thus, in this study, we present an approximate formulation of water flux in an anisotropic medium. For simplicity, we choose the spatial coordinate axes to be in the principal directions of the anisotropic medium (Bear, 1979) such that one axis is perpendicular to the bedding plane. Then, we propose the water-flux formulation for anisotropic media by extending Eq. (14):

$$\boldsymbol{q} = -\boldsymbol{K}[i - \frac{I}{\gamma(\frac{1}{\alpha})}\gamma(\frac{1}{\alpha}, \left(\frac{i}{I*}\right)^{\alpha})]\boldsymbol{n}_i \tag{3-15a}$$

$$I = \frac{\sqrt{(I_x i_x)^2 + (I_y i_y)^2 + (I_z i_z)^2}}{\sqrt{(i_x)^2 + (i_y)^2 + (i_z)^2}} \tag{3-15b}$$

where $\boldsymbol{K}$ is the conductivity tensor, and subscripts x, y and z refer to components along three coordinate directions. Specifically, I_j (j=x, y, z) is the measured threshold hydraulic gradient in the j-direction from one-dimensional experiments. Because of the way the coordinate system was chosen, there are no cross terms in the conductivity tensor. It is also easy to show that the relation among the magnitude of conductivity, conductivity components, and hydraulic-gradient components has the same mathematical form as Eq. (3-15b).

The reasonableness of the approximation (Eq. (3-15)) can be demonstrated by its consistency with known results. For one-dimensional flow along the bedding direction (e.g., the x direction), Eq. (3-15) is reduced to Eq. (3-6) with $I = I_x$. Similarly, if the z direction is perpendicular to the bedding plane, we can also get the expected result, $I = I_z$, for one-dimensional flow along the z direction. For isotropic cases (or $I_x = I_y = I_z$), we can recover Eq. (3-14) from Eq. (3-15). Thus, Eq. (3-15) gives an approximate, yet practically reasonable way to model non-Darcian water flow in the bedding shale formations, while the exact formulation for water flux in anisotropic media is difficult to obtain.

3.7 Concluding Remarks

This chapter presents new results of a continuing effort to develop a general modeling framework for non-Darcian water flow in low-permeability media. Specifically, we devote this communication to addressing several key issues related to geological disposal of high-level nuclear waste in shale formations.

One of the most important technical questions for the performance of a shale/clay repository is the relative importance of advection versus diffusion in the damage zone near underground tunnels/drifts. We demonstrate that under normal conditions (under which there are no intersections between tunnels/drifts and conductive geological structures, such as faults), water flow velocity in the damaged zone, as a result of non-Darcian flow behavior, is extremely small such that solute transport is dominated by diffusion, rather than advection. Our findings are also consistent with the often observed existence of persistent abnormal pressures in shale formations.

Unsaturated flow takes place in both the engineered barrier system and the host rock of a shale/clay repository. Relative permeability is the key parameter for modeling the unsaturated flow process. We

show that without incorporating non-Darcian flow behavior, significant errors can occur in the determination of relative-permeability values from traditional measurement methods. How to recover the true relative permeability values from the measurements is also discussed.

A geological repository is subject to temperature evolution in the near field as a result of heat generated by nuclear waste. Thus, it is important to incorporate the impact of temperature on non-Darcian flow behavior in order to more accurately assess repository performance. As a first step toward to resolving this issue, we propose a hypothesis to consider the temperature impact based on limited test results from the petroleum literature. The hypothesis states that the threshold hydraulic gradient is a function of temperature-dependent mobility only.

Shale formations consist of bedding layers and are therefore generally anisotropic. To consider the bedding effects, we also propose an empirical relationship between water flux and hydraulic gradient for non-Darcian water flow in anisotropic media. The relationship is consistent with the known relationships for one-dimensional and three-dimensional isotropic cases.

3.8 References

Bear, J., 1979. Hydraulics of Groundwater. McGraw-Hill, Inc., New York.

Blecker, R.F., 1970. Saturated flow of water through clay loam subsoil material of the Brolliat and Springerville soil series. Master Thesis, The University of Arizona.

Bianchi, M., Liu, H.-H., Birkholzer, J., 2013. Radionuclide transport behavior in a generic radioactive waste repository, *Groundwater* (submitted).

Bechtel SAIC Company (BSC), 2004. Analysis of hydrologic properties data, Report ANL-NBS-HS-000042.

Cui, Y.J., Tang, A.M., Loiseau, C., Delage P., 2008. Determining the unsaturated hydraulic conductivity of a compacted sand-bentonite mixture under constant-volume and free-swell conditions, *Physics and Chemistry of the Earth,* 33, S462-S471.

Deming, D., 1994. Factors necessary to define a pressure seal, *AAPG Bulletin,* 78(6), 1005-1009.

Dubin, B., Moulin, G., 1986. Influences of critical gradient on the consolidation of clay. In Consolidation of soils, testing and evaluation (eds Young and Townsend), ASTM STP 892, pp. 354-377. West Conshohocken, PA.

Hansbo, S., 1960. Consolidation of clay, with special reference to influence of vertical sand drains. Swed. Geotech. Inst. Proc. 18, Stockholm.

Hansbo, S., 2001. Consolidation equation valid for both Darcian and non-Darcian flow, *Geotechnique*, 51(1), 51-54.

Kestin, J., Sokolov, M., Wakeham, W.A., 1978. Viscosity of liquid water in the range -8^{o}C to 150^{o}C, *J. Phys*, Chem. Ref. data, 7(3), 941-948.

Liu, H.H., Zhang, Y.Q., Zhou, Q., Molz, F.J., 2007. An interpretation of potential scale dependence of the effective matrix diffusion coefficient, *Journal of Contaminant Hydrology*, 90(1-2), 41-57.

Liu, H.H., Li, L. C., Birkholzer, J., 2012. Unsaturated properties for non-Darcian water flow in clay, *Journal of Hydrology*, 430-431, 173-178.

Liu, H.H., Birkholzer, J., 2013. On the relationship between water flux and hydraulic gradient for unsaturated and saturated clay, *Journal of Hydrology*, 476, 242-247.

Lutz, J.F., Kemper, W.D., 1959. Intrinsic permeability of clay as affected by clay-water interaction, *Soil Sci.*, 88: 83-90.

Miller, R.J., Low P.F., 1963. Threshold gradient for water flow in clay systems, *Soil. Sci. Soc. Am. Proc.*, 27(6), 605-609.

Tremosa, J., Gonçalvès, J., Matray, J.M., 2012. Natural conditions for more limited osmotic abnormal fluid pressures in sedimentary basins, *Water Resources Research*, 48, W04530, doi:10.1029/2011WR010914.

Tsang, C.F., Barnichon, J.D., Birkholzer, J., Li X.L, Liu, H.-H., Sillen, X., 2012. Coupled thermo-hydro-mechanical processes in the near field of a high-level radioactive waste repository in clay formations, *Int. J. Rock Mech. Min. Sci.,* 49: 31-44. DOI 10.1016/j.ijrmms.2011.09.015.

Swartzendruber, D., 1961. Modification of Darcy's law for the flow of water in soils, *Soil Science*, 93: 22-29.

Van Genuchten, M., 1980. A closed-form equation for predicting the hydraulic conductivity of unsaturated soil, *Soil. Sci. Soc. Am. J.*, 44(5), 892-898.

Wang, X.-W., Yang, Z.-M., Sun, Y.-P., Liu, X.-W., 2011. Experimental and theoretical investigation of nonlinear flow in low permeability reservoir, *Procedia Environmental Sciences*, 11, 1392-1399.

Weast, R.C., Astle, M.J., Beyer, W.H., 1989. CRC handbook of chemistry and physics (69th edition), CRC Press, Inc., Boca Raton, Florida.

Xu, S.L., Yue, X. A., Hou, J.R., 2007. Experimental investigation on flow characteristics of deionized water in microtubes, *Chinese Science Bulletin*, 52(6), 849-854.

Zeng, J.H., Cheng, S.W., Kong, X., Guo. K., Wang, H.Y., 2010. Non-Darcy flow in oil accumulation (oil displacing water) and relative permeability and oil saturation characteristics of low-permeability sandstones, *Pet. Sci.,* 7, 20-30.

Zheng, L., Li, L., Rutqvist, J., Liu, H., Birkholzer, J.T., 2012. Modeling Radionuclide Transport in Clays. Lawrence Berkeley National Laboratory. FCRD-URD-2012-000128.

Zou, Y., 1996. A non-linear permeability relation depending on the activation energy of pore liquid, *Geotechnique*, 46(4), 769-774.

This page left blank intentionally.

4 USING ENVIRONMENTAL TRACERS TO ESTIMATE FRACTURE NETWORK PROPERTIES: BEDRICHOV TUNNEL, CZECH REPUBLIC

4.1 Introduction

Environmental tracers are non-applied chemical species present in precipitation with known concentration histories and known decay and production rates in the subsurface. These tracers provide information on the transport characteristics of groundwater systems over a wide range of time scales. The primary goal of this study is to use environmental tracer data from the Bedrichov tunnel experiment to help characterize fracture transport characteristics. Cutting-edge transport theory and computational power are being used to incorporate environmental tracer information in estimating fracture network capabilities. The primary activities accomplish during FY-2013 include attending the DECOVALEX-2012 meetings in Leipzig Germany and Jeju Island Korea, and the development of lumped parameter for the simulation of environmental tracer concentrations discharging in the Bedrichov Tunnel.

Interpretation of environmental tracers has proven useful for the conceptualization and parameterization of fracture flow systems. Simplified analytic solutions to the 1-D advection-diffusion models have been used to estimate recharge and fracture spacing (Cook and Robinson, 2002), and 1-D numerical models have been used to show the effect of matrix diffusion on environmental tracer concentration and groundwater age distribution using parallel fracture networks (Cook et al., 2005). However, higher dimensional modeling and or more sophisticated fracture networks have not been used.

Fracture network transport of applied tracers is an area of active research (e.g. Painter and Cvetkovic, 2005; Painter et al., 2008a,b). However, these studies are concerned with the movement of applied tracers and/or released contamination. Applied tracers have a very limited time range of applicability and even the longest term tracer experiments would be on the order of 10's of years, while travel times in large fracture networks can be over 10^5 years. Making predictions of long term transport over the latter time scale will be highly uncertain using only observations on the former. Improving the interpretation of environmental tracers which can provide information on transport up to 10^8 years will clearly aid when making predictions on the at time scale.

Task C2 of the DECOVALEX workgroup is centered around a dataset of environmental tracers and discharge in Bedrichov Tunnel located in the Bohemian Massif of the Czech Republic. The tunnel is around 1 km in length with a max depth of 200m and cuts through fractured granite. The dataset includes stable isotopes of water, tritium, tritiogenic ^{3}He and other noble gases, and dissolved chlorofluorocarbons (CFCs) measured in fracture discharge. It leverages an existing data collection point for stable isotopes and tritium measured in precipitation near the study site. The goal of Task C2 is to model groundwater flow and transport of environmental tracers in the fractured system surrounding the Bedrichov Tunnel, and utilize this data to constraint fracture network parameters.
Methods:

In FY13 we developed lumped parameter models and numerical models that simulate tracer transport to the Bedrichov Tunnel. Existing lumped parameter conceptual models and a newly developed conceptual model which includes matrix diffusion were used to provide an initial first order interpretation of the tracer data. Subsequently 3-d models of groundwater flow and isotope tracer transport were developed using the PFLOTRAN flow and transport code. These models are simplified and will be used as the building blocks for more advanced simulation and interpretation in the future.

4.2 Lumped Parameter Models

The concentration of a tracer a sampling point is a function of the distribution of groundwater age ($g(\tau)$) given by the convolution integral:

$$C(t) = \int_0^\infty C_{in}(t-\tau)g(\tau)e^{-\lambda\tau}d\tau \quad (4\text{-}1)$$

where C_{in} is the input function for the tracer and λ is the decay constant for the tracer of interest. Age distributions have been developed for a variety of simple aquifer type and flow systems (e.g. Cook and Herczeg, 2000). The models used in this study include commonly used dispersion and exponential model as well as a newly developed model which includes matrix diffusion in fractured systems. For the exponential model:

$$g(\tau) = \frac{1}{\tau} * e^{-\frac{t-\tau}{\tau}} \quad (4\text{-}2)$$

and for the dispersion model:

$$g(\tau) = \left(\frac{4\pi(t-\tau)^3}{Pe\tau}\right)^{1/2} \exp\left(-1-\frac{t-\tau}{\tau}\right)^{2\tau Pe(t-\tau)} \quad (4\text{-}3)$$

where Pe is the peclet number for transport. In order to account for matrix diffusion we use the random walk in time method after (Painter et al., 2008a,b). Here the retarded travel time distribution is given by:

$$g(t_{tr}) = \int_0^\infty \int_0^\infty g_{ret}(t_{tr}-\tau|\beta)g_{\beta|\tau}(\beta|\tau)g(\tau)\,d\tau d\beta \quad (4\text{-}4)$$

where τ is the non-retarded advective travel time, β is the transport resistance parameter and t_{tr} is the total travel time include retention. The retention time distribution can be derived for a variety of processes including unlimited matrix diffusion which is given by (Painter et al., 2008a,b):

$$g_{ret} = H(t_{ret})\kappa\beta/2\sqrt{\pi t_{ret}}\exp(-\kappa^2\beta^2/4t_{ret}) \quad (4\text{-}5)$$

where:

$$\kappa = \theta_{im}\sqrt{DR_{im}} \quad (4\text{-}6)$$

is a function of the immobile porosity θ_{im}, effective diffusion coefficient and immobile retardation factor R_{im}. We incorporate matrix diffusion via the random walk in time methodology after Painter et al. (2008a) by sampling an advective travel from travel time distributions of a dispersive and exponential age distribution, then sample the resistance parameter given the travel time, then sample from the retention time distribution give the resistance parameter to calculate a total travel time. The total travel time distribution is then reconstructed from these samples.

Observation of isotopes at the Bedrichov tunnel were then used to constrain the mean age of the lumped parameter models. For a given conceptual model, lumped parameter models were run with different mean groundwater age (τ) and the resulting modeled isotope concentrations compared with observed concentrations.

4.3 Results

The main activities in this fiscal year were workshop attendance and model development. At this point only preliminary results for the lumped parameter and PFLOTRAN numerical modeling are available. More sophisticated forward modeling and parameter estimation will be included in future work.

Lumped Parameter Modeling:

Modeled stable δD composition in the Bedrichov tunnel at sampling point V6 for an exponential age distribution with mean ages of 1, 2.5, 5 and 10 years is show in Figure 4-1. The exponential model is incapable of fitting the observed data for any age distribution and shows a bias toward heavy isotopes. Models stable δD composition in the Bedrichov tunnel at sampling point V6 for a dispersion age distribution with mean ages of 1, 2.5, 5 and 10 years is shown in Figure 4-2. The dispersion model fits the observed data slightly better, but as in the case of the exponential model, the dispersion model produces consistently heavy isotopic signals for all ages modeled. A similar bias is modeled results was observed for all other sample locations. This bias is an effect of preferential seasonal recharge of winter snow melt. However, it can be noted that temporal variation in modeled isotopes essentially disappears for all mean ages over 5 years, thus the fact that the observed isotopic composition does vary indicates a short residence time of 5 years or less in Bedrichov tunnel waters. Future work will include developing a seasonally weighted input function that will allow a more quantitative comparison.

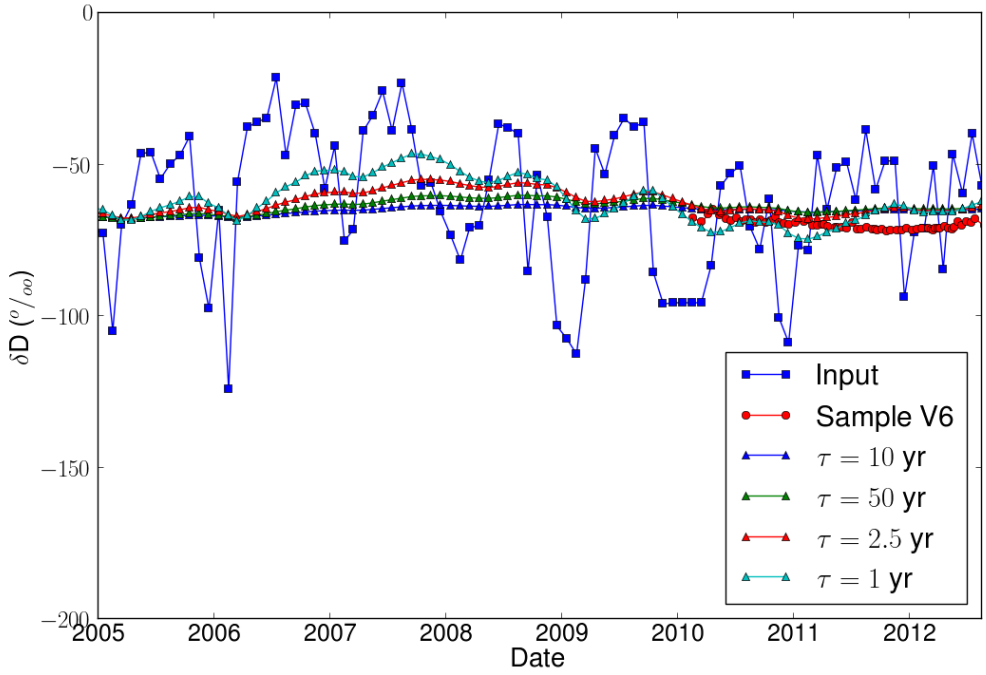

Figure 4-1. Measured and modeled stable isotope composition for the Bedrichov sample V6 using the exponential age distribution

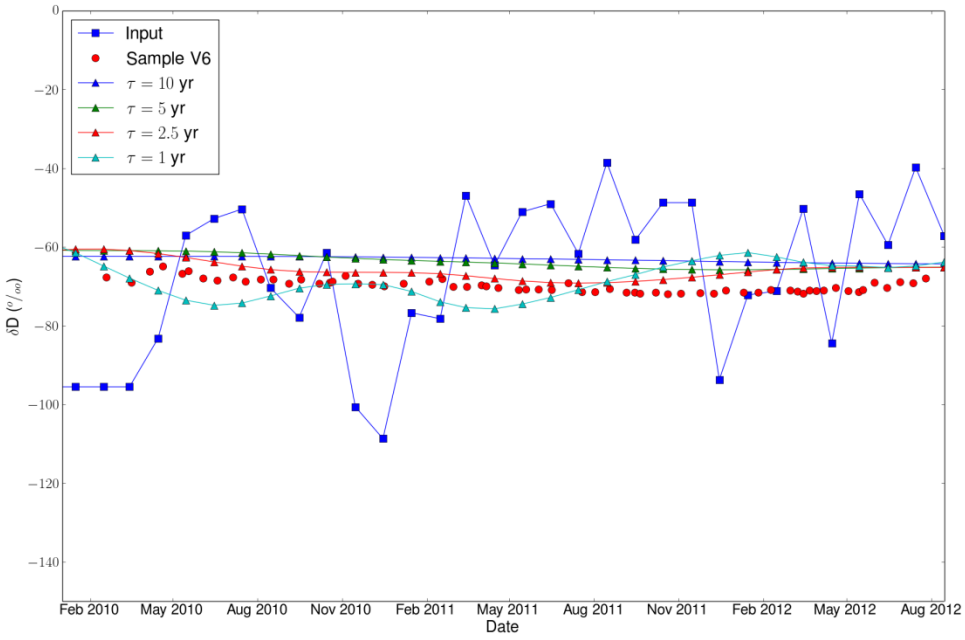

Figure 4-2. Measured and modeled stable isotope composition for the Bedrichov sample V6 using the dispersive age distribution

A tracer plot of tritium versus CFC-12 is shown in Figure 4-3. Tritium in Bedrichov precipitation was created using an inverse distance weighted average of surrounding records including Vienna, Prague, and Uhlirska. The expected concentration measured in 2012 for increasing mean age is plotted in the dashed red line. Black dots indicate 5 year intervals in mean age. From Figures 4-3 and 4-4 it is apparent that waters discharging the Bedrichov tunnel are generally less than 5 years in age. This is the case regardless of the age distribution chosen. Thus, we conclude that fluid flow in the Bedrichov fractures rapid and groundwater ages are less 5 years for almost all samples.

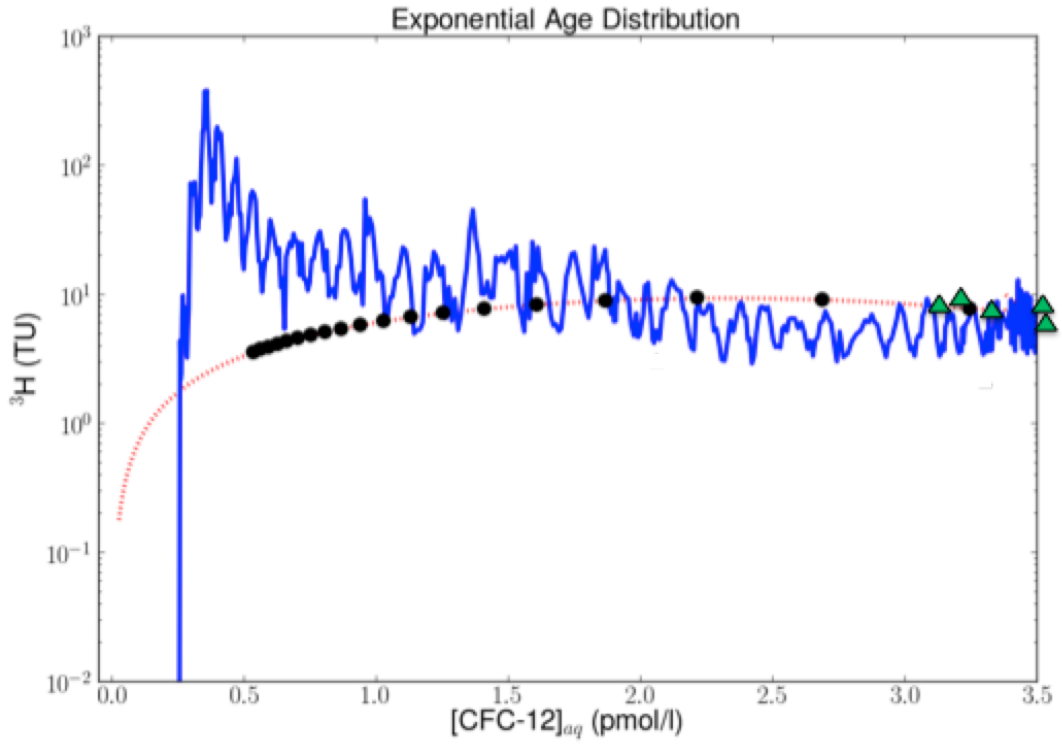

Figure 4-3. Tracer plot of ^{3}H vs CFC-12 for precipitation (blue line) at Bedrichov, measured samples (green triangles) and expected concentration for the year 2012 given an exponential age distribution as a function of increasing mean age. Black circles are the expected concentration for every 5 year interval of mean age

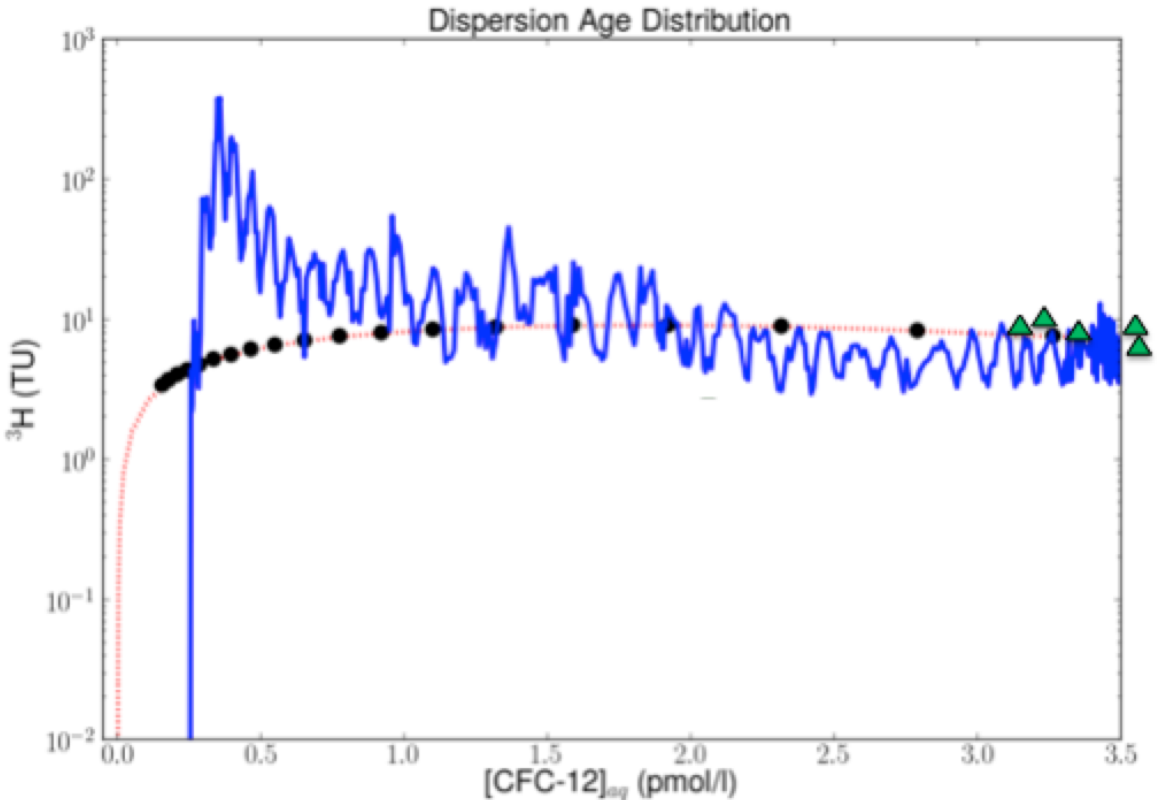

Figure 4-4. Tracer plot of ^{3}H vs CFC-12 for precipitation (blue line) at Bedrichov, measured samples (green triangles) and expected concentration for the year 2012 given a dispersion age distribution as a function of increasing mean age. Black circles are the expected concentration for every 5 year interval of mean age

Matrix Diffusion:

We explored the effect of matrix diffusion at the Bedrichov site using our random walk in time method. Figure 4-5 shows the expected travel times for dispersion only and for dispersion and retention assuming infinite matrix diffusion. Here we assume matrix diffusion parameters representative of the Bedrichov site, and assign a mean advective travel time was 2 years, matrix porosity of 1% and fracture diameter of 0.2 mm. We observe no difference in the age distribution in Figure 4-5 and find that the mean total travel time including retention is indistinguishable from the mean travel time considering advection alone. Figure 4-6 shows the advective and total travel time distributions for a system with a mean advective travel time of 100 years, 10% matrix porosity and fracture width of 0.2 mm. There is a clear effect of matrix diffusion in Figure 1-6 and the mean total travel time of 5000 years is significantly different than that of purely advection alone.

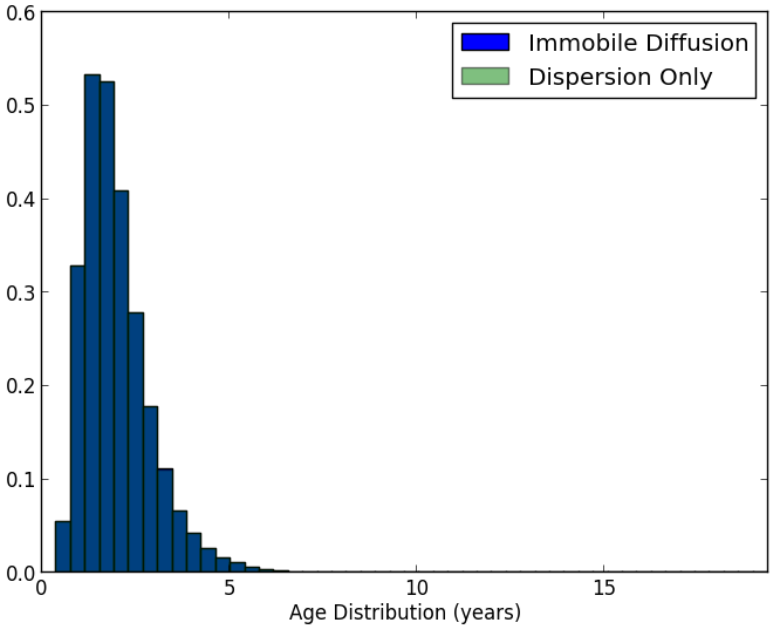

Figure 4-5. Expected age distributions for a dispersion model only and a dispersion model which includes retention time from infinite matrix diffusion for a mean advective travel time of 2 years, a matrix porosity of 1% and a fracture diameter of 0.2mm

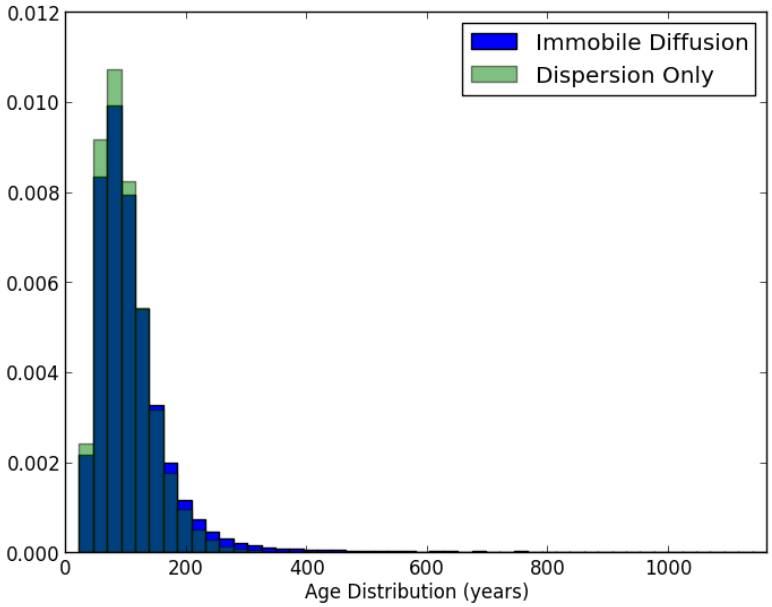

Figure 4-6. Expected age distributions for a dispersion model only and a dispersion model which includes retention time from infinite matrix diffusion for a mean advective travel time of 100 years, a matrix porosity of 10% and a fracture diameter of 0.2mm

4.4 Conclusions

We have developed lumped parameter models of stable isotope, tritium and CFC-12 transport at the Bedrichov Tunnel site and compared modeled results to measured data. To account for matrix diffusion in the fractured system at Bedrichov, the effect of matrix diffusion on travel must be investigated. Here we account for the retention time from matrix diffusion using a random walk in time methodology. Our lumped parameter models consistently predict heavier isotopic values that those observed at the site, indicating preferential recharge of winter precipitation. The variability in isotopic composition of discharge observed at the site is indicative of short travel times – as modeled isotopic composition with mean travel times over 5 years tend to show no temporal variation. These results are consistent with those from CFC and ^{3}H which indicate travel times of less than 5 years in the Bedrichov tunnel. Using parameters indicative of the Bedrichov Tunnel we show that matrix diffusion is probably not a major process at this site given the very fast transit times. However, this process will have very large effect with longer residence times.

4.5 References

Cook, P.G., A. L. Herczeg (2000), *Environmental Tracers in Subsurface Hydrology*, Kluwer, Boston, 529p.

Cook, P. G., A. J. Love, N. I. Robinson, and C. T. Simmons (2005), Groundwater ages in fractured rock aquifers, *J. Hydrology*, 308(1-4), 284-301.

Cook, P. G., and N. I. Robinson (2002), Estimating groundwater recharge in fractured rock from environmental ^{3}H and ^{36}Cl; Clare Valley, South Australia, *Water Resources Research* 10.1029/2001WR000772.

Painter, S., and V. Cvetkovic (2005), Upscaling discrete fracture network simulations: An alternative to continuum transport model, *Water Resour. Res.* 41, W02002.

Painter S., Cvetkovic V., Mancillas J., and Pensado O., (2008a), Time domain particle tracking methods for simulating transport with retention and first-order transformation, Water Resources Research 44, W01406, doi:10.1029/2007WR005944.

Painter, S., V. Cvetkovic, and O. Pensado (2008b), Time-domain random-walk algorithms for simulating radionuclide transport in fractured porous rock, *Nuclear technology*, 163 (1), 129-136.

5 KURT SITE CHARACTERIZATION DATA - FRACTURE AND HYDROLOGIC DATA FROM DEEP BOREHOLES IN KURT SITE

5.1 Introduction

Korea Atomic Energy Research Institute (KAERI) was engaged, on behalf of the Sandia National Laboratories (SNL), to conduct three tasks including sharing KURT site characterization data, technique development for in-situ borehole characterization and streaming potential (SP) testing, to support the study of high-level nuclear waste disposal in crystalline geologic media. This section documents a deliverable for the task of sharing KURT site characterization data. In this task, KAERI provides SNL with fracture and hydrologic data from the deep borehole DB-1 (500m), DB-2 (1,000m), YS-1 (500m) and YS-6 (500m) and hydrochemical data from the deep borehole DB-1 and YS-1 around the KURT (Table 5-1).

5.2 KURT (KAERI Underground Research Tunnel)

History and current status of KURT:

KURT is a generic underground research laboratory, and it intends to obtain information on the geological environment and behavior and performance of engineered barriers under repository conditions. For an investigation into the feasibility, stability, and safety of the proposed HLW disposal concept in Korea, it was necessary to experimentally investigate the disposal system in underground conditions. The Planning Committee for the Korean Nuclear Energy R&D Program decided to construct a small-scale underground research laboratory at KAERI to test the disposal concept in 2003. Site characterization and a detailed design for the construction of KURT were completed in 2004. In November 2004, KAERI received a construction license from the municipal local governments of Daejeon city and Yuseong district, as well as from the Ministry of Science and Technology (MOST). Construction started in March 2005 and was completed in November 2006.

KURT has a total length of 255 m with a 180 m long access tunnel and two research modules with a total length of 75 m. The maximum depth of the tunnel is 90-100 m from the peak of a mountain that locates over the site. The horseshoe-shaped tunnel section is 6 m wide and 6 m high (Figure 5-1). The host rock is granite, which is one of the potential host rock types for an HLW disposal repository in Korea. The utilization of radioactive material in KURT is not allowed.

The design requirements for KURT were as follows (Cho et al., 2008):

- The long-term stability of the tunnel should be ensured with minimum rock support.
- Damage to the host rock from an excavation should be minimized.
- The access tunnel should be linear to obtain the maximum overburden of the research modules with the minimum length of the access tunnel.
- The research modules should be located at the rock mass with good quality.
- The research modules should be located in a fresh bed rock with the minimum thickness of 50 m.
- Construction should be economical as possible.

Table 5-1. Data list for the task of sharing KURT site characterization data

		Data	Detail	Format	
	Background information about KURT			MS Word	
Geology	General geology	Geological description		MS Word	
		Lineaments (local)	Orientation, Length	Excel	A1
		Topography	Digital elevation map	Cad	A2
	Deep borehole data DB-1 : 500m (length) DB-2 : 1,000m (length) YS-1 : 500m (Core, fracture) only YS-6 : 500m	Core data	Core mapping	Cad/PDF	A3
		Logging data	Image by Acoustic televiewer	PDF and Excel	A4
			Image by BIPS	PDF	A4
		Geophysical logging data	Natural gamma	Excel	A5
			Full-wave sonic	Excel	A5
			SP	Excel	A5
			Electronic conductivity	Excel	A5
			Temp	Excel	A6
	Fractures	Deterministic fracture zones	Orientation, Width, Length	Excel	A7
		Background faults/large fractures	Frequency	Excel	A8
		Fracture set	Fracture set	Excel	A9
Hydrogeology	Hydrogeological properties	Permeability	K	Excel	A10
			T	Excel	A10
		Storage	S	Excel	A10
		Effective porosity	n	Excel	A10
Geochemistry	Geochemical properties. DB-1 : 500m YS-1 : 500m	Major ion	Cation, Anion	Excel	A11
		Minor ion	trace element	Excel	A11
		In-situ data	pH, DO, EC, Temp	Excel	A11
		Rock/Fracture minerals	Chemistry, mineralogy	Excel	A12

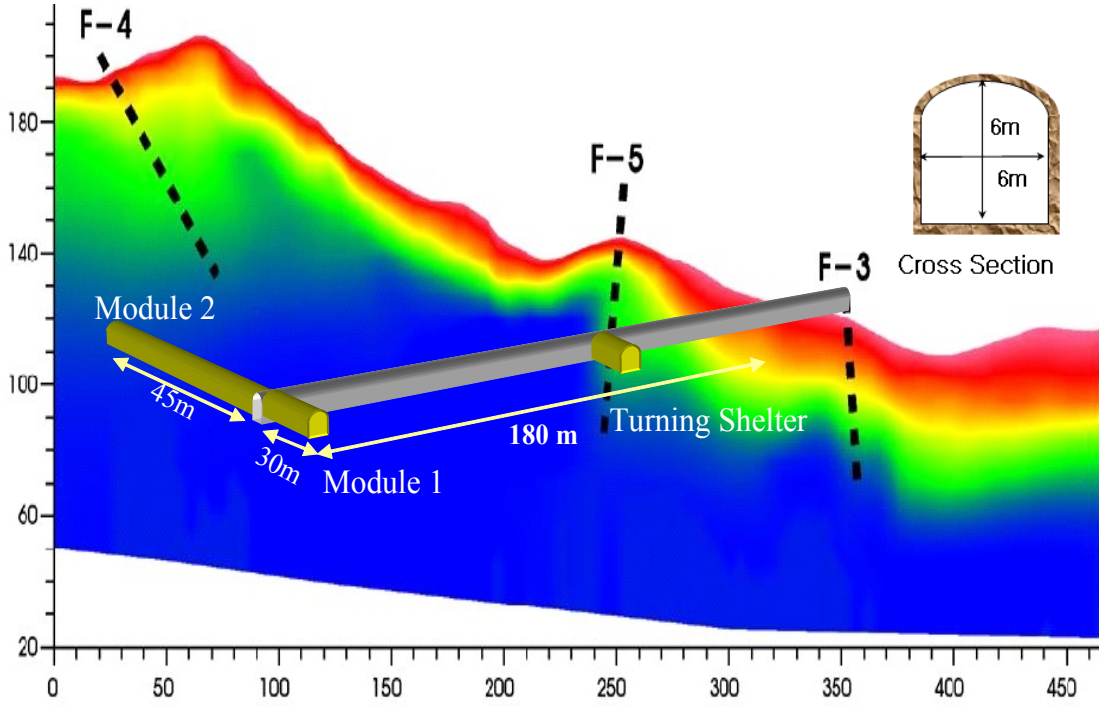

Figure 5-1. Current layout of the KURT

The drill and blasting method was applied to make a horseshoe shaped access tunnel and research modules. A careful blasting to minimize the blasting impact on the research reactor and other neighboring buildings at KAERI was required. Daily excavation was advanced about 1–3 m depending on the rock quality. The tunnel was supported mainly by using rock bolts and shotcrete in some zones of the tunnel. Lattice girders were installed at weak zones around the tunnel entrance and the fracture zones (Cho et al., 2008).

Data collected from geological investigations provided important information for the design and safety assessment of a repository system. Geological investigations at the KURT site were progressing, including developing site descriptive models and collecting geological, hydrological, and geochemical baseline datasets.

KURT has also played a significant role in developing and demonstrating a repository disposal system as well as the technologies needed for its construction and closure. The research experience gained at KURT has provided important information to validate the safety and feasibility of a disposal system and has made important contributions toward the successful implementation of a future commercial geological repository program.

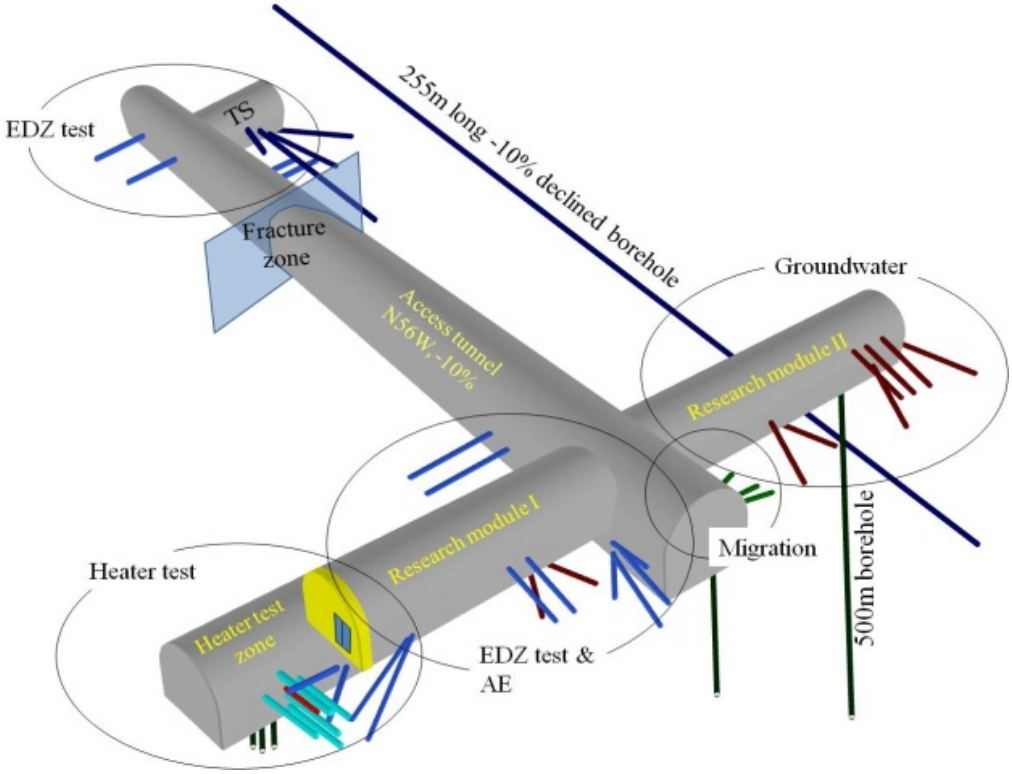

Figure 5-2. Location of in situ tests and experiments with related boreholes at KURT

Test and experiments in KURT:

During phase I (2006~2011), the following in situ tests and experiments were carried out after the successful completion of construction in Nov. 2006. Figure 5-2 shows the location of in situ tests and experiments and the associated boreholes.

- Single hole heater test: A 5 kw heater was installed in a heater hole, and about 100 temperature sensors were installed inside the rock surrounding the heater. The heater temperature was controlled to be increased step by step to 90°C. The power input, heater, air and rock temperatures, rock displacement, and rock stress were measured to investigate thermo-mechanical responses of the rock mass during the heating phase.
- EDZ characterization: Rock mass properties were measured to determine the characteristics of EDZ. Rock cores collected before and after excavation were investigated to evaluate thermal and mechanical property changes. Different geophysical tests were also applied to determine the size of EDZ.
- Solute migration experiments: Solute retardation by filling minerals in rock fractures was investigated to improve understanding of transport and retention of solute/colloid in a fractured rock mass.
- Development of site investigation techniques: Deep geological survey techniques, as well as QA procedures for various borehole tests, were developed to improve data quality.
- Long-term corrosion experiment: Estimation of long-term corrosion rate of disposal canister materials and the effect of dissolved oxygen (DO), Eh, and pH on the corrosion behavior.

- Hydrogeological and geochemical studies: Comprehensive data of hydrogeological and geochemical conditions were collected in regular term. Long-term monitoring of hydrogeological and geochemical parameters and the site descriptive hydro-structural modeling have been carried out.
- International collaboration project with SNL: KAERI investigated the influence of groundwater pressure on fracture aperture size, which controls the fracture transmissivity. Another research, i.e., a streaming potential (SP) experiment, is in progress to determine the hydraulic properties and behavior of the 3D subsurface volume of saturated fractured rock using a hydraulic head and streaming potential data.

Future plan:

During phase II (2012–2016), intensive experiments on hydrogeological characterization of MWCF and in situ long-term performance tests on a 1/3 scale engineered barrier system are major experimental research items to be executed at the KURT facility. The current dimensions of the research modules are limited, and thus the KURT facility needs to be extended for the execution of the planned tests and experiments during phase II. The design of the tunnel layout and construction method was optimized by March 2013. Fig. 4-9 shows an example of the potential tunnel layouts, which could be modified depending on the results from site investigations. The tunnel and additional utilities will be constructed from 2013 to 2014.

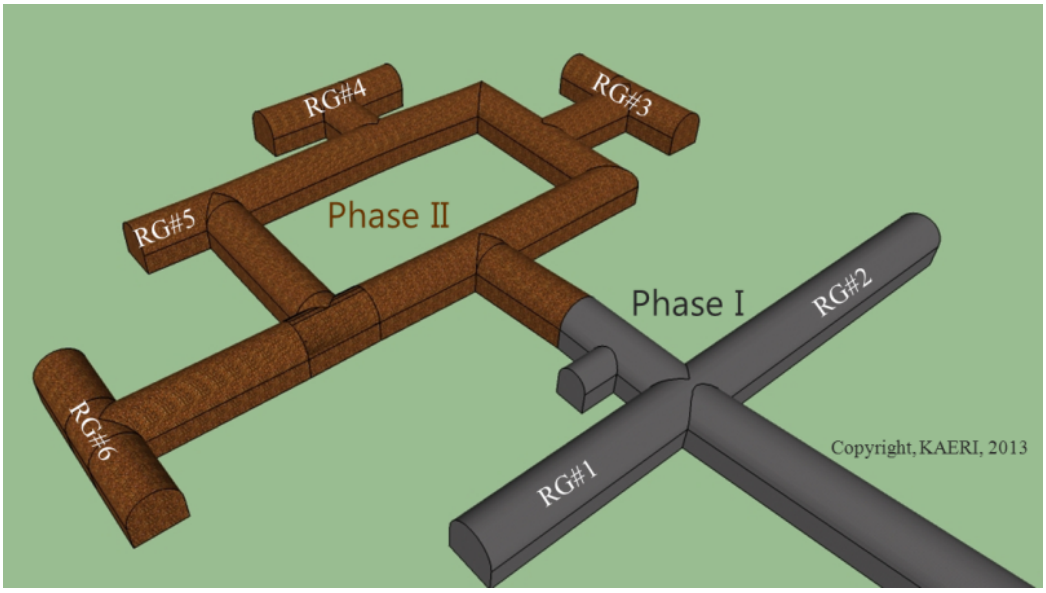

Figure 5-3. An alternative layout for tunnel extension of KURT

5.3 Geology of the KURT Site

The KURT is located in KAERI, which is stationed in the Yuseong area, which occupies the northem part of the city of Daejeon, Korea. The Yuseong area is approximately 150 km south from Seoul and belongs to the Keum River drainage basin in the western part of the Korean peninsula. The topography of the area

is characterized as having fairly rolling hills surrounded by upland with elevations of 300- 500 m. The highest point in the distant area was about 850 m, and most of the lowlands were located at an elevation of approximately 50 m. The geology of the Yuseong area is composed of Precambrian metamorphic and Mesozoic plutonic rocks and dikes (Figure 5-4). The Precambrian metamorphic rocks were distributed in the northwestern part of the study area and composed mainly of biotite gneisses and schists. They were intruded widely by plutonic rocks. The gneisses and schists were gradationally related. The Mesozoic plutonic rocks were composed of schistose granite, biotite granite, two-mica granite, and dike rocks. The two-mica granite is distributed most widely in the Yuseong area (Ryu, 2012).

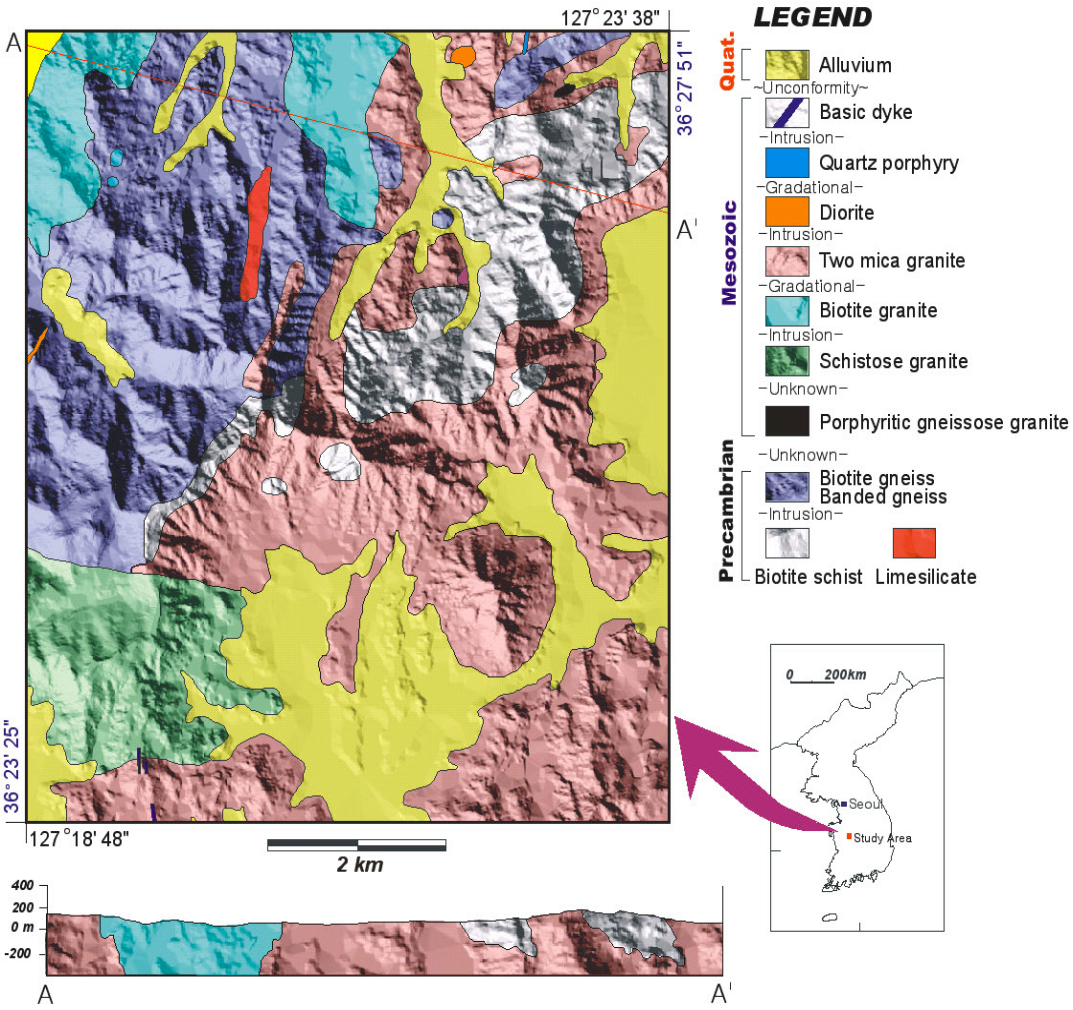

Figure 5-4. Location and geologic map of KURT site.

Two-mica granite with discernible foliation is a major rock type in cored rock samples at the KURT site. Under the microscopic observation of dri11 cores, the two mica granite consisted mainly of quartz, plagioclase, orthoclase, biotite, and muscovite, along with small amounts of chlorite, rutile, zircon, and apatite as accessory minerals. The two-mica granite often showed as biotitic granite and schistose biotitic granite in some biotite-concentrated areas. Sericitization was commonly observed along the twin or grain boundaries of the plagioclase, and chloritization was seen along the cleavages in the biotite. Some iron oxides existed as a glassy vein along the micro-fractures. The results of the modal analysis from fresh host rocks collected from the deep boreholes (YS-1 and DB-1) illustrate the existence of a classified table

of plutonic rock, which was mostly distributed in the granite region. The plagioclase of the fresh two-mica granite had an albite to oligoclase composition, and the biotite had an Al-depleted composition.

Whole-rock analyses of the major and trace elements suggested that the two mica granite was I-type and peraluminous granite and was formed by a differentiation of the calc-alkaline series. The SiO_2 content varied from 66.4 to 75.0%. The content of TiO_2, $A1_2O_3$, MgO, FeO_T , CaO, and P_2O_5 tended to have negative correlations with SiO_2, whereas K_2O had a positive correlation with SiO_2, which are the usual tendencies of granite (Kim et. al., 2004)

The mineralogy of fracture filling mineral were investigated from the borehole core samples. Most of the fractures were characterized by the existence of mineral coatings on the fracture surfaces. The fracture filling minerals are intergrown with each other. Illite, laumontite, calcite, chlorite, epidote, and montmorillonite were identified as fracture filling minerals. Laumontite (zeolite mineral) was very widely produced among the fracture-filling minerals. While a large amount of illite was not generated, it had the highest frequency of occurrence. The frequency of calcite was lower than that of the other fracture-filling minerals. Chlorite was mainly produced as an altered mineral on the fracture surfaces. The production of laumontite, epidote, and pyrite, in particular, suggest that the KURT site was influenced by hydrothermal alteration. According to observations using a scanning electron microscope (SEM), laumontite of a typical columnar crystal type and the illite and kaolinite of plate-type crystals were identified. In addition, chlorite and montmorillonite were produced as in a typical plate-type crystalline aggregation and typical honeycomb-type structure, respectively. Other fracture filling minerals identified in the cores include kaolinite, clinozoisite, pyrite, and iron oxides.

5.4 Deep Boreholes in the KURT Site

During an earlier stage, BH and YS series boreholes were drilled for a field-scale investigation. The depth of these boreholes ranged from 100 to 500 m. Among them, YS-1 and YS-6 boreholes were drilled at a depth of 500 m. KP-1 and KP-2 boreholes were investigated for the design of the KURT facility in particular prior to construction. During the KURT operation phase, DB-1 borehole was drilled at a depth of 500 m inside the tunnel to investigate deep geological environment. Recently, DB-2 borehole was drilled to a depth of 1,000 m outside of the tunnel to evaluate a main water conducting feature, which was identified during the DB-1 borehole investigation (Figure 5-5).

The lithological, mineralogical, rock mechanical, hydrogeological, and hydrogeochemical characteristics were investigated in these boreholes. A long-term monitoring of the groundwater pressure and chemical variations using a multi-packer system in DB-1 (SolExperts system, Switzerland) and YS-1 (Westbay system, Canada) boreholes was carried out. However, hydrochemical monitoring of YS-1 borehole has been stopped since 2006 due to the problem of MP system and grouting effect. The hydrochemical differences of YS-1 borehole were mainly resulted from the grouting activity, which carried out before MP installation on the fracture zone around GL-115m with Portland cement, where the borehole was collapsed after the drilling and hydraulic testing.

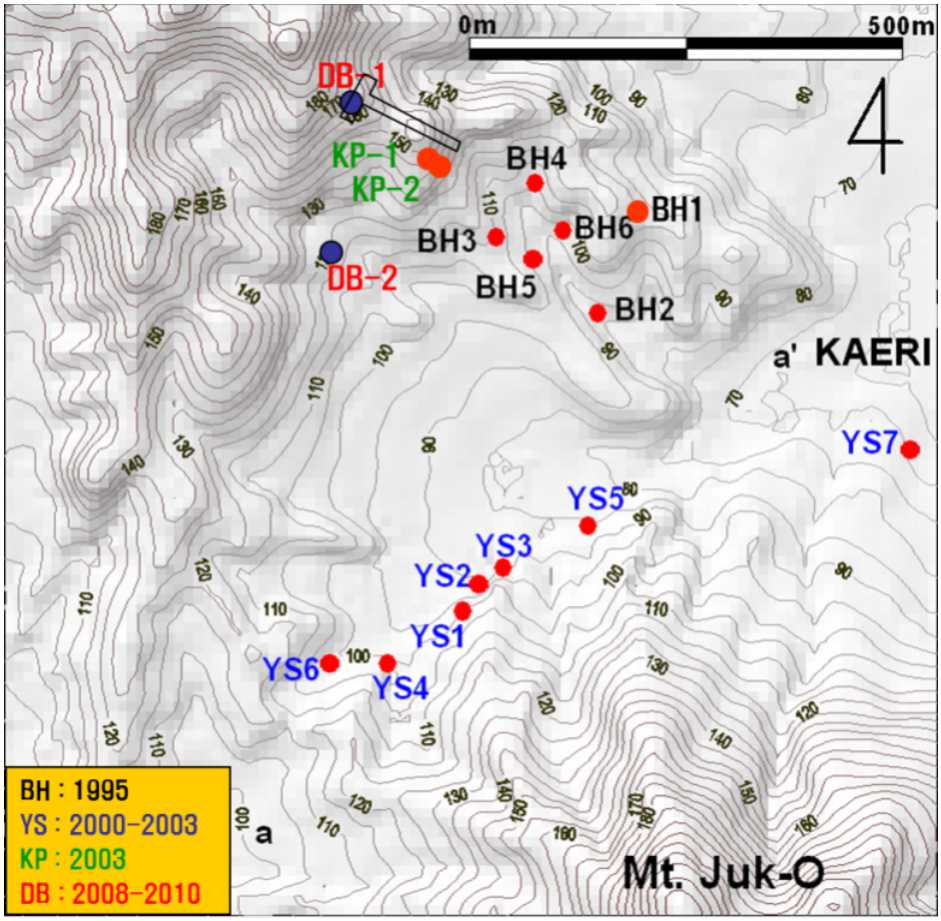

Figure 5-5. Location of boreholes around KURT.

During the operation of the KURT, additional geophysical surveys inside and outside of the tunnel, hydrogeological investigations (hydraulic testing and groundwater sampling), geophysical loggings, and VSP explorations in DB-1 and DB-2 boreholes were performed for developing geological model of the KURT site. These results were used to evaluate a conceptual hydrogeological model and a groundwater flow simulation.

5.5 Concluding Remarks

Sandia National Laboratories (SNL) and Korean Atomic Energy Research Institute (KAERI) have developed a multi-year plan for joint field testing and modeling to support the study of high-level nuclear waste disposal in crystalline geologic media, by leveraging the existing KAERI Underground Research Tunnel (KURT) (Wang, 2012). The work currently planned includes three tasks:

1. Streaming potential (SP) testing: This testing will use the existing experimental setup in the KURT to obtain a mechanistic understanding of the coupling of electrochemical processes with hydrologic flows in a fractured rock and develop a modeling capability for fusing SP signal with hydrologic measurements. This testing will directly support the Used Fuel Disposition (UFD) effort on developing advanced methods for characterizing an excavation-disturbed zone (EDZ).

KAERI will be responsible for instrumentation, field testing and data acquisition. SNL and KAERI will work jointly on experimental design and data interpretation. The work will be reported as a part of UFD milestone reports on flow characterization and modeling and international collaborations.

2. Sharing KURT site characterization data: The UFD Campaign is developing a discrete fracture network (DFN) model for modeling water flow and transport in fractured geologic media. Over the years, KAERI has performed extensive site characterization in KURT and its adjacent area. The data obtained from this effort will be valuable for DFN model validation and demonstration. In this task, KAERI will provide SNL with detailed fracture maps and hydrologic data around the KURT.
3. Technique development for in-situ borehole characterization: SNL and KAERI will develop a roadmap for the technique development and demonstration for in-situ borehole measurements. A key technique will be identified and the preliminary demonstration will be initiated using the DB-2 borehole.

For task 1, KAERI has acquired the needed equipment and started experimental setup for laboratory testing. This testing system will be transferred to the underground research laboratory once the new excavation in the KURT is completed. For task 2, KAERI has provided the following set of geological, hydrological, and geochemical data:

- A1: Lineament around KURT
- A2: Lineament index and DEM file
- A3: Core logging data of deep boreholes in KURT site
- A4: BHTV data of deep boreholes in KURT site
- A5: BIPS data of deep boreholes in KURT site
- A6: Geophysical logging data of deep boreholes in KURT site
- A7: Fracture zone data of deep boreholes in KURT site
- A8: Fracture frequency data of deep boreholes in KURT site
- A9: Summary of fracture set in KURT site
- A10: Hydrological properties of KURT site
- A11: Hydrochemical properties of water samples from the YS-1 and DB-1 boreholes.
- A12: Geochemical porperties of rock and minerals in KURT

These data will be used for the UFD discrete fracture network model development. Because of a large quantity of data involved, these data are available upon request (ywang@sandia.gov).

5.6 References

Cho, W. J., S. K. Kwon, and J. H. Park (2008), KURT, a small-scale underground research laboratory for the research on a high-level waste disposal, *Annals of Nuclear Energy*, 35, pp.132-140.

Ryu, J.-H., Y. K. Koh, S. W. Park, G. Y. Kim, and J.-W. Choi (2012), Geochemical Characterization of Deep Groundwater in KURT Using Geochemical Modeling, *J. Env. Eng.*, March, 2012, 351-359.

Wang Y. (2012), *Work Plan for UFD R&D Tests at KAERI Underground Research Tunnel (KURT) Site*, DOE-NE UFD FCRD-UFD-2012-000212.

This page left blank intentionally.

6 UPSCALING OF HYDROLOGIC AND GEOCHEMICAL PARAMETERS: LITERATURE REVIEW

6.1 Introduction

Parameters used in the assessment of groundwater flow and radionuclide transport in saturated media are determined from a wide range of laboratory and field-scale testing. Importantly, key hydrologic and geochemical parameters in geologic media generally vary spatially on multiple scales. Existing repository performance assessments try to capture this variability with model input parameter uncertainty, which inevitably lead to a significant overestimate of total flow flux and radionuclide release. Therefore, there is a need for the development of modeling capabilities to capture the effects of the spatial heterogeneity on fluid flow and radionuclide transport and to upscale hydrologic and geochemical properties from laboratory measurements to field observations. Such capabilities will significantly reduce both the predicted total radionuclide release from a repository and the associated uncertainty through improved performance prediction of the natural barrier system.

This section focuses on a literature review of upscaling of geologic permeability/hydraulic conductivity as well as upscaling of sorption coefficients/K_d. Assuming that heterogeneous spatial distributions of these parameters are known, several different techniques are offered for how to populate each model-cells/grid-block with a value for the parameter that effectively replicates the effects of its heterogeneous distribution. Such upscaling techniques will provide an important linkage between detailed process models and simplified total system performance models.

6.2 Upscaling Permeability/Hydraulic Conductivity

Two reviews on hydraulic conductivity upscaling were particularly useful in highlighting the strengths and weaknesses of each technique [*McKenna and Rautman*, 1996; *Renard and de Marsily*, 1997]. Promising techniques for upscaling can be broken into five categories, each of which is described below:

1. Spatial averaging (*Desbarats*, 1992);
2. Renormalization (*King*, 1989);
3. Perturbation theory (*Duquerroix et al.*, 1994);
4. Numerical inverse (*McKenna and Rautman*, 1996), and;
5. Power-law averaging (*Journel et al.*, 1986).

Of course, other more specialized techniques exist, but are less broadly applicable (*Harris et al.*, 2007).

6.2.1 Spatial Averaging

A number of expressions for averaging a property that exhibits spatial correlation (described by a second-order, stationary, random variable) have been developed (*Desbarats and Dimitrakopoulos*, 1990; *Desbarats*, 1992; *Dimitrakopoulos and Desbarats*, 1993). These techniques are based on geostatistical averaging methods and are referred to as "spatial averages." An algorithm for spatial averaging in two-dimensional domains (*Desbarats and Dimitrakopoulos*, 1990) uses the geometric mean of the point-scale data and the variogram describing those data. The upscaled value for effective hydraulic conductivity of a flow-model grid block is given as:

$$K_{eff} = K_G \exp\left[\frac{\sigma^2 - \gamma(V,V)}{2}\right], \tag{4-7}$$

where K_G is the geometric mean (see below) and the variance term, σ^2, refers to the variance of all point-scale values that lie within the larger scale block. The expression, $[\sigma^2 - \gamma(V,V)]$, is the average covariance value of the natural-log hydraulic conductivity values within the large-scale block. The term $\gamma(V,V)$ is the average value of the point-scale variogram within the larger, upscaled block. Another permutation of spatial averaging, developed for three-dimensional domains, is an extension of power-law averaging (*Dimitrakopoulos and Desbarats*, 1993). The significant feature of this extension relative to the power-law averaging (see below) is recognition of the dependence of K_{eff} on the scale of the grid block over which it is calculated, In the work of Dimitrakopoulos and Desbarats (1993), K_{eff} for a grid block in a numerical flow model is approximated by:

$$K_{eff} = K_w \exp\left\{\frac{1-w}{2}\left[\sigma^2 - \gamma\left(V,V\right)\right]\right\}, \tag{4-8}$$

where K_w is the power average of the entire suite of the core-scale (laboratory) hydraulic conductivity measurements, σ^2 is the variance of the natural-log transform of the core-scale measurements, w is the power (as in power-law averaging), and $\gamma(V,V)$ is the average variogram value of the lognormal, core-scale hydraulic conductivity values within the grid-block.

6.2.2 Renormalization

Renormalization is a technique for determining effective hydraulic conductivity that has seen limited use relative to other upscaling techniques. In its general sense, renormalization involves the derivation of mapping functions, which can translate the physical properties of a medium observed at one scale to a larger scale. The mapping takes place from one discrete scale to another discrete scale. King (1989) used an analogy between hydraulic conductivity and electrical conductance as a mapping function for hydraulic conductivity across scales. Another mapping function developed by Piggott and Elsworth (1992) is the geometric mean calculated through a mapping function that describes the probability of locations containing non-conductive sites. The complexity of mapping functions in both cases limits application of the scaling algorithm to blocks composed of 2×2 squares of smaller blocks in two dimensions and of 2×2×2 cubes of smaller blocks in three dimensions. Both of these studies (*King*, 1989; *Piggott and Elsworth*, 1992) consider only the case for which the range of spatial correlation is no larger than the grid-block dimensions (random structure); they also assume an isotropic field of small-scale conductivity values.

6.2.3 Perturbation Theory

Perturbation theory has also been used to examine the concept of effective hydraulic conductivity. Evaluation of heterogeneity by perturbation theory is based on the assumption that the hydraulic-conductivity field can be described by a mean value and "small" fluctuations about that mean; these small fluctuations have a mean of zero. The principal difficulty in applying perturbation theory to defining effective hydraulic-conductivity values has been the definition of the small fluctuations in the hydraulic conductivity field. In the original work, estimates of effective hydraulic conductivity were found to be accurate when the standard deviation of the natural-log hydraulic conductivity values was less than or equal to 0.5 (*Gutjahr et al.*, 1978):

$$\begin{aligned} K_{eff} &= K_G\left(1-\frac{\sigma_y^2}{2}\right) \quad \text{for 1D flow,} \\ K_{eff} &= K_G \quad \text{for 2D flow,} \\ K_{eff} &= K_G\left(1-\frac{\sigma_y^2}{6}\right) \quad \text{for 3D flow.} \end{aligned} \tag{4-9}$$

These results can be compared to earlier work involving the geometric average of hydraulic conductivity. Gutjahr et al. (1978) indicated that the effective hydraulic conductivity for steady flows was equal to the geometric mean in two dimensions, slightly below the mean in one dimension and slightly above it in three dimensions. Further work has extended the validity of Eq. (4-9) to the case of gradually varying flow; that is, to cases where the scale of head fluctuations is large relative to the scale of hydraulic-conductivity fluctuations (*Kitanidis*, 1990).

The development of Eq. (4-9) relies upon several assumptions that may be restrictive depending on the problem. These assumptions are: (1) a natural-lognormally distributed hydraulic-conductivity field, (2) a locally isotropic hydraulic-conductivity tensor, (3) "small" fluctuations about the mean hydraulic conductivity, (4) an infinite domain, and (5) stationarity of the hydraulic-conductivity field.

6.2.4 Numerical Inverse

Numerical techniques (also referred to as inverse techniques) typically involve the numerical solution of Darcy's law over a domain composed of separate, internally homogeneous, hydraulic-conductivity elements (*McKenna and Rautman*, 1996). By applying constant-head boundary conditions to opposite ends of the domain and no-flow boundary conditions to the sides of the domain, a uniform flow field is created. Effective hydraulic conductivity for the entire domain is determined by dividing the volumetric discharge by the cross-sectional area of the domain perpendicular to the flow direction and multiplying by the inverse of the gradient. There are several issues pertinent to the use of numerical techniques for determining effective hydraulic conductivity.

The boundary conditions of the flow domain are set arbitrarily to force a uniform gradient across the domain. This geometry yields the effective hydraulic conductivity only in the direction of flow. To calculate effective hydraulic conductivity in another direction, the gradient must be rotated. It is possible to define the principal directions of the hydraulic conductivity tensor through these gradient rotations; however, these calculations can become computationally expensive.

Another drawback involving the design of the flow system is the imposition of no-flow boundary conditions along the sides of the domain. These boundaries are an artifice necessary for computationally efficient calculation of K_{eff}. However, these no-flow boundaries may impose an unrealistic condition on the flow system. One technique for avoiding this problem is to embed the domain over which effective hydraulic conductivity is being determined within a "skin" of flow elements (*Gómez-Hernández and Journel*, 1990). Obviously, there is a trade-off between accuracy in modeling flow and the computational cost of using large skin volumes.

6.2.5 Power-Law Averaging

Power-law averages have been used extensively in the oil industry to estimate the effective hydraulic conductivity of simulator grid blocks from core-scale measurements (*Deutsch*, 1989b; *Journel et al.*, 1986). Dimitrakopoulos and Desbarats (1993) incorporated a power-law average into a spatial averaging equation:

$$K_w = \left(\frac{1}{N} \sum_{i=1}^{N} K_i^w \right)^{\frac{1}{w}}, \tag{4-10}$$

where K_w is the power-law average for a specific power, w, and the K_i are the N individual values of conductivity to be averaged. The bounding values of the maximum and minimum hydraulic conductivity computed using Eq. (4-10) are obtained for $w = 1$ and $w = -1$, respectively; these correspond to the arithmetic and harmonic means. The arithmetic mean is calculated as (*Freeze and Cherry*, 1979):

$$K_A = \sum_{i=1}^{N} \frac{K_i d_i}{d}, \tag{4-11}$$

where d is the total length of the flow path and the d_i are the lengths of each individual flow segment with hydraulic-conductivities, K_i. The harmonic mean is calculated as (*Freeze and Cherry*, 1979):

$$K_H = \frac{d}{\sum_{i=1}^{N} \frac{d_i}{K_i}}. \tag{4-12}$$

The geometric mean (*Gutjahr et al.*, 1978) is a result of $w = 0$, although Eq. (4-10) must undergo limited expansion (*Deutsch*, 1989a), because the expression as written is indeterminate at $w = 0$. The geometric mean is calculated as

$$K_G = \exp\left[\frac{1}{N} \sum_{i=1}^{N} \ln\left(K_i\right) \right]. \tag{4-13}$$

A technique to determine the correct value of w based on the spatial correlation structure of the hydraulic conductivity data has been demonstrated by several authors (*Deutsch*, 1989a; *Journel et al.*, 1986; *McKenna and Rautman*, 1996). The basic procedure makes use of the dependency of w on the spatial correlation structure. Several realizations of conductivity values with the size of the desired flow-model grid blocks are generated that exhibit the desired spatial structure, and the effective conductivities of these fields are computed through use of a numerical flow model. These values are viewed as the true effective hydraulic conductivities of the grid-scale model volumes. A curve-fitting technique then fits the K_w function of Eq. (4-10) to those true values, and the value of w associated with the best-fit curve is taken as the appropriate power for general application. The majority of studies involving power-law averaging have involved bimodal hydraulic conductivity distributions, such as occur in many elastic, sand-shale depositional sequences. In petroleum applications, the power, w, is typically defined as a function of shale content of the reservoir.

6.2.6 Evaluation

McKenna and Rautman (1996) performed a thorough and rigorous study of hydraulic conductivity upscaling as applied to a spatially correlated heterogeneous hydraulic conductivity field. The field was generated with SGSIM (*Deutsch and Journel*, 1998) and comprised 256×256 point values of hydraulic conductivity. These values are log-normally distributed with mean −4 and two levels of $\log_{10}$ hydraulic-conductivity variability of $\sigma = 0.5$ and 1.0. Finally, seven different fields were generated for each hydraulic-conductivity variability value (0.5 and 1.0) with spatial correlation lengths of 1, 2, 4, 8, 16, 32, and 64 units. Upscaling was performed using the techniques described above.

The spatial-averaging upscaling algorithm performed poorly in reproducing the transport properties of the non-upscaled simulation. This poor performance increased with increasing hydraulic conductivity variability (the results for $\sigma = 1$ yielded completely unreasonably upscaled values in the numerical experiments). The often significant computational burden of spatial-averaging is also a consideration.

The renormalization technique for upscaling proposed by King (1989) tended to create fields with a higher variance compared to other techniques. This higher variance is caused by the combination of arithmetic and harmonic averaging that takes place within the renormalization. These two types of averaging accentuate the high and low point values within the averaging space. In addition, the renormalization calculation is limited to averaging 2×2-arrays of point values at a time. To upscale point values to larger blocks, several iterations of scaling 2×2 values are necessary to achieve the final level of scaling. This parsing of the total number of point values into 2×2 grids and scaling them separately causes the variance to be larger than the other methods where all points are averaged together at the same time. Also, renormalization requires square elements, which are often impractical.

The perturbation technique produced upscaled results that overestimate the flow parameters, but produced transport parameters similar to the transport results of the other techniques. These results indicate that the perturbation method overestimated the mean value of hydraulic conductivity compared to other techniques, but it calculated similar values for the variability of the upscaled hydraulic conductivity field. McKenna and Rautman (1996) did not find perturbation techniques to be optimum for upscaling $K_{eff.}$

Selection of an upscaling technique also depends upon the practical considerations of implementation. Specifically, the method used to produce the upscaled material-property values for the individual flow-model elements must be capable of handling irregular shapes (for unstructured grid modeling). This limitation effectively precludes practical implementation of the numerical-inverse method, which requires solving the Laplace equation in a highly irregular (and spatially varying) geometry.

Power-law averaging appears to be a fast, flexible, and accurate technique for upscaling. The disadvantage of power-law averaging is the requirement of conducting a number of numerical experiments using different values of w to determine the best exponent. Results of power-law averaging showed that either travel-time distributions or total flux can be reproduced accurately a different power (the most accurate power for reproducing the point-scale flux was not the most accurate power for reproducing the point-scale transport parameters). In this situation, a compromise between reproducing the point-scale mass flux and the point-scale transport values must be reached. Moreover, the power-law averaging algorithm (including $w = -1$, 0, and 1) is essentially the only scaling algorithm feasible for use in scaling irregular and possibly anisotropic flow-model grids. Although use of power-law averaging is best after performing numerical experimentation to determine the correct power value, w, in the absence of available data or sufficient information, it is best to use geometric upscaling and set $w = 0$.

6.3 Upscaling of Sorption/Distribution Coefficients (K_d)

Several attempts have been made to upscale sorption or distribution coefficients, K_d (*Dean and Reimus*, 2008; *SNL*, 2007). Bethke and Brady (2000) even go so far as to say that K_d upscaling in and of itself is not an effective approach at large-scale reactive transport modeling (it tends to ignore long tails in breakthrough curves) and instead suggest using surface complexation theory (*Davis and Kent*, 1990; *Dzombak and Morel*, 1990) to specify effective or upscaled K_d.

Because laboratory batch sorption measurements or short-duration desorption measurements tend to significantly underestimate radionuclide sorption parameters (because they do not interrogate the fraction

of radionuclide mass that desorbs very slowly), Dean and Reimus (2008) proposed a technique to provide more accurate effective K_d values. They fit a multi-site kinetic model to their laboratory data to avoid using a single desorption-rate constant, which tended to over-predict radionuclide desorption and, in turn, underpredict radionuclide retardation factors. A simple thought experiment illustrates the motivation for their efforts (*Dean and Reimus*, 2008):

> Consider a simple two-site system in which the first site has a K_d value of 3 ml/g and represents 80% of the available sites, and the second site has a K_d value of 1000 ml/g and represents 20% of the available sites. These values are consistent with lab results where frequently 20% or more of the sorbed radionuclide tends to desorb very slowly (i.e., high K_d value), but the slowly desorbing fraction would effectively not be noticed in a batch sorption experiment or short-duration desorption experiment. The apparent K_d value from such an experiment would be ~3 ml/g, or approximately the value corresponding to the weaker sorption site. Assuming that transport over a small distance unit results in an 80:20 split of radionuclide mass experiencing the 3- and 1000-ml/g K_d values, respectively, then transport over n distance units will result in only 0.8^n of the radionuclide mass experiencing a K_d value of 3 ml/g, with the remaining radionuclide mass experiencing much greater K_d values. For large values of n, all of the mass converges toward experiencing a weighted average of the K_d values, in this case $0.8(3) + 0.2(1000) = 202.4$ ml/g. That is, a K_d value of 3 ml/g will be effectively experienced over 80% of the transport distance, while a K_d value of 1000 ml/g will be experienced over 20% of the transport distance. Kinetic effects are ignored in this example because it is assumed that time scales are long relative to the inverse of reaction rate constants. This simple analysis illustrates how effective K_d values will be much larger over long time and distance scales if effective K_ds are implemented rather than those measured from results of batch sorption and short-duration desorption experiments.

SNL (2007) defined upscaled (effective) K_d as the value of K_d applied to a large grid cell that yields modeled radionuclide sorption behavior similar to the modeled sorption behavior resulting from a heterogeneous distribution of small-scale K_d values. Preliminarily, K_d data should be available that are representative of the reactive constituents and the site groundwater, and these data should be translated into probability distribution functions (PDFs). It is important to note that some effort must be expended up front to conclude that this technique for upscaling K_ds is appropriate for each site. That is, numerical experiments should demonstrate that the transport characteristics (e.g., breakthrough curves) through a homogeneous system (in this case 500×500 m^2) using an effective K_d closely approximate the transport characteristics through a heterogeneous system where the random correlated spatial distribution of K_d is defined according to the K_d PDFs. The procedure is as follows:

1. Develop spatially correlated random K_d fields at a scale commensurate with the experimental data used to develop the defining PDFs. If possible, take into account geology and mineralogy in these distributions (i.e., perhaps K_d varies as a function of mineralogy and this mineralogy has constituents of known mass fraction/abundance).
2. Perform appropriate advection-dispersion-reaction modeling across each realization of the K_d field (recall that the K_d field may be conditioned on available geologic/mineralogic data). It should also be noted that spatially variable permeability fields were also developed on the same scale as the K_d fields and applied to the numerical grid to create a heterogeneous flow field.
3. Calculate and effective K_d, K_{eff}, in this case by running the model twice on each K_d/permeability realization both with and without reaction (in one case $K_d = 0$) and using this calculation:

$$K_{eff} = \frac{\theta}{\rho}\left(\frac{t_R}{t_{NR}} - 1\right), \tag{4-14}$$

where θ and ρ are the homogeneous formation porosity and bulk density, respectively, and t_R and t_{NR} are the time for 50% breakthrough for the reactive and non-reactive simulation, respectively. There is now one K_{eff} for each realization of the K_d/permeability realization (i.e., a distribution of K_{eff}).

4. Verify that the ensemble average breakthrough curve for all random K_d/permeability realizations is sufficiently close to the ensemble average breakthrough curve for all random permeability realizations using the K_{eff} calculated from each K_d realization.
5. Further verify that the K_{eff} distribution is independent of the correlation length used to develop the spatially correlated random K_d fields (assuming there are no data on K_d correlation lengths). Verify also that the K_{eff} distribution is independent of the hydraulic gradient boundary conditions supplied to the advection-dispersion-reaction model (and hence independent of the permeability fields).
6. Consult with subject matter experts to incorporate their opinions on the K_{eff} distribution. In this case, subject matter experts requested that the K_{eff} distribution be extended to the minimum and maximum values found in the spatially correlated random K_d fields with 5% probability assigned to the lower portion of the range and 30% probability assigned to the high side. The remaining 65% probability follows the unmodified K_{eff} distribution. This was felt to more completely capture the full range of K_d uncertainty.

To summarize, spatially heterogeneous K_d fields were calculated using geostatistics conditioning on K_d PDFs (incorporating any additional factors affecting the spatial distribution such as rock mineralogy and spatial heterogeneity if data are available). A single K_{eff} was calculated from each spatially heterogeneous K_d field and assembled into a distribution. Numerical experiments verified that the ensemble average breakthrough curve of all K_d realizations approximated the ensemble average curve when K_{eff} was used. Also, the K_{eff} distribution was found to be insensitive to both K_d correlation length and the applied hydraulic gradient boundary conditions. Not surprisingly, the K_{eff} distribution was much narrower than the K_d distributions used as input. This is to be expected because, in any upscaling study, as the scale gets larger, variability in the effective parameter gets smaller. Expert judgment may be used extend the range of K_{eff} if deemed necessary. The final distribution of K_{eff} will be used to develop the spatially variable K_d field for the upscaled model grid.

Some additional references are provided (*Auriault*, 1991; *Dagan*, 1979; *Duff et al.*, 2001; *Durlofsky*, 1992; *Gómez-Hernández and Journel*, 1994; *Indelman and Dagan*, 1993; *Neuman*, 1994; *Niibori et al.*, 2009; *Nœtinger*, 1994; *Poley*, 1988; *Rubin and Gómez-Hernández*, 1990; *Walker and Gylling*, 2002; *Wen and Gómez-Hernández*, 1996).

6.4 Scale Dependence of the Effective Matrix Diffusion Coefficient

While de Marsily (1986) thoroughly described scale-dependent dispersivity, more recently, researchers from Lawrence Berkeley National Laboratory noted scale dependence in effective matrix diffusion coefficients. Early work calculated a scale dependence of a fractal nature with the ratio of effective matrix diffusion, D_e, to matrix diffusion-coefficient, D_m, given as (*Liu et al.*, 2004a):

$$\frac{D_e}{D_m} = \delta^{1-d}\left(L^*\right)^{d-1}, \tag{4-15}$$

where δ is the length of the ruler used to measure the solute travel path (recall that this is a fractal analysis), L^* is the length scale (straight-line solute travel distance), and d is the site-specific fractal dimension. Because $d > 1$, D_e/D_m increases with L^*. Also, d is site specific; at Yucca Mountain it is 1.7 (*Callahan et al.*, 2000; *Liu et al.*, 2003; *Liu et al.*, 2004b) and at Mirror Lake it is 1.3 (*Becker and Shapiro*, 2000; *Shapiro*, 2001).

Liu et al. (2007) also derived analytical solutions for effective matrix diffusion scale dependence in heterogeneous media as well as in media characterized by multiple (fracture) flow paths. For heterogeneous porous media with log-normally distributed permeability described using σ_k as the standard deviation of ln(k), the effective permeability is defined in terms of the geometric-mean permeability, k_g, as:

$$k_e = k_g \exp\left(\frac{\sigma_k}{2}\right). \tag{4-16}$$

After some further assumptions and mathematical manipulation, Liu et al. (2007) define for heterogeneous media:

$$\frac{D_e}{D_m} = \left(\frac{k_e}{k_g}\right)^{\frac{(2+n)^2}{2m^2}}, \tag{4-17}$$

where m and n are exponents characterizing the porosity-permeability relationship and tortuosity for matrix diffusion, respectively. Assuming a typical value of $m = 3$ (*Costa*, 2006), and a value of $n = 1$ corresponding to the lower limit of n (*Boving and Grathwohl*, 2001; *Liu et al.*, 2004a), the exponent in the preceding equation is 0.5.

The derivation of scale-dependent effective matrix diffusion in a fractured medium begins with definition of parameter, a, which is assumed to follow a normal distribution:

$$a = \frac{\phi_m \sqrt{D_m}}{2b}. \tag{4-18}$$

The normal probability distribution function of a is described according to σ, the standard deviation of a and $\bar{a}$, the arithmetic mean of a. This derivation is only good for a low degree of heterogeneity (so that few negative values of a are included in the distribution such that:

$$\sigma' = \frac{\sigma}{\bar{a}} \le \frac{1}{3}. \tag{4-19}$$

After some mathematical manipulation based on the Tang et al. (1981) solution for solute transport in a channel, the scale-dependent effective matrix diffusion is given as:

$$\frac{D_e}{D_m} = \left[\frac{1}{1 - 2\tau\bar{a}^2\left(\sigma'\right)^2}\right]^2, \tag{4-20}$$

where the residence time is $\tau = x/V$ (x is distance traveled and V is the fracture flow speed).

Liu et al. (2007) conclude their study with a literature survey examining field-scale effective matrix diffusion coefficients for fractured rock system. Forty field tracer tests at 15 fractured rock sites were surveyed for effective matrix diffusion coefficients. The scale factors for the matrix diffusion coefficient (to convert it to effective matrix diffusion coefficient) ranged from 0.5 to 884 for observation scales from 5 to 2,000 m. At a given scale, the scale factor varied by two orders of magnitude, reflecting differences in geology at each site. Four reasons for matrix diffusion scale dependence were provided: (1) presence of a degraded zone along fracture walls and infilling materials (gouge) within fractures, (2) variability in fracture aperture within a single fracture, (3) co-existence of differently scaled fractures (i.e., global-flow fractures, bypassed fractures, small fractures, and ultra-small fractures), and (4) multirate diffusion processes caused by heterogeneity in the matrix porosity and diffusion coefficient within the rock matrix.

6.5 Site Characterization to Performance Assessment Upscaling

In March of 2005, the Äspö task force on modeling of groundwater flow and solute transport released their summary of Tasks 6A, 6B, and 6B2 (Hodgkinson and Black, 2005). This fascinating project disbursed a detailed data set from a dipole radiologic-tracer experiment in a natural granite fracture to 11 international modeling teams and asked each to build their own conceptual model of the system (Task 6A). Next, using the tracer-test data, each team was to constrain system parameters (i.e., perform parameter estimations on quantities such as velocity, dispersivity, mass-transfer rates, and sorption parameters) as Task 6B. Finally, in Task 6B2, each team was to modify the site-characterization parameters to appropriately reflect the performance-assessment scale. Neither models nor intrinsic parameters for the media could be altered (e.g., fracture aperture and matrix porosity), but the flow was now to be simulated as a natural gradient (four orders of magnitude slower) and only the solute transport parameters like mass-transfer rate, dispersion, and sorptivity could be changed. Not surprisingly, each modeling team found this exercise challenging and results varied widely. Several general conclusions were presented: (1) data that constrain site-characterization parameters do not do a good job at constraining performance-assessment-scale parameters (e.g., flow-wetted fracture surface area and transport aperture), (2) laboratory measured sorption coefficients, K_d, are not appropriate for use in interpreting field-scale tracer tests, and (3) assumptions of irreversible sorption that seem appropriate at the site-characterization scale are not likely to be appropriate at the performance-assessment scale. The overarching conclusion is that site-characterization data only inform short-term phenomena; the diffusive and sorptive properties of near-fracture immobile zones, which dominate the interpretation of short-term tracer tests, are not at all important at the performance-assessment scale. A key recommendation going forward is to explicitly include performance-assessment-scale information from natural analogue sites. While 11 different techniques were presented to upscale site-characterization models to performance-assessment models, none were particularly appealing or compelling. Clearly, this is a significant scientific challenge requiring much more research effort.

Acknowledgment: The work documented in this section is based on the work done by former Sandian Dr. Scott James a few years ago in support of the UFD program.

6.6 References

Auriault, J. L. (1991), Heterogeneous medium. Is an equivalent macroscopic description possible?, *International Journal of Engineering Science*, *29*(7), 785-795.

Becker, M. W., and A. M. Shapiro (2000), Tracer transport in fractured rock: Evidence of nondiffusive breakthrough tailing, *Water Resources Research*, *36*, 1677-1686.

Bethke, C. M., and P. V. Brady (2000), How the K_d approach undermines ground water cleanup, *Ground Water*, *38*(3), 435-443.

Boving, T. B., and P. Grathwohl (2001), Tracer diffusion coefficients in sedimentary rock: Correlations to porosity and hydraulic conductivity, *Journal of Contaminant Hydrology*, *53*, 5-100.

Callahan, T. J., et al. (2000), Using multiple experimental methods to determine fracture/matrix interactions and dispersion of nonreactive solutes in saturated volcanic rock, *Water Resources Research*, *36*(12), 3547-3558.

Cook, P.G., A. L. Herczeg (2000), *Environmental Tracers in Subsurface Hydrology*, Kluwer, Boston, 529p.

Cook, P. G., A. J. Love, N. I. Robinson, and C. T. Simmons (2005), Groundwater ages in fractured rock aquifers, *J. Hydrology*, 308(1-4), 284-301.

Cook, P. G., and N. I. Robinson (2002), Estimating groundwater recharge in fractured rock from environmental ^{3}H and ^{36}Cl; Clare Valley, South Australia, *Water Resources Research* 10.1029/2001WR000772.

Costa, A. (2006), Permeability-porosity relationship: A reexamination of the Kozeny-Carman equation based on a fractal pore-space geometry assumption, *Geophysical Research Letters*, *53*, 85-100.

Dagan, G. (1979), Models of groundwater flow in statistically homogeneous porous formations, *Water Resources Research*, *15*(1), 47-63.

Davis, J. A., and D. B. Kent (1990), Surface complexation modeling in aqueous geochemistry, in *Mineral-Water Interface Geochemostry*, edited by M. F. Hochella and A. F. White, pp. 177-260, Mineralogical Society of America, Washington, DC.

de Marsily, G. (1986), *Quantitative Hydrogeology: Groundwater Hydrology for Engineers*, 440 pp., Academic Press, Inc., San Diego, California.

Dean, C. A., and P. W. Reimus (2008), Effective K_d values for radionuclides in Yucca Mountain saturated alluvium, in *International High-Level Radioactive Waste Management Conference*, edited, pp. 171-178, Las Vegas, NV.

Desbarats, A. J., and R. Dimitrakopoulos (1990), Geostatistical modeling of transmissibility for 2D reservoir studies, in *SPE Formation Evaluation*, edited, pp. 437-443.

Desbarats, A. J. (1992), Spatial averaging of hydraulic conductivity in three-dimensional heterogeneous porous media, *Mathematical Geology*, *24*(3), 249-267.

Deutsch, C. V. (1989a), DECLUS: A Fortran 77 program for determining optimum spatial declustering weights, *Computers and Geosciences*, *15*(3), 325-332.

Deutsch, C. V. (1989b), Calculating effective absolute permeability in sandstone/shale sequences, in *SPE Formation Evaluation*, edited, pp. 343-348.

Deutsch, C. V., and A. G. Journel (1998), *GSLIB: Geostatistical Software Library and User's Guide*, 2 ed., Oxford University Press, New York, New York.

Dimitrakopoulos, R., and A. J. Desbarats (1993), Geostatistical modeling of grid block permeabilties for 3D reservoir simulators, in *SPE Reservoir Engineering*, edited, pp. 13-18.

Duff, M. C., et al. (2001), Comparison of two micro-analytical methods for detecting the spatial distribution of sorbed Pu on geologic materials, *Journal of Contaminant Hydrology*, *47*, 211-218.

Duquerroix, J.-P., et al. (1994), Influence of permeability anisotropy on large-scale properties of heterogeneous reservoirs, in *SPE Annual Technical Conference and Exhibition*, edited, p. 16, Society of Petroleum Engineers, Richardson, TX.

Durlofsky, L. J. (1992), Representation of grid block permeability in coarse scale models of randomly heterogeneous porous media, *Water Resources Research*, *28*(7), 1791-1800.

Dzombak, D. A., and F. M. M. Morel (1990), *Surface Complexation Modeling: Hydrous Ferric Oxide*, 416 pp., John Wiley & Sons, New York, NY.

Freeze, A. R., and J. A. Cherry (1979), *Groundwater*, 604 pp., Prentice-Hall, Inc., Englewood Cliffs, New Jersey.

Gómez-Hernández, J. J., and A. G. Journel (1990), Stochastic characterization of grid-block permeabilities: From point values to block tensors, in *2nd European Conference on the Mathematics of Oil Recovery*, edited by D. Guèrillot and O. Guillon, pp. 93-90, Edition Technip, Paris, France.

Gómez-Hernández, J. J., and A. G. Journel (1994), Stochastic characterization of gridblock permeabilities, in *SPE Formation Evaluation*, edited, Society of Petroleum Engineers.

Gutjahr, A. L., et al. (1978), Stochastic analysis of spatial variability in subsurface flows. 2. Evaluation and application, *Water Resources Research*, *14*(5), 953-959.

Harris, S. D., et al. (2007), Three-dimensional upscaling of fault damage zones for reservoir simulation, in *Structurally Complex Reservoirs*, edited by S. J. Jolley, et al., pp. 353-374., The Geologic Society of London, London, UK.

Indelman, P., and G. Dagan (1993), Upscaling of conductivity of heterogeneous formations: General approach and application to isotropic media, *Transport in Porous Media*, *12*, 161-183.

Journel, A. G., et al. (1986), Power averaging for block effective permeability, in *SPE California Regional Meeting*, edited, Society of Petroleum Engineers, Oakland, CA.

Kim, G. Y., Y. K. Koh, D. S. Bae, and C. S. Kim (2004), Mineralogical characteristics of fracture-filling minerals from the deep borehole in the Yuseong area for the radioactive waste disposal project, *J. Miner. Soc. Korea*, 17(1), 99-114.

King, P. R. (1989), The use of renormalization for calculating effective permeability, *Transport in Porous Media*, *4*(1), 37-58.

Kitanidis, P. K. (1990), Groundwater flow in heterogeneous formations, in *Second George Kovac's Colloquium*, edited, UNESCO, Paris, France.

Liu, H. H., et al. (2003), Modeling flow and transport in unsaturated fractured rocks: An evaluation of the continuum approach, *Journal of Contaminant Hydrology*, *62-63*, 173-178.

Liu, H. H., et al. (2004a), Scale dependency of the effective matrix diffusion coefficient, *Vadose Zone Journal*, *3*, 312-315.

Liu, H. H., et al. (2004b), Field investigation into unsaturated flow and transport in a fault: Matrix diffusion and the validity of models, *Journal of Contaminant Hydrology*, *74*(1-4), 39-59.

Liu, H. H., et al. (2007), Scale dependence of the effective matrix diffusion coefficient: Some analytical results, *Vadose Zone Journal*, *6*, 679-683.

McKenna, S. A., and C. A. Rautman (1996), Scaling of material properties for Yucca Mountain: Literature review and numerical experiments on saturated hydraulic conductivity, 117 pp, Sandia National Laboratories, Albuquerque, NM.

Neuman, S. P. (1994), Generalized scaling of permeabilities: Validation and effect of support scale, *Geophysical Research Letters*, *21*(5), 349-352.

Niibori, Y., et al. (2009), Evaluation of solute transport through a fracture by considering the spatial distributions of retardation effect in grain scale, *Journal of Hydraulic Engineering-ASCE*, *14*(11), 1214-1220.

Nœtinger, B. (1994), The effective permeability of a heterogeneous porous formation, *Transport in Porous Media*, *15*, 99-127.

Piggott, A. R., and D. Elsworth (1992), Analytical models for flow through obstructed domains, *Journal of Geophysical Research*, *97*(B2), 2085-2093.

Poley, A. D. (1988), Effective permeability and dispersion in locally heterogeneous aquifers, *Water Resources Research*, *24*(11), 1921-1926.

Renard, P., and G. de Marsily (1997), Calculating equivalent permeability: A review, *Advances in Water Resources*, *20*(5-6), 253-278.

Rubin, Y., and J. J. Gómez-Hernández (1990), A stochastic approach to the problem of upscaling of conductivity in disordered media: Theory and unconditional numerical simulations, *Water Resources Research*, *26*(4), 691-701.

Shapiro, A. M. (2001), Effective matrix diffusion in kilometer-scale transport in fractured crystalline rock, *Water Resources Research*, *55*, 175-211.

SNL (2007), Saturated Zone Site-Scale Transport, Sandia Natrional Laboratories, Las Vegas, Nevada.

Tang, D. H., et al. (1981), Contaminant transport in a fractured porous media: Analytical solution for a single fracture, *Water Resources Research*, *17*(3), 555-564.

Walker, D., and B. Gylling (2002), Site-scale groundwater flow and modelling of Aberg and upscaling of conductivity, 57 pp, Swedish Nuclear Fuel and Waste Management Company, Stockholm, Sweden.

Wen, S.-H., and J. J. Gómez-Hernández (1996), Upscaling hydraulic conductivites in heterogeneous media: An overview, *Journal of Hydrology*, *183*, ix-xxxii.

Zhou, Q., et al. (2007), Field-scale effective matrix diffusion coefficient for fractured rock: Results from literature survey, *Journal of Contaminant Hydrology*, *93*, 161-187.